

S -wave pion-pion scattering lengths from nucleon-meson fluctuations

Jürgen Eser^{1,*} and Jean-Paul Blaizot^{1,†}

¹*Université Paris-Saclay, CNRS, CEA, Institut de physique théorique, 91191, Gif-sur-Yvette, France*
(Dated: December 30, 2021)

We present calculations of the S -wave isospin-zero and isospin-two pion-pion scattering lengths within a nucleon-meson model with parity doubling. Both scattering lengths are computed in various approximations, ranging from a mean-field (MF) calculation towards the inclusion of loop corrections by means of the functional renormalization group (FRG). The bosonic part of the investigated nucleon-meson model is formulated in terms of stereographic projections as a “natural” set of coordinates on the respective vacuum manifold. We thereby elucidate subtleties concerning the truncation of the effective action w.r.t. higher-derivative pion interactions and the “successful” computation of the scattering lengths. As the main result, we find simultaneous agreement for the isospin-zero and isospin-two scattering lengths with experimental data within the LPA'-truncation of the FRG, together with chiral symmetry breaking (roughly) occurring at the characteristic scale of $4\pi f_\pi$. The isoscalar σ -mass is dynamically generated by the FRG integration of momentum modes, and is a prediction of the model. It ends being of the order of 500 MeV, i.e., much lower than the value (> 1 GeV) found in MF or one-loop treatment of this or related models. Finally, the convergence of the corresponding low-energy expansion of the quantum effective action in terms of pion momenta is discussed.

I. INTRODUCTION

With only the two lightest (and idealized as mass-degenerate) quark flavors (“up” and “down”), the chiral $SU(2) \times SU(2)$ -symmetry of quantum chromodynamics (QCD) is broken to an $SU(2)$ flavor subgroup. This breaking occurs explicitly through the nonvanishing quark masses and spontaneously through the formation of a quark condensate. As the ultimate consequence, the color-singlet hadrons (approximately) appear as multiplets of the flavor subgroup, named isospin. Historically, the concept of isospin was first established from the observation of almost mass-degenerate protons and neutrons [1–3], whose quark contents are combinations of the up and down flavors. The proton and the neutron form the nucleon doublet, which is the fundamental representation of the $SU(2)$ isospin group. They carry opposite projections of the isospin quantum number $I = 1/2$ (proton: $+1/2$; neutron: $-1/2$).

The pivotal principles of chiral and isospin symmetries governing the hadronic regime of the strong interaction give rise to effective models of QCD. These basically come in two distinct classes: linear and nonlinear models—referring to linear or nonlinear realizations of chiral symmetry. Their respective stereotypes are given by the linear sigma model (LSM) [4–6] and the nonlinear sigma model (NLSM) [5, 7–10]. The LSM incorporates all chiral partners (fields with the same quantum numbers except for parity), which appear in the hadronic multiplets, equally as dynamical degrees of freedom (d.o.f.). The NLSM reduces the field content to the (pseudo-)Nambu-Goldstone bosons of chiral symmetry breaking. It is the fundamental building block of chiral perturbation theory (ChPT) [11–16], which elevates itself as the effective field theory of low-energy QCD. In general, phenomenological Lagrangians obtained from these principles were seminally discussed in Refs. [9, 17–21].

The research objective of the present work is the computation of the S -wave isospin-zero and isospin-two pion-pion scattering lengths within an effective nucleon-meson model. To this end, we formulate the model in the framework of the quantum effective-action formalism, with special emphasis on the integration of quantum fluctuations using the FRG technique [22–25]. We are interested in the capability of this approach to reproduce experimental data on the scattering lengths, hence testing and exemplifying the infrared (IR) dynamics of the class of LSMs. Our results are predictions of a non-fundamental hadronic model (with a linear realization of chiral symmetry). Nevertheless, they represent loop-corrected low-energy observables computed with a nonperturbative method. We systematically and conclusively compare the scattering lengths to (common) MF and one-loop calculations as well as to similar effective models [26–29].

Another focus lies on the relation of the nucleon-meson model to the corresponding NLSM, which readily emerges when restricting the dynamics of the system to the three-sphere S^3 (that corresponds to the vacuum manifold) [30–33]—the regularization and perturbative renormalization of the NLSM with the help of the LSM (in this particular

* juergen.eser@ipht.fr

† jean-paul.blaizot@ipht.fr

limit) was indeed proposed in the past by Refs. [30, 34–36]. To account for these geometric aspects along with the derivation of the scattering lengths, we express the bosonic part of the quantum effective action through stereographic projections as a “natural” set of coordinates on S^3 . We elucidate subtleties regarding higher-derivative interactions and their influence on the analytic and numeric results. The usage of stereographic coordinates for this objective originates from Refs. [37–42], which treat the dynamic generation of (stereographic) higher-derivative couplings in the $SO(4)$ - and $SO(6)$ -symmetric quark-meson(-diquark) models; this has the practical virtue of adopting the mathematical formulas and geometric knowledge developed in these publications. In the formulation of stereographic coordinates, well-known low-energy relations from the NLSM are evident—yet other sets of coordinates are equally appropriate for the calculation of the coordinate-independent on-shell pion-pion scattering amplitude.

The FRG is a modern implementation of the Wilsonian renormalization group [43]. It has found diverse applications in high-energy and statistical physics (and other areas such as quantum gravity), see Ref. [44] for a recent review. The method is well-suited to analyze the long-distance low-energy properties of theories or models of various kinds, interpolating from the ultraviolet (UV) classical action towards the quantum effective action in the IR. For instance, it offers a straightforward description of QCD bound states via dynamical hadronization [45]. Furthermore, the mapping of LSMs onto nonlinear realizations of chiral symmetry (within the FRG) was pioneered by Refs. [37–42, 46–48], where linearly realized quark-meson(-diquark) models were transformed into their nonlinear low-energy limits. The fixed-point structure and the geometry of the NLSM were thoroughly worked out by Refs. [40, 49–53], also underlining its relevance for gravitational physics. The consistent embedding of effective hadronic models into the FRG formalism and related developments were addressed and summarized in Ref. [54]; LSMs are oftentimes employed for questions related to the QCD phase diagram [55].

Effective nucleon-meson models, introduced during the “pre-QCD era,” were originally motivated by the ambition to describe the strong nuclear force between protons and neutrons. Within such models, the nuclear force is carried by light mesons, which are exchanged among nucleons, a picture that still holds in the framework of QCD for small momenta. The nucleon-meson model to be considered here takes up this idea of effective dynamics. It further features the concept of parity doubling [56–59], i.e., it comprises the explicit treatment of the chiral partners of the nucleons, where we assume that this applies to the $N(1535)$ -resonance [3]. The parity doubling of nucleons, which is accompanied by the mirror assignment of Dirac spinors w.r.t. chiral symmetry, allows for a chiral-invariant “bulk mass” m_0 in the fermionic sector of the model. On the one hand, this m_0 -parameter reflects the “heterogeneous” nature of the nucleon mass, since only a minor fraction comes from chiral symmetry breaking [besides the trace anomaly as well as intrinsic quark and gluon field energies, see e.g. Refs. [60–63]]. On the other side, it leads to nonzero nucleon masses even in the chiral-restored phase, where chiral partners become degenerate in mass.

Despite the fact that the parity-doublet model incorporates the nucleons in the “nonstandard” mirror assignment—and this property does not (necessarily) stand for example in the tradition of the early Walecka and Lee-Wick models for nuclear matter [64, 65]—, it serves as an interesting starting point for the analysis of the pion-pion scattering amplitude (and represents the class of LSMs). The parity doubling promises (presumably) heavier fermion masses as compared to quark-meson or naively-assigned nucleon-meson models (in which the masses of quarks/nucleons do not “survive” chiral symmetry restoration). The suppression and massive decoupling of the fermionic fluctuations along decreasing energy-momentum scales is an important ingredient for the reproduction of hadronic low-energy observables [38, 42, 45]. This lets us (in the first instance) recede from analogous investigations in quark-meson models, whose low-energy couplings have proven to be dominated by the fermionic loop contributions even far in the IR [38], and from similarly constructed nucleon-meson models without chiral-invariant nucleon mass.

The thermodynamics of the parity-doublet nucleon-meson model was extensively studied within the FRG approach in Refs. [66, 67]. The corresponding phase diagram shows a robust chiral phase transition inside dense nuclear matter, in addition to the nuclear liquid-gas transition. The mass parameter m_0 was chosen as 800 MeV. This value principally matches the rather broad range of $200 \text{ MeV} \lesssim m_0 \lesssim 900 \text{ MeV}$ assumed in numerous phenomenological investigations, see e.g. Refs. [56, 59, 68, 69]. Most often, slightly more precise values of 500 MeV to 800 MeV are discussed. Although the value of the chiral-invariant mass m_0 is lively debated in the current literature and directly affects the equation of state of dense nuclear matter, it is of subordinate importance for our purposes—albeit the computation of the scattering lengths as IR observables of the parity-doublet model lets us comment on it. Indications for parity doubling and nonzero nucleon masses beyond the chiral phase transition were also found in recent lattice-QCD calculations [70]. Generally, FRG applications to nuclear matter under extreme conditions of density (apart from the discussion of parity doubling) were carried out in Ref. [71].

The theoretical reference of our investigations—concerning algebraic expressions and numeric precision—is ChPT, which provides a systematic and model-independent analysis of hadronic correlation functions. Effective Lagrangians formulated in the context of ChPT are based on a nonlinear realization of chiral symmetry, leading at lowest order to exclusive pion self-interactions. The pions are the (pseudo-)Nambu-Goldstone bosons of spontaneous chiral symmetry breaking [72–74]. They dominate the pole structure of the hadronic correlation functions, which precisely makes them the most relevant d.o.f. in the low-energy regime of the strong interaction. The couplings of the pion self-interactions

within effective Lagrangians are determined by the low-energy constants of QCD [11, 12, 75].

In the spectrum of physical particles, the neutral pion π^0 and the two charged pions π^\pm form an isospin triplet, i.e., $I = 1$. The chiral partner of the three pions is the isoscalar σ -meson, which is eliminated in the nonlinear realization in favor of pionic interactions (whereas its presence is eponymous in the LSM). The light pion mass of $M_\pi \simeq 138$ MeV [3] (averaged over M_{π^0} and M_{π^\pm}) substantiates the special role of the pions as low-energy mediators of the strong interaction.

The nonlinear effective field theory of pions is the result of the so-called chiral expansion, i.e., the simultaneous low-energy expansion of the generating functional of QCD in terms of pion momenta and quark masses. The generating functional contains mesonic currents as perturbations to the massless QCD Lagrangian. In the sense of the external field method, this supplementation yields direct access to (mesonic) correlation functions. Moreover, these functions obey symmetry relations, which are known as the chiral Ward identities and which are equivalent to the invariance property of the generating functional under (local) chiral transformations [11–14, 16].¹

The chiral expansion relies on the small ratio $|p^2|/M^2 < 1$, where p denotes the pion momentum and M indicates the mass scale such that (low-energy) propagators of the form $(p^2 - M^2)^{-1} \simeq -M^{-2}(1 + p^2/M^2 + \dots)$ converge [14]. The parameter M is identified with typical hadronic mass scales like the proton mass, the ρ -meson mass $M_\rho \simeq 775.26$ MeV [3], or the characteristic chiral-symmetry breaking scale $4\pi f_\pi$ [14, 76]. The latter follows from a “naive” dimensional analysis of loop diagrams contributing to the pion-pion scattering process. It involves the (weak) pion decay constant $f_\pi = (130.2 \pm 1.2)/\sqrt{2}$ [3],² which itself is a measure for the strength of chiral symmetry breaking. The chiral expansion and the dynamic generation of low-energy couplings from renormalization-group flow equations were explored by Refs. [37–39, 42, 46, 47]; some of these “preparatory” works also promote the usage of stereographic coordinates.

An immediate application of ChPT is the computation of the S -wave pion-pion scattering lengths [77–82]. Regarding the S -wave (with angular momentum $l = 0$) in the partial-wave decomposition, the leading-order scattering amplitude is completely determined by the two scattering lengths a_0^0 and a_0^2 (with isospin $I = 0, 2$; the subscript is given by the angular momentum l and the superscript denotes the isospin I). Both scattering lengths are experimentally measured and theoretically predicted (beyond leading order) to high accuracy [16], merging into the values

$$a_0^0 = 0.2198 \pm 0.0126, \quad a_0^2 = -0.0445 \pm 0.0023. \quad (1)$$

At tree level, the scattering lengths reduce to the Weinberg limits (WLs) [77]

$$a_0^0 \stackrel{\text{WL}}{=} \left. \frac{2s - M_\pi^2}{32\pi f_\pi^2} \right|_{s=4M_\pi^2} = \frac{7M_\pi^2}{32\pi f_\pi^2} \simeq 0.1565, \quad a_0^2 \stackrel{\text{WL}}{=} - \left. \frac{s - 2M_\pi^2}{32\pi f_\pi^2} \right|_{s=4M_\pi^2} = - \frac{M_\pi^2}{16\pi f_\pi^2} \simeq -0.0447, \quad (2)$$

which solely depend on the first Mandelstam variable s (evaluated at threshold, $s = 4M_\pi^2$) as well as the two (geometric) constants f_π and M_π . Thus the limit captures the isospin-two scattering length already fairly well, cf. Eq. (1).

As measure for chiral symmetry breaking, the pion decay constant f_π parametrizes the vacuum-to-hadron transition amplitude

$$\langle 0 | \mathcal{J}_A^{\mu,i}(x) | \pi^j(p) \rangle = -i\delta^{ij} f_\pi p^\mu e^{-ip \cdot x}, \quad (3)$$

which is encountered in the weak decay of the positively charged pion to an antimuon and a muon-neutrino, $\pi^+ \rightarrow \mu^+ \nu_\mu$ [14]. By virtue of Eq. (3), the axial-vector current $\mathcal{J}_A^{\mu,i}$ creates on-shell pions out of the vacuum state [the indices i, j are adjoint isospin indices; the pion triplet π^i , $i = 1, 2, 3$, is the adjoint representation of the isospin symmetry and it is related to the physical (neutral and charged) pions π^0, π^\pm via complex linear combinations [83]]. It is the algebraic complement to the (conserved) isospin current. For nonzero quark masses, we have $\partial_\mu \mathcal{J}_A^{\mu,i} \neq 0$ [5].

In the LSM, the axial-vector current $\mathcal{J}_A^{\mu,i}$ (as a function of the spacetime variable x) normally takes the form [5, 84]

$$\mathcal{J}_A^{\mu,i}(x) \Big|_{\text{pions}} = \sigma_0 \partial^\mu \pi^i(x) + \mathcal{O}(\pi^3). \quad (4)$$

Using the matrix element (3), this equation identifies (at leading order) the condensate σ_0 of the isoscalar σ -field with the pion decay constant, $\sigma_0 \equiv f_\pi$, which we exploit in the following. The condensate, in turn, is the manifestation of chiral symmetry breaking within the model.

The computation of the scattering lengths a_0^0 and a_0^2 within LSMs was frequently discussed [85], but in many cases ended rather inconclusive. Especially, the simultaneous correct prediction of the S -wave scattering lengths often fails

¹ Strictly speaking, quantum anomalies are excluded from this statement.

² The additional factor of $1/\sqrt{2}$ is the convention we use in this work.

[26–29, 86–91], where some of the considered models are extended with (axial-)vector mesons or “exotic” states like tetraquarks and glueballs (as well as include or neglect baryonic d.o.f.). This shortcoming can be attributed to the large isoscalar mass M_σ favored e.g. in Refs. [26, 27, 29] ($M_\sigma \sim 1370$ MeV, in contrast to $M_\sigma \sim 500$ MeV typically needed for a successful reproduction of the isoscalar channel within LSMs). This disagreement coming with such a heavy scalar resonance is corroborated by the introduction of vector fields, as shown in Refs. [28, 92]. The vector fields shift the σ -mass required for reproducing the isoscalar scattering length to even smaller values. Some of the cited publications then proceed to the inverse and infer the isoscalar mass from a fitting procedure of model parameters to the S -wave scattering lengths (and further data, for instance, mesonic decay constants and decay widths) [26, 92]. Others adjust (or choose) the mass “by hand,” exclusively for the purpose of obtaining reasonable results for the pion-pion scattering lengths [93, 94]. Equal sensitivity to the isoscalar mass was also observed for pion-nucleon scattering, see e.g. Ref. [68].

Of great importance for the following Sections is the analysis of the pion-pion scattering process in Ref. [28], which (partly) stimulated our work; it is a study of the low-energy limit of an extended LSM (with vector and axial-vector mesons). In this limit, the corresponding low-energy couplings and the pion-pion scattering amplitude were computed by a tree-level integration of the scalar and vector resonances based on the classical action. Due to the favored large σ -mass of the model and the preferable identification of the σ -meson with the $f_0(1370)$ -resonance, the obtained S -wave scattering lengths a_0^0 and a_0^2 were not compatible with experimental data—inviting the consideration of loop corrections.

In contrast to the aforementioned investigations, we will demonstrate throughout this paper that the present approach simultaneously meets (within errorbars) both scattering lengths—which is verifiably not achieved in numerous other linear model calculations (as stated in the previous two paragraphs). The isoscalar σ -mass, which is a model prediction (together with the scattering lengths), will end up comparably light when including loop corrections (from values of $M_\sigma > 1$ GeV within the MF and one-loop approximations towards $M_\sigma \sim 500$ MeV within the FRG computations). This finding suggests an identification of the σ -meson with the $f_0(500)$ -resonance. The σ -mass is derived from the FRG integration of quantum fluctuations within the nucleon-meson model; its value as well as those of the pion-pion scattering lengths are therefore dynamically generated and intrinsically predicted by the initialization of the integration procedure, which we tune such that chiral symmetry breaking sets in at $\Lambda_\chi = 1.2$ GeV $\simeq 4\pi f_\pi$. Hence, the layout of argumentation of this work will have the structure as listed below:

Model predictions: a_0^0 , a_0^2 , and M_σ

Model parameters (input): f_π , M_π , M_{fermions} , and chiral symmetry breaking at $\Lambda_\chi \simeq 4\pi f_\pi$

Findings: $\left\{ \begin{array}{l} \text{FRG: } a_0^0 \text{ and } a_0^2 \text{ successfully simultaneously reproduced (in the LPA'-truncation);} \\ M_\sigma \sim 500 \text{ MeV, } \sigma\text{-meson identified as the } f_0(500)\text{-resonance.} \\ \text{MF and one-loop: } a_0^0 \text{ and } a_0^2 \text{ not simultaneously reproduced;} \\ M_\sigma > 1 \text{ GeV, } \sigma\text{-meson rather associated with isoscalar resonances above 1 GeV.} \end{array} \right.$

The remainder of this manuscript is organized as follows: Sec. II is dedicated to the (parity-doublet) nucleon-meson model and its formulation in terms of the effective average action. The subsequent Sec. III deals with the theory of pion-pion scattering. The numeric results are presented in Sec. IV and a conclusion is given in Sec. V. Lastly, some technical details are summarized in Appendices A to F. We use natural units, $\hbar = c = 1$; Lorentz indices in Euclidean spacetime (denoted as \mathbb{E}^4) appear as “lower” indices only.

II. NUCLEON-MESON MODEL

The central object of the FRG is the effective average action Γ_k .³ This quantity interpolates between the classical action S in the UV (with cutoff Λ) and the quantum effective action Γ in the IR ($\Gamma_{k=\Lambda} = S$ and $\Gamma_{k=0} = \Gamma$). The index k symbolizes a sliding IR cutoff, separating low-energy from high-energy fluctuations in the Wilsonian manner. The k -dependence of Γ_k is dictated by the Wetterich equation [22],

$$\partial_k \Gamma_k = \frac{1}{2} \text{tr} \left[\left(\Gamma_k^{(2)} + R_k \right)^{-1} \partial_k R_k \right] = \frac{1}{2} \text{tr} \left(\text{circle with a cross} \right), \quad (5)$$

³ In the following, we refer to the “effective average action” simply as the “effective action,” and similarly for the “quantum effective action.”

where the superscript “(2)” indicates the second functional derivative w.r.t. the field d.o.f. The regulator function R_k introduces the cutoff scale k . It typically operates as an additional mass contribution for the low-energy modes. From Eq. (5) arises an infinite set of differential equations, which is truncated by choosing a specific ansatz for Γ_k . More technical aspects (like the regulator functions) are deferred to Appendix D.

In Eq. (5), we made use of the diagrammatic Feynman representation

$$\text{————} = \left(\Gamma_k^{(2)} + R_k \right)^{-1}, \quad \text{---}\bigotimes\text{---} = \partial_k R_k, \quad \text{---}\bigcirc\text{---}^n = \Gamma_k^{(n)} \quad (6)$$

of the propagator, the regulator insertion, and the dressed n -point vertex functions (relevant for later equations). The trace operator leads to the loop structure of the Wetterich equation (5).

A. Effective action

The effective action Γ_k of the parity-doublet nucleon-meson model reads

$$\Gamma_k [\varphi, \bar{\psi}_1, \psi_1, \bar{\psi}_2, \psi_2] = \int_x \left\{ \frac{1}{2} Z_k (\partial_\mu \varphi) \cdot \partial_\mu \varphi + V_k(\varphi^2) - h\sigma + \bar{\psi}_1 \left[Z_k^\psi \gamma_\mu \partial_\mu + y_{1,k} (\sigma + i\gamma_5 \vec{\pi} \cdot \vec{\tau}) \right] \psi_1 \right. \\ \left. + \bar{\psi}_2 \left[Z_k^\psi \gamma_\mu \partial_\mu - y_{2,k} (\sigma - i\gamma_5 \vec{\pi} \cdot \vec{\tau}) \right] \psi_2 + m_{0,k} (\bar{\psi}_1 \psi_2 + \bar{\psi}_2 \psi_1) \right\}, \quad (7)$$

with the short-hand notation $\int_x = \int d^4x$ for the (Euclidean) spacetime integration. The two Dirac fermions $(\bar{\psi}_i, \psi_i)$, $i = 1, 2$, represent a pair of “mirror-assigned” flavor doublets of the chiral $\text{SU}(2) \times \text{SU}(2)$ -symmetry [and its diagonal $\text{SU}(2)$ isospin subgroup], cf. Appendix A. Both are defined to be parity-even. The bosonic d.o.f. are collected in the irreducible (linear) representation $(2, 2)$ of chiral symmetry, $\varphi = (\vec{\pi}, \sigma) = (\pi^1, \pi^2, \pi^3, \sigma)$. The three Pauli matrices are denoted as $\vec{\tau}$.

Equation (7) constitutes an LPA'-ansatz, that includes a scale-dependent potential V_k , Yukawa couplings $y_{1,k}$ and $y_{2,k}$, the chiral-invariant mass $m_{0,k}$, as well as bosonic and fermionic (field-independent) wave-function renormalization factors Z_k and Z_k^ψ , respectively. The parameter $m_{0,k} \neq 0$ generates a nonvanishing fermion mass also in the chiral-restored phase. Moreover, the nucleon-meson model exhibits explicit chiral symmetry breaking through the term proportional to $h \neq 0$, which accounts for nonzero quark masses (and a physical pion mass). Setting $Z_k = Z_k^\psi = 1$ and neglecting the scale dependence of $m_{0,k}$, $y_{1,k}$, and $y_{2,k}$, we call truncation (7) the LPA (local potential approximation). For the effective potential $V_k(\varphi^2)$, we use a Taylor polynomial of order $N_\alpha = 6$ (in the invariant $\varphi^2 = \vec{\pi}^2 + \sigma^2$),

$$V_k(\varphi^2) = \sum_{n=1}^{N_\alpha} \frac{\alpha_{n,k}}{n!} (\varphi^2 - \varphi_0^2)^n, \quad \alpha_{n,k} = V_k^{(n)}(\varphi_0^2), \quad (8)$$

with the coefficients $\alpha_{n,k}$, $n = 1, \dots, N_\alpha$, and the scale-independent expansion point φ_0^2 (to be chosen slightly larger than the IR minimum, i.e., $\varphi_0^2 \gtrsim f_\pi^2$). Pursuant to Refs. [38, 42, 55], this truncation goes beyond ordinary “tree-level” potentials with quartic field interactions ($N_\alpha = 2$). The (relative) numeric robustness against variations in N_α is discussed in Appendix D.

Upon condensation of the isoscalar σ -field ($\sigma \rightarrow \sigma_0 + \sigma$) and the assumption that $m_0 \neq 0$,⁴ the fermion fields—as defined above—are entangled through the nondiagonal mass matrix

$$\mathfrak{M}_\psi = \begin{pmatrix} y_1 \sigma_0 & m_0 \\ m_0 & -y_2 \sigma_0 \end{pmatrix}. \quad (9)$$

Hence, they are connected through a nondiagonal propagator structure. The fermions are disentangled to the physical parity-opposite basis, $(\psi_1, \psi_2) \rightarrow (N_+, N_-)$, by applying a parity transformation in addition to an orthogonal rotation, such that

$$\mathfrak{M}_N = \begin{pmatrix} m^+ & 0 \\ 0 & m^- \end{pmatrix}, \quad m^\pm = \frac{1}{2} \left[\pm \sigma_0 (y_1 - y_2) + \sqrt{\sigma_0^2 (y_1 + y_2)^2 + 4m_0^2} \right]. \quad (10)$$

⁴ Henceforth, we frequently leave out the subscript “ k ” for a more compact notation; the k -dependence is explicitly given in Eqs. (7) and (8). It should be clear from the context, if we refer to the respective quantity in the IR limit, $k \rightarrow 0$, or not.

For the details of this transformation, we refer again to Appendix A. In the physical basis, the fermionic part of Eq. (7) becomes

$$\begin{aligned} \Gamma[\varphi, \bar{\psi}_1, \psi_1, \bar{\psi}_2, \psi_2] \Big|_{\text{fermions}} &\longrightarrow \Gamma[\varphi, \bar{N}_+, N_+, \bar{N}_-, N_-] \Big|_{\text{fermions}} \\ &\equiv \int_x \left\{ \bar{N}_+ (Z^\psi \gamma_\mu \partial_\mu + m^+) N_+ + \bar{N}_- (Z^\psi \gamma_\mu \partial_\mu + m^-) N_- \right. \\ &\quad + \bar{N}_+ (y_\sigma^{++} \sigma + i y_\pi^{++} \gamma_5 \vec{\pi} \cdot \vec{\tau}) N_+ + \bar{N}_- (y_\sigma^{--} \sigma + i y_\pi^{--} \gamma_5 \vec{\pi} \cdot \vec{\tau}) N_- \\ &\quad \left. - \bar{N}_+ (y_\sigma^{+-} \sigma + i y_\pi^{+-} \gamma_5 \vec{\pi} \cdot \vec{\tau}) N_- + \bar{N}_- (y_\sigma^{-+} \sigma + i y_\pi^{-+} \gamma_5 \vec{\pi} \cdot \vec{\tau}) N_+ \right\}. \end{aligned} \quad (11)$$

The fermion fields N_+ and N_- represent the parity-even isospin doublet of protons and neutrons and the parity-odd chiral partners of the nucleons, respectively. Together, they form the parity doublet $N = (N_+, N_-)$. In Eq. (11), the Yukawa interactions with the bosonic d.o.f. evidently split,

$$y_\sigma^{++/--} = \frac{1}{2} \left[\pm(y_1 - y_2) + \frac{\sigma_0(y_1 + y_2)^2}{\sqrt{\sigma_0^2(y_1 + y_2)^2 + 4m_0^2}} \right], \quad (12)$$

$$y_\pi^{++/--} = \frac{1}{2} \left[\pm(y_1 + y_2) + \frac{\sigma_0(y_1^2 - y_2^2)}{\sqrt{\sigma_0^2(y_1 + y_2)^2 + 4m_0^2}} \right], \quad (13)$$

$$y_{\sigma/\pi}^{+-} \equiv y_{\sigma/\pi}^{-+} = \frac{m_0(y_1 \pm y_2)}{\sqrt{\sigma_0^2(y_1 + y_2)^2 + 4m_0^2}}. \quad (14)$$

In the limit $m_0 \rightarrow 0$, the fermion masses m^\pm consistently reduce to $m^+ = y_1 \sigma_0$ and $m^- = y_2 \sigma_0$, i.e., they are solely generated by spontaneous chiral symmetry breaking; the Yukawa couplings of Eqs. (12), (13), and (14) simplify to $y_\sigma^{++} = y_\pi^{++} = y_1$, $y_\sigma^{--} = -y_\pi^{--} = y_2$, and $y_\sigma^{+-} = y_\pi^{+-} = 0$. Thus in summary, the fermions decouple and become massless in the chiral-restored phase, $\sigma_0 \rightarrow 0$. In contrast, for $\sigma_0 \rightarrow 0$ but nonzero chiral-invariant mass $m_0 \neq 0$, one finds that $m^\pm = m_0$, $y_\sigma^{++} = y_\pi^{++} = -y_\sigma^{--} = -y_\pi^{--} = (y_1 - y_2)/2$, and $y_\pi^{+-} = y_\sigma^{+-} = -y_\pi^{-+} = -y_\sigma^{-+} = (y_1 + y_2)/2$.

The physical observables, which are computed from the effective actions (7) and (11) in the IR limit, $\Gamma \equiv \Gamma_{k=0}$, are directly related to the renormalization-group-invariant vertex functions of the generic form

$$\frac{\delta^n \Gamma_k[\phi]}{\delta \phi_1 \cdots \delta \phi_n} \prod_{i=1}^n \left(Z_k^{\phi_i} \right)^{-1/2} \Big|_{k=0} =: \frac{\delta^n \tilde{\Gamma}_k[\tilde{\phi}]}{\delta \tilde{\phi}_1 \cdots \delta \tilde{\phi}_n} \Big|_{k=0}, \quad n \in \mathbb{N}. \quad (15)$$

The object ϕ_i symbolizes any field component (with all its different vector-space indices collected in the index i) of the model at hand and $Z_k^{\phi_i}$ is the corresponding wave-function renormalization. This rescaling of vertex functions through the $Z_k^{\phi_i}$ -factors is absorbed into the renormalized fields $\tilde{\phi}_i := (Z_k^{\phi_i})^{1/2} \phi_i$, as shown on the right-hand side of the definition (15). Furthermore, the effective action $\tilde{\Gamma}_k$ is obtained by replacing the field ϕ accordingly. The physical squared boson and fermion masses, which stem from the two-point functions, are then given by the following expressions:

$$M_\pi^2 \equiv \frac{m_\pi^2}{Z} = \frac{2V'}{Z}, \quad M_\sigma^2 \equiv \frac{m_\sigma^2}{Z} = \frac{2V' + 4\sigma_0^2 V''}{Z}, \quad (M^\pm)^2 \equiv \frac{(m^\pm)^2}{(Z^\psi)^2}. \quad (16)$$

Likewise, the renormalized mass parameter M_0 and the renormalized Yukawa couplings (exemplified by the coupling $\tilde{y}_\sigma^{++/--}$) are deduced as

$$M_0 \equiv \frac{m_0}{Z^\psi}, \quad \tilde{y}_\sigma^{++/--} \equiv \frac{y_\sigma^{++/--}}{Z^\psi Z^{1/2}} \equiv \frac{1}{2} \left[\pm(\tilde{y}_1 - \tilde{y}_2) + \frac{\tilde{\sigma}_0(\tilde{y}_1 + \tilde{y}_2)^2}{\sqrt{\tilde{\sigma}_0^2(\tilde{y}_1 + \tilde{y}_2)^2 + 4M_0^2}} \right]. \quad (17)$$

While renormalized couplings generally carry a tilde (“ $\tilde{\cdot}$ ”), we simply use capital letters for the renormalized masses M_π , M_σ , M_0 , and M^\pm .

B. Vacuum manifold, stereographic projections, and the NLSM

With the local isomorphisms to special orthogonal groups, two-flavor chiral symmetry breaking is characterized by the breaking scheme $\text{SO}(4) \rightarrow \text{SO}(3)$. The vacuum manifold of the $\text{SO}(4)$ -invariant bosonic part of the effective action, i.e., the set of energetically degenerate vacuum states of the system, is given by the three-sphere S^3 . It is then convenient to consider the bosonic interactions in terms of stereographic projections, which is a common set of coordinates on S^3 . This rewriting foremost yields an intuitive understanding of the underlying geometric concepts: The radius θ of the three-sphere S^3 is the “massive” mode in this picture and it physically corresponds to the original σ -field (which manifests itself in the fact that $M_\theta \equiv M_\sigma$). Its fluctuations are thus radial excitations of the sphere around its physical ground state with $\theta = f_\pi$. Additionally, if the dynamics of the radius is effectively frozen by fixing it to the pion decay constant, one readily recovers the NLSM, which is the fundamental building block of ChPT. The NLSM exclusively “lives” on S^3 .

The pions geometrically describe an $\text{SO}(4)$ -rotation, traveling on the sphere S^3 with constant radius θ . The (pionic) coset generators of $\text{SO}(4)/\text{SO}(3)$, which correspond to the axial charge operators derived from the axial current \mathcal{J}_A^μ , rotate one vacuum state into another, all of which are physically equivalent. The remaining generators of the residual $\text{SO}(3)$ -symmetry “annihilate” the vacuum, such that $\text{SO}(3)$ -rotations around the axis of the position vector pointing onto S^3 leave the actual vacuum state invariant. The pionic $\text{SO}(4)$ -matrix and the decomposition of the $\mathfrak{so}(4)$ -algebra into the coset generators and the $\mathfrak{so}(3)$ -subalgebra are presented in Appendix B.

Concretely, we use (properly rescaled) stereographic projections from the south pole $\tilde{\varphi} = (0, 0, 0, -\theta)$,

$$\Pi^a = 2f_\pi \frac{\tilde{\pi}^a}{\theta + \tilde{\sigma}}, \quad a = 1, 2, 3, \quad \theta = |\tilde{\varphi}| = \sqrt{\tilde{\pi}^2 + \tilde{\sigma}^2}. \quad (18)$$

Substituting the fields $\tilde{\varphi}$ with the coordinates defined in Eq. (18) and using the metric tensor $g_{\bar{a}\bar{b}}(\Pi)$ on S^3 (with the “curved” coset indices $\bar{a}, \bar{b} = 1, 2, 3$),

$$g_{\bar{a}\bar{b}}(\Pi) = \frac{16f_\pi^2}{(4f_\pi^2 + \Pi^2)^2} \delta_{\bar{a}\bar{b}} = \delta_{\bar{a}\bar{b}} \left[\frac{1}{f_\pi^2} - \frac{\Pi^2}{2f_\pi^4} + \frac{3\Pi^4}{16f_\pi^6} + \mathcal{O}(\Pi^6) \right], \quad (19)$$

the bosonic part of the (renormalized) nucleon-meson model (7) is converted into $\tilde{\Gamma}_{\text{stereographic}}[\Pi, \theta]$, with

$$\tilde{\Gamma}_{\text{stereographic}}[\Pi, \theta] := \int_x \left[\frac{\theta^2}{2} g_{\bar{a}\bar{b}}(\Pi) (\partial_\mu \Pi^{\bar{a}}) \partial_\mu \Pi^{\bar{b}} + \frac{1}{2} (\partial_\mu \theta) \partial_\mu \theta + \tilde{V}_k(\theta^2) - \tilde{h}\theta \frac{4f_\pi^2 - \Pi^2}{4f_\pi^2 + \Pi^2} \right]. \quad (20)$$

Note that the pions Π carry the indices $\{\bar{a}, \bar{b}, \dots\}$ in their role as mappings between (Euclidean) spacetime and the manifold S^3 [to be distinguished from the Lie-algebra indices $\{a, b, \dots\}$]. The notation $\Pi^2 \equiv \Pi \cdot \Pi$ means $\delta_{\bar{a}\bar{b}} \Pi^{\bar{a}} \Pi^{\bar{b}}$; other technical details are found in Appendix B.

From this stage one immediately recovers the effective action of the NLSM by forcing the radius θ of the three-sphere to be equal to the pion decay constant,

$$\theta = f_\pi = \text{const.}, \quad (21)$$

which restricts the dynamics to the vacuum manifold S^3 . Up to irrelevant constants and setting $\tilde{h} = 0$, the effective action then reads

$$\tilde{\Gamma}_{\text{NLSM}}[\Pi] = \int_x \frac{f_\pi^2}{2} g_{\bar{a}\bar{b}}(\Pi) (\partial_\mu \Pi^{\bar{a}}) \partial_\mu \Pi^{\bar{b}} = \int_x \left[\frac{1}{2} (\partial_\mu \Pi) \cdot \partial_\mu \Pi - \frac{1}{4f_\pi^2} \Pi^2 (\partial_\mu \Pi) \cdot \partial_\mu \Pi + \mathcal{O}(\Pi^6) \right]. \quad (22)$$

The last term in Eq. (20) proportional to the parameter \tilde{h} adds momentum-independent pion self-interactions to the (purely momentum-dependent) action (22) of the NLSM, i.e.,

$$\tilde{h} \left[f_\pi - \frac{\Pi^2}{2f_\pi} + \frac{\Pi^4}{8f_\pi^3} + \mathcal{O}(\Pi^6) \right]. \quad (23)$$

The squared pion mass is thus given by⁵

$$M_\pi^2 = \frac{\tilde{h}}{f_\pi} \equiv \frac{h}{Z^{1/2} f_\pi}, \quad (24)$$

⁵ We stick to the small Greek letter “ π ” in the subscript of the physical (coordinate-independent) quantities f_π and $M_\pi \equiv M_\Pi$ throughout the entire paper. The pion-pion scattering amplitude $\mathcal{M}_{\pi\pi}$ is analogously denoted.

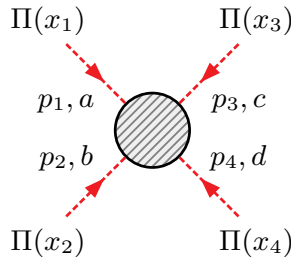


Figure 1. Pion-pion scattering process with incoming pion momenta p_n , $n = 1, \dots, 4$, and isospin indices $\{a, b, c, d\}$.

whereas the squared mass of the θ -field in Eq. (20) is calculated from the (renormalized) effective potential \tilde{V} ,⁶

$$M_\theta^2 = 2\tilde{V}' + 4f_\pi^2\tilde{V}'' \equiv M_\sigma^2. \quad (25)$$

The physical vacuum configuration of the nucleon-meson model is attained at the north pole $\tilde{\varphi} = (0, 0, 0, \theta)$,

$$\Pi^a|_{\tilde{\sigma}=\tilde{\sigma}_0, \tilde{\pi}^a=0} = 0 \quad \forall a, \quad \theta|_{\tilde{\sigma}=\tilde{\sigma}_0, \tilde{\pi}^a=0} = \tilde{\sigma}_0 = f_\pi, \quad (26)$$

where the last equation is the identification of the (renormalized) isoscalar condensate $\tilde{\sigma}_0$ with the pion decay constant [according to Eqs. (3) and (4)]. Of course, this configuration was already anticipated in the discussion of this Section. It a posteriori justifies the Taylor expansion for small Π^2 ($\Pi^2 \ll 1$; see also Fig. 6 in Appendix B), that we implicitly employed in Eqs. (19), (23), and (24).

The reformulation of the (parity-doublet) nucleon-meson model through the stereographic coordinates allows one to compute the pion-pion amplitude in a “chiral expansion” similar to the NLSM and ChPT. It pointedly elaborates on common geometric features of the linear and nonlinear realizations of chiral symmetry. In the following, we make use of these concepts and perform an expansion of the effective action in terms of “small” (squared) pion fields and pion momenta (derivatives acting on the pion fields), after the integration of quantum nucleon-meson fluctuations based on Eq. (5). Although other choices of coordinates, including that in the original formulation (7), are still valid and do not affect the physical outcome of the calculation, this particular choice allows us to explicitly demonstrate the convergence of the above formalism and work out subtleties with higher-derivative pion self-interactions and their influence on the analytic and numeric accuracy.

III. PION-PION SCATTERING

The amplitude $\mathcal{M}_{\pi\pi}$ of pion-pion scattering ($\Pi^a \Pi^b \rightarrow \Pi^c \Pi^d$), graphically illustrated in Fig. 1, is constrained by Lorentz and crossing symmetries to

$$\mathcal{M}_{\pi\pi}^{abcd}(s, t, u) = i\mathfrak{A}(s, t, u)\delta^{ab}\delta^{cd} + i\mathfrak{A}(t, u, s)\delta^{ac}\delta^{bd} + i\mathfrak{A}(u, s, t)\delta^{ad}\delta^{bc}, \quad (27)$$

with the adjoint isospin indices $\{a, b, c, d\}$ and the Mandelstam variables

$$\begin{aligned} s &= (p_1 + p_2)^2 = (p_3 + p_4)^2, \\ t &= (p_1 + p_3)^2 = (p_2 + p_4)^2, \\ u &= (p_1 + p_4)^2 = (p_2 + p_3)^2 \end{aligned} \quad (28)$$

with incoming pion momenta p_n , $n = 1, \dots, 4$ [16].

Working with the effective action Γ , it is adequate to compute the scattering amplitude $\mathcal{M}_{\pi\pi}$ at tree level.⁷ The effects of loop corrections are entirely taken into account by using the “dressed” propagators and vertices in place of the classical ones (derived from the classical action S) [95]. The notion “tree level” refers to the topological form of the Feynman diagrams—generally speaking, irrespective of the underlying action functional and not restricted to

⁶ We use the masses M_θ and M_σ synonymously in the later Sections.

⁷ The quantum effective action Γ corresponds to the renormalized action functional $\tilde{\Gamma}$ from Sec. II. We omit the tilde from now on.

the ‘‘standard’’ perturbative sense. Our strategy is therefore to integrate the FRG equation (5) in order to obtain the effective action Γ and subsequently focus on the bosonic part of the truncation (7) in its stereographic picture (20) in order to compute the amplitude $\mathcal{M}_{\pi\pi}$ in an expansion in pion fields and pion momenta. The fermions (nucleons and their chiral partners) do not enter the tree-level scattering diagrams; their loop effects are captured by the dressed bosonic vertices. In consequence, this approach goes much beyond the common MF and one-loop levels.

At leading order of the chiral expansion (equivalent to tree level) [16, 78–82], the amplitude \mathfrak{A} on the right-hand side of Eq. (27) solely depends on the first Mandelstam variable s , i.e., $\mathfrak{A}(s, t, u) \equiv \mathfrak{A}(s)$. In the partial-wave analysis of \mathfrak{A} , this implies that only the S - and P -waves (with angular-momentum quantum numbers $l = 0$ and $l = 1$, respectively) are nonzero [16, 81]. At threshold, $s = 4M_\pi^2$, the tree-level amplitude even further reduces to the isospin-zero ($I = 0$) and isospin-two ($I = 2$) S -wave contributions. More precisely, the two relevant scattering lengths a_0^0 and a_0^2 are related to the partial-wave amplitudes t_l^I as follows [28]:⁸

$$\begin{aligned} a_0^0 &= t_0^0|_{s=4M_\pi^2, t=u=0} = \frac{1}{32\pi} [3\mathfrak{A}(s, t, u) + \mathfrak{A}(t, u, s) + \mathfrak{A}(u, s, t)] \Big|_{s=4M_\pi^2, t=u=0} \\ &= \frac{1}{32\pi} [3\mathfrak{A}(4M_\pi^2) + 2\mathfrak{A}(0)], \end{aligned} \quad (29)$$

$$a_0^2 = t_0^2|_{s=4M_\pi^2, t=u=0} = \frac{1}{32\pi} [\mathfrak{A}(t, u, s) + \mathfrak{A}(u, s, t)] \Big|_{s=4M_\pi^2, t=u=0} = \frac{1}{16\pi} \mathfrak{A}(0). \quad (30)$$

The tree-level pion-pion scattering amplitude (in Minkowski spacetime \mathbb{M}^4) within the effective action (20) is determined by the Feynman diagrams

$$\begin{aligned} \mathcal{M}_{\pi\pi}^{abcd} &\sim \begin{array}{c} \Pi \quad \Pi \\ \diagdown \quad \diagup \\ \text{---} \text{---} \\ \diagup \quad \diagdown \\ \Pi \quad \Pi \end{array} = \begin{array}{c} \Pi \quad \Pi \\ \diagdown \quad \diagup \\ \text{---} \text{---} \\ \diagup \quad \diagdown \\ \Pi \quad \Pi \end{array} + \underbrace{\begin{array}{c} \Pi \quad \Pi \\ \diagdown \quad \diagup \\ \text{---} \text{---} \\ \diagup \quad \diagdown \\ \Pi \quad \Pi \end{array}}_{s-, t-, \text{ and } u\text{-channel}} \\ &= i\Gamma_{\text{PIIIII}}^{(4)abcd}(x_1, x_2, x_3, x_4) + \underbrace{\int_{z_1} \int_{z_2} i\Gamma_{\text{PIII}\theta}^{(3)ab}(x_1, x_2, z_1) G_{\theta\theta}(z_1, z_2) i\Gamma_{\text{PIII}\theta}^{(3)cd}(x_3, x_4, z_2)}_{s\text{-channel}} \\ &\quad + t\text{-channel} + u\text{-channel}, \end{aligned} \quad (31)$$

where we left out the pion-leg specifications (cf. Fig. 1) in the first line to enhance readability. In the second line, we reintroduced the adjoint isospin indices $\{a, b, c, d\}$ as well as the spacetime variables x_n , $n = 1, \dots, 4$. The propagator of the θ -field, which is given by the inverse two-point function, is denoted by $G_{\theta\theta}$ and the imaginary unit i attached to the vertex functions is a typical convention in \mathbb{M}^4 . The Minkowskian version of the (Euclidean) effective action Γ , sitting on the vertices in the above diagrams, is produced by a naive inverse Wick rotation, $\Gamma \rightarrow -i\Gamma$, which is tacitly carried out but not labeled separately in the course of the current Section ($\mathbb{E}^4 \rightarrow \mathbb{M}^4$).

The summation of all relevant tree-level diagrams for the four-pion amplitude, i.e., with at most a single θ -exchange, is equivalent to eliminating the θ -field by evaluating the effective action Γ at its stationary point (w.r.t. θ),

$$\left. \frac{\delta\Gamma}{\delta\theta} \right|_{\theta_{\text{sol}}} = 0 \quad \Rightarrow \quad \Gamma_{\text{sol}}[\Pi] := \Gamma[\Pi, \theta] \Big|_{\theta=\theta_{\text{sol}}[\Pi]} \quad \Rightarrow \quad \begin{array}{c} \Pi \quad \Pi \\ \diagdown \quad \diagup \\ \text{---} \text{---} \\ \diagup \quad \diagdown \\ \Pi \quad \Pi \end{array} \equiv i\Gamma_{\text{sol}}^{(4)abcd}(x_1, x_2, x_3, x_4). \quad (32)$$

Thus the summation collapses to a single dressed vertex, including bosonic and fermionic quantum fluctuations. The equation of motion (EOM) in Eq. (32) has the form ($\square = \partial_\mu \partial^\mu$)

$$\frac{\delta\Gamma}{\delta\theta} = 0 \quad \Rightarrow \quad \xi + \epsilon \left[\frac{\square\xi}{M_\pi^2} - \frac{\xi + f_\pi}{M_\pi^2} g_{\bar{a}\bar{b}} (\partial_\mu \Pi^{\bar{a}}) \partial^\mu \Pi^{\bar{b}} + 2f_\pi \frac{\Pi^2}{4f_\pi^2 - \Pi^2} + \frac{\mathcal{O}(\xi^2)}{M_\pi^2} \right] = 0 \quad (33)$$

⁸ The scattering length $a_0^1 \sim \mathfrak{A}(t, u, s) - \mathfrak{A}(u, s, t)$ vanishes at threshold, $a_0^1 = 0$. The term ‘‘scattering length’’ originates from its canonical definition $a_l^I \sim t_l^I/M_\pi$, which has the dimension of length (inverse energy). In the chiral limit, $M_\pi \rightarrow 0$, a_0^0 and a_0^2 are zero.

after shifting the θ -field by its physical expansion point, $\xi := \theta - f_\pi$. We furthermore renamed the dimensionless ratio M_π^2/M_σ^2 as ϵ , for which we take a small value as granted, $\epsilon \ll 1$. This holds at least for the masses quoted in Ref. [3],

$$\epsilon := \frac{M_\pi^2}{M_\sigma^2}, \quad \epsilon_{\text{phys}} \sim \frac{(138 \text{ MeV})^2}{(475 \text{ MeV})^2} \simeq 0.0844. \quad (34)$$

Following Ref. [32], the solution to the EOM is a power series in the small parameter ϵ ,

$$\theta_{\text{sol}} = f_\pi + \xi_{\text{sol}}, \quad \xi_{\text{sol}} = \epsilon \xi_1 + \epsilon^2 \xi_2 + \epsilon^3 \xi_3 + \epsilon^4 \xi_4 + \epsilon^5 \xi_5 + \dots, \quad (35)$$

which itself is a functional of the Π -fields, $\xi_{\text{sol}}[\Pi]$. The expansion coefficients ξ_n , $n \in \mathbb{N}$, are obtained in an iterative manner, namely,

$$\xi_1 = \frac{f_\pi}{M_\pi^2} g_{\bar{a}\bar{b}} (\partial_\mu \Pi^{\bar{a}}) \partial^\mu \Pi^{\bar{b}} - 2f_\pi \frac{\Pi^2}{4f_\pi^2 - \Pi^2}, \quad (36)$$

$$\xi_2 = -\frac{1}{M_\pi^2} \left[\square - g_{\bar{a}\bar{b}} (\partial_\mu \Pi^{\bar{a}}) \partial^\mu \Pi^{\bar{b}} \right] \xi_1, \quad (37)$$

$$\xi_3 = -\frac{1}{M_\pi^2} \left\{ \left[\square - g_{\bar{a}\bar{b}} (\partial_\mu \Pi^{\bar{a}}) \partial^\mu \Pi^{\bar{b}} \right] \xi_2 + \text{terms} \propto \xi_1^2 \right\}, \quad (38)$$

$$\xi_4 = -\frac{1}{M_\pi^2} \left\{ \left[\square - g_{\bar{a}\bar{b}} (\partial_\mu \Pi^{\bar{a}}) \partial^\mu \Pi^{\bar{b}} \right] \xi_3 + \text{terms} \propto \xi_1^3 + \text{terms} \propto \xi_1 \xi_2 \right\}, \quad (39)$$

$$\xi_5 = -\frac{1}{M_\pi^2} \left\{ \left[\square - g_{\bar{a}\bar{b}} (\partial_\mu \Pi^{\bar{a}}) \partial^\mu \Pi^{\bar{b}} \right] \xi_4 + \text{terms} \propto \xi_1^4 + \text{terms} \propto \xi_1^2 \xi_2 + \text{terms} \propto \xi_1 \xi_3 + \text{terms} \propto \xi_2^2 \right\}, \quad (40)$$

and so forth. At order $n > 1$, we deduce the general (iterative) solution

$$\xi_n = -\frac{1}{M_\pi^2} \left\{ \left[\square - g_{\bar{a}\bar{b}} (\partial_\mu \Pi^{\bar{a}}) \partial^\mu \Pi^{\bar{b}} \right] \xi_{n-1} + \underbrace{\text{terms} \propto \xi_1^{n-1} + \dots}_{\mathfrak{P}(n-1) - 1 \text{ possibilities}} \right\}, \quad (41)$$

with the (number-theoretical) partition function $\mathfrak{P}(n)$ of the integer n . The solution of $\mathcal{O}(\epsilon^n)$ manifestly involves pion derivatives up to $\mathcal{O}(\partial^{2(n+1)})$. This subtle point already leads to the expectation that we need to expand the effective action Γ_{sol} to that order in pion derivatives, if we want to achieve analytic accuracy at $\mathcal{O}(\epsilon^n)$ for the scattering lengths. Indeed, solving Eq. (33) for ξ along the above iterative scheme, expanding the resulting pionic effective action Γ_{sol} up to $\mathcal{O}(\Pi^4, \partial^{12})$, and extracting the four-pion amplitude $\mathfrak{A}(s)$ out of the fourth functional derivative of Γ_{sol} , we find for the S -wave scattering lengths

$$\mathcal{O}(p^0): \quad a_0^0 = \frac{5M_\pi^2}{32\pi f_\pi^2} (1 + \epsilon), \quad (42)$$

$$a_0^2 = \frac{M_\pi^2}{16\pi f_\pi^2} (1 + \epsilon); \quad (43)$$

$$\mathcal{O}(p^2): \quad a_0^0 = \frac{M_\pi^2}{32\pi f_\pi^2} (7 + 9\epsilon + 12\epsilon^2), \quad (44)$$

$$a_0^2 = -\frac{M_\pi^2}{16\pi f_\pi^2} (1 + 3\epsilon); \quad (45)$$

$$\mathcal{O}(p^4): \quad a_0^0 = \frac{M_\pi^2}{32\pi f_\pi^2} (7 + 29\epsilon + 60\epsilon^2 + 48\epsilon^3), \quad (46)$$

$$a_0^2 = -\frac{M_\pi^2}{16\pi f_\pi^2} (1 - \epsilon); \quad (47)$$

$$\mathcal{O}(p^6): \quad a_0^0 = \frac{M_\pi^2}{32\pi f_\pi^2} (7 + 29\epsilon + 108\epsilon^2 + 240\epsilon^3 + 192\epsilon^4); \quad (48)$$

$$\mathcal{O}(p^8): \quad a_0^0 = \frac{M_\pi^2}{32\pi f_\pi^2} (7 + 29\epsilon + 108\epsilon^2 + 432\epsilon^3 + 960\epsilon^4 + 768\epsilon^5); \quad (49)$$

Table I. Analytic errors $\Delta_{\text{analytic}}^{I,m}$ in units of $M_\pi^2/(32\pi f_\pi^2)$ and $M_\pi^2/(16\pi f_\pi^2)$ for $I = 0$ and $I = 2$, respectively.

Isospin I	$\mathcal{O}(p^0)$	$\mathcal{O}(p^2)$	$\mathcal{O}(p^4)$	$\mathcal{O}(p^6)$	$\mathcal{O}(p^8)$	$\mathcal{O}(p^{10})$	$\mathcal{O}(p^{12})$
$I = 0$	$2 + 24\epsilon$	$20\epsilon + 96\epsilon^2$	$48\epsilon^2 + 384\epsilon^3$	$192\epsilon^3 + 1536\epsilon^4$	$768\epsilon^4 + 6144\epsilon^5$	$3072\epsilon^5 + 24576\epsilon^6$	$12288\epsilon^6 + 98304\epsilon^7$
$I = 2$	2	4ϵ	zero	zero	zero	zero	zero

$$\mathcal{O}(p^{10}): \quad a_0^0 = \frac{M_\pi^2}{32\pi f_\pi^2} (7 + 29\epsilon + 108\epsilon^2 + 432\epsilon^3 + 1728\epsilon^4 + 3840\epsilon^5 + 3072\epsilon^6); \quad (50)$$

$$\mathcal{O}(p^{12}): \quad a_0^0 = \frac{M_\pi^2}{32\pi f_\pi^2} (7 + 29\epsilon + 108\epsilon^2 + 432\epsilon^3 + 1728\epsilon^4 + 6912\epsilon^5 + 15360\epsilon^6 + 12288\epsilon^7); \quad (51)$$

⋮

The indication $\mathcal{O}(p^m)$, m even, stands for the expansion order in the small pion momentum p (via the correspondence between derivatives acting on the Π -fields and the pion momentum, $\partial \leftrightarrow p$). The outcome of this procedure in Eqs. (42) to (51) can be systematically compared to the exact (coordinate-independent) tree-level scattering lengths of the LSM [30, 33, 94] [cf. Eq. (C26) in Appendix C],

$$\begin{aligned} a_0^0 &= \frac{M_\pi^2}{32\pi f_\pi^2} (\epsilon - 1) \left(\frac{9}{4\epsilon - 1} + 2 \right) \stackrel{\epsilon < 1/4}{\equiv} \frac{M_\pi^2}{32\pi f_\pi^2} (1 - \epsilon) \left[7 + 9 \sum_{n=1}^{\infty} (4\epsilon)^n \right] \\ &= \frac{M_\pi^2}{32\pi f_\pi^2} (7 + 29\epsilon + 108\epsilon^2 + 432\epsilon^3 + 1728\epsilon^4 + 6912\epsilon^5 + 27648\epsilon^6 + 110592\epsilon^7) + \mathcal{O}(\epsilon^8), \end{aligned} \quad (52)$$

$$a_0^2 = -\frac{M_\pi^2}{16\pi f_\pi^2} (1 - \epsilon). \quad (53)$$

In the first line of Eq. (52), we have expressed the scattering length a_0^0 through a geometric series, which is convergent for $\epsilon < 1/4$. The second line confirms our statement about the analytic accuracy; for instance, at $\mathcal{O}(p^2)$ and higher, the WLs of Eq. (2) are reproduced for $\epsilon \rightarrow 0$, whereas this is not the case at $\mathcal{O}(p^0)$. From $\mathcal{O}(p^4)$ on, the isospin-two scattering length a_0^2 matches the exact value (53), as expected (as being a polynomial of order ϵ). This also explains why we have cut out a_0^2 at higher orders, since it does not change anymore. In total, we have to take pion momenta of $\mathcal{O}(p^{12})$ into account—as predicted—in order to obtain the correct numeric prefactors up to ϵ^5 during the expansion of the (nonlinear) pion action Γ_{sol} , cf. Eqs. (51) and (52). The (exact) tree-level scattering lengths (52) and (53) are calculated in terms of stereographic coordinates in Appendix C, where furthermore the proof of coordinate independence of the (on-shell) four-point function is given—thereby showing the universal character of the tree-level relations.

The deviations among the numeric prefactors at $\mathcal{O}(p^m)$ define the “analytic” and “numeric” errors

$$\Delta_{\text{analytic}}^{I,m} = \text{abs} \left[a_0^I \Big|_{\text{exact; expanded up to } \epsilon^{m/2+1}} - a_0^I \Big|_{\mathcal{O}(p^m)} \right], \quad (54)$$

$$\Delta_{\text{numeric}}^{I,m} = \text{abs} \left[a_0^I \Big|_{\text{exact}} - a_0^I \Big|_{\mathcal{O}(p^m)} \right]. \quad (55)$$

Per definition, we then have the following identities:

$$\Delta_{\text{numeric}}^{0,m} \equiv \Delta_{\text{analytic}}^{0,m} + \mathcal{O}(\epsilon^{m/2+2}), \quad (56)$$

$$\Delta_{\text{numeric}}^{2,m} \equiv \Delta_{\text{analytic}}^{2,m},$$

where the first implies that $\Delta_{\text{numeric}}^{0,m} \rightarrow \Delta_{\text{analytic}}^{0,m}$ for large m . The second identity in Eq. (56) immediately holds, since the isospin-two scattering length is a polynomial of degree one. The analytic errors are collected in Table I.

The elimination of the θ -field with the EOM (32) in favor of pionic interactions generates various higher-derivative couplings in the effective action Γ_{sol} , in addition to the ones from the metric (19) and Eq. (23). E.g., there principally is a single four-pion interaction at $\mathcal{O}(p^0)$ and three different term structures at $\mathcal{O}(p^2)$, respectively,

$$\mathcal{O}(p^0): \quad \Pi^4; \quad \mathcal{O}(p^2): \quad \Pi^2 \Pi \cdot \square \Pi, \quad \Pi^2 (\partial_\mu \Pi) \cdot \partial^\mu \Pi, \quad (\Pi \cdot \partial_\mu \Pi)^2. \quad (57)$$

For higher momentum orders, the amount of (possible) four-pion interaction terms “rapidly” increases, see Appendix F, and this might lead to intricacies when analytically computing the effective action Γ_{sol} . In fact, this is the reason why we stopped the expansion at $\mathcal{O}(p^{12})$, as the number of pion terms already went up to 3335.⁹ The dimensionless expansion parameter ϵ lets us numerically determine the “radius of convergence” w.r.t. the running energy-momentum scale k in Sec. IV, since the dynamic ratio M_π^2/M_σ^2 asymptotically tends towards one, $\epsilon \rightarrow 1$, in the chiral-restored phase. It thereby crosses the critical value of $\epsilon = 1/4$, which signals the transition from convergence ($\epsilon < 1/4$) to divergence ($\epsilon \geq 1/4$) of the geometric series—hence enclosing the predictability of the scattering lengths within the convergent energy region of the pionic effective action,

$$\epsilon = \frac{M_\pi^2}{M_\sigma^2} < 1/4. \quad (58)$$

Taking the limit $M_\sigma \rightarrow \infty$ ($\epsilon \rightarrow 0$ for nonzero and finite M_π), such that

$$\theta = f_\pi \equiv \lim_{M_\sigma \rightarrow \infty} \theta_{\text{sol}}, \quad (59)$$

we consistently arrive again at the WLs of Eq. (2),

$$\lim_{M_\sigma \rightarrow \infty} a_0^0 = \frac{7M_\pi^2}{32\pi f_\pi^2}, \quad \lim_{M_\sigma \rightarrow \infty} a_0^2 = -\frac{M_\pi^2}{16\pi f_\pi^2}. \quad (60)$$

These correspond to the tree-level scattering lengths within the NLSM (with pionic mass contribution), i.e.,

The diagrammatic equation (61) shows the decomposition of a four-pion contact term. On the left, a shaded circle with four external pions (labeled Π) is equated to the sum of two terms. The first term is a four-pion contact term with a circle containing the number 4, labeled 'LSM'. The second term is a θ -exchange diagram with two internal pions (circles containing 3) and a dashed line between them labeled θ , also labeled 'LSM'. An arrow labeled $M_\sigma \rightarrow \infty$ points to the right, where the sum of the two LSM terms is equated to a single four-pion contact term with a circle containing the number 4, labeled 'NLSM'.

where the θ -exchange diagram represents the s -, t -, and u -channel. Finding corrections to Eq. (60) (at order p^4 and higher) requires the extension of the (leading-order) NLSM to ChPT, involving the low-energy constants of QCD [78–82]. In the linear realization, one would have to explicitly compute the flow of higher-derivative couplings, which translate into covariant derivatives of the (pseudo-)Nambu-Goldstone fields [38, 40, 52].

IV. NUMERIC RESULTS

As announced in the Introduction, we compute and compare the scattering lengths a_0^0 and a_0^2 in different approximations (or truncations). Following the strategy from Sec. III, we distinguish four cases (the first two of which itemized together):

- FRG (LPA, LPA’): The flow equations for the Taylor coefficients α_n , $n = 1, \dots, N_\alpha$, of the potential (8) are solved in the LPA and LPA’ truncations. The latter further includes the flow of the wave-function renormalization factors, the Yukawa couplings, and the chiral-invariant mass parameter. After the integration procedure, we translate the resulting effective action Γ into the stereographic form (20) and deduce the scattering lengths (as described above). The scaling of the effective action Γ_k even permits the evaluation of the scattering lengths on all k -scales.
- One-loop approximation: By replacing the second functional derivative on the right-hand side of Eq. (5) with the classical two-point function, we can analytically integrate the equation, once the initial couplings are fixed,

$$\Gamma_k^{(2)} \longrightarrow S^{(2)} \quad \Rightarrow \quad \Gamma_{\text{one-loop}} - \Gamma_{\Lambda, \text{one-loop}} = \frac{1}{2} \text{tr} \left\{ \ln S^{(2)} - \ln \left[S^{(2)} + R_\Lambda \right] \right\}. \quad (62)$$

In Eq. (62), we plugged in the regulator property $R_{k=0} = 0$ (see Appendix D) and recognize the usual one-loop “trace-log” formula (plus a regulator term) [96]; see furthermore Appendix E for the analytic integration of the flow equation for the effective potential. We then proceed with the scattering lengths as in the first item.

⁹ Though the number of actually generated term structures depends on the chosen coordinates and turns out to be smaller.

Table II. IR observables obtained from the integration of momentum modes as compared to the PDG [3] and to the tree-level fitting data used in Ref. [28].

Observable [MeV]	Ref. [28]	MF	One-loop	FRG (LPA)	FRG (LPA')	PDG
f_π	96.3 ± 0.7	91.79	91.56	91.92	91.25	$(130.2 \pm 1.2)/\sqrt{2} \simeq 92.07 \pm 0.85$
M_π	141.0 ± 5.8	140.0	140.2	139.9	138.2	$(2M_{\pi^\pm} + M_{\pi^0})/3 \simeq 138.1$
M_σ	1363	1477	1102	497	505	$M_{f_0(500)} = 475 \pm 75$
M^+	not included	938.9	938.0	939.5	936.7	$(M_{\text{proton}} + M_{\text{neutron}})/2 \simeq 938.9$
M^-	not included	1517	1514	1518	1511	$M_{N(1535)} = 1510 \pm 10$

- MF: We ignore the bosonic fluctuations on the right side of the flow equation (5), i.e., only the fermionic loop is integrated out [66, 97].¹⁰ The outcome accounts for the physics of fermions in a fixed external bosonic potential. The integration procedure follows again Eq. (62). Once more, we eventually proceed as delineated in the first item.

We adjust the integration of momentum modes such that spontaneous chiral symmetry breaking roughly occurs at $\Lambda_\chi = 1.2$ GeV in all approximations (LPA', LPA, one-loop, and MF). This guarantees qualitative comparability among them by setting a particular reference scale. With this major premise, the initial parameters are independently tuned such that physical values for the particle masses (pions, fermions) and the pion decay constant f_π are achieved in the IR limit, matching published data from the Particle Data Group (PDG) [3]—the σ -mass, in turn, is a prediction of the approximation/truncation, which is intrinsically constrained by the scale Λ_χ and the aforementioned observables. To this end, we identify the fields in truncations (7) and (11) with the lightest resonances in the PDG data featuring the respective quantum numbers. Note that, in order to find an unambiguous and compatible prediction for M_σ , we need to fix the chiral-invariant mass m_0 to a common value among all investigated approximations; see also the discussion in Appendix E. A reasonable choice for m_0 in the LPA, one-loop, and MF cases is given by the renormalized IR mass $M_0 = m_0/Z^\psi$ of the LPA'-truncation, which leads to exactly the same chiral-invariant mass and Yukawa couplings in the IR. Further details about the numeric implementation are presented in Appendices D and E.

Figure 2 shows as a function of k , the integrated flow for all four cases, from the upper limit of 1.5 GeV, which is the largest mass scale in the model [$M^- \equiv M_{N(1535)} \simeq 1.5$ GeV [3]], down to the IR limit, $k \rightarrow 0$. The IR “observables” produced by these flows are listed in Table II; they are compared to PDG data and to Ref. [28]. Intriguingly, if we require that the scale of chiral symmetry breaking roughly lies at Λ_χ (where the mass splitting between the bosons becomes evident) and that the pion mass M_π , the pion decay constant f_π , as well as the fermion masses (mostly) account for physical values, we obtain isoscalar σ -masses of around 500 MeV in the LPA and LPA' (cf. columns five and six in Table II). In contrast, the obtained σ -mass is relatively large in the MF and one-loop approximations (columns three and four; $M_\sigma > 1$ GeV), similar to the tree-level fitting result of Ref. [28] (second column). Taking the $f_0(500)$ -resonance as reference (last column), the FRG-masses (LPA and LPA') meet (within errorbars) the broad experimental value, while this not true for the MF and one-loop cases; those are rather associated with isoscalar f_0 -resonances above 1 GeV. The same holds for the tree-level σ -mass of Ref. [28], where the authors (and related publications therein) claim that it is rather the $f_0(1370)$ -resonance that should be interpreted as the chiral partner of the pions. Regarding the other IR quantities, we are able to generate reasonable values for the pion decay constant, the pion mass, and the fermion masses in all four approximations.¹¹

At the crossover transition from the chiral-broken phase in the IR ($\sigma_0 \gg 0$) to the restored phase ($\sigma_0 \rightarrow 0$), the chiral partners become degenerate in mass as one moves to the UV ($\pi \leftrightarrow \sigma$ and $N_+ \leftrightarrow N_-$), according to the discussion in Sec. II. In the LPA'-truncation [cf. Figs. 2(a) and 2(b)], the fermionic masses M^+ and M^- obviously “converge” to a scale-dependent nonzero mass, which is precisely given by the (renormalized) mass parameter $450 \text{ MeV} \lesssim M_0 \lesssim 825 \text{ MeV}$, as revealed in Appendix D. In the LPA [cf. Figs. 2(c) and 2(d)], they likewise tend to the constant value $m_0 = 824.5 \text{ MeV}$, which coincides with the renormalized IR parameter M_0 of the LPA'-truncation. Comparing the LPA and LPA' to the one-loop and MF calculations, we further observe that the evolution of the σ -mass w.r.t. the energy-momentum scale k below Λ_χ is non-monotonous for the FRG truncations, but monotonous in Figs. 2(e) to 2(h). Apparently, the successive inclusion of quantum fluctuations (from MF and one-loop towards the FRG flows) bends the curve down to smaller isoscalar meson masses in the IR. This “down bending” emerges with the self-consistent treatment of the Taylor coefficients in the integration of the flow equations; see the analysis of this feature in Fig. 7(c) in Appendix D.

¹⁰ The different approximations/truncations are taken here as definitions. It is clear that these may differ from other contexts/calculations.

¹¹ For the pion and nucleon masses, we take the arithmetic means of the PDG values (cf. the last column of Table II). This is motivated by the exact SU(2) isospin symmetry of the nucleon-meson model (7).

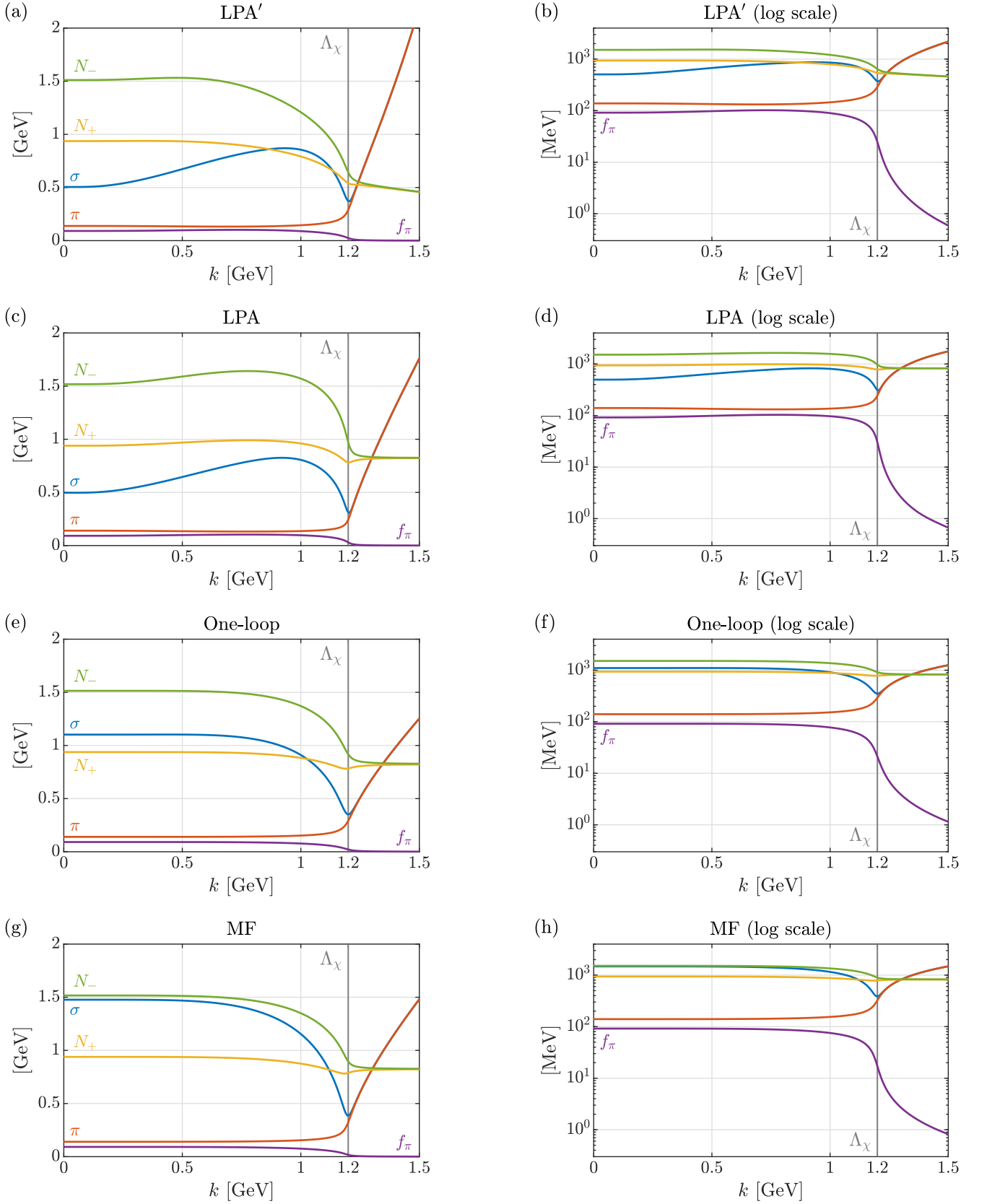


Figure 2. Scale dependence of the (renormalized) masses and the pion decay constant f_π . The vertical gray line indicates the characteristic chiral-symmetry breaking scale Λ_χ . It is kept constant in all approximations to achieve qualitative comparability. In each row, the plot on the right-hand side is the log-scale equivalent of the plot to its left.

Table III. S -wave pion-pion scattering lengths a_0^I , $I \in \{0, 2\}$, within the (parity-doublet) nucleon-meson model (for the approximations presented in Figs. 2 and 3 as well as in comparison with experimental data and ChPT).

Isospin I	Ref. [28]	MF	One-loop	FRG (LPA)	FRG (LPA')	Experiment/ChPT [16]	Experiment/ChPT [98]
$I = 0$	0.1456	0.1683	0.1749	0.2373	0.2291	0.2198 ± 0.0126	0.2196 ± 0.0096
$I = 2$	-0.0448	-0.0459	-0.0459	-0.0425	-0.0422	-0.0445 ± 0.0023	-0.0444 ± 0.0024

Furthermore, in Appendix E, we show that the down bending can also occur for some parameter sets in the one-loop approximation, which however do not meet the requirement of the chiral-symmetry breaking scale Λ_χ . The bending is associated with the similar (non-)monotonicity in the flowing pion decay constant $f_\pi \sim \sigma_0$, which is however hardly visible in Figs. 2(a) to 2(d). As for the LPA, the fermion masses in the MF and one-loop approximations approach the constant value of $m_0 = 824.5$ MeV in the UV (which equals the IR value of m_0 in these cases).

In the linear realization of chiral symmetry, the S -wave scattering lengths a_0^0 and a_0^2 are functions of M_σ via the scale-dependent ratio ϵ , as elaborated in Sec. III. Keeping the pion mass M_π and the pion decay constant f_π fixed, we plot the scattering lengths as functions of M_σ in Fig. 3; the markers on the drawn lines represent the masses of Table II and the corresponding pairs (M_σ, a_0^I) , $I \in \{0, 2\}$, are summarized in Table III. As the main result, the low-energy scattering lengths from the LPA'-flow of Fig. 2(a) [computed with Eqs. (52) and (53)] simultaneously agree (within errorbars) with the experimental/theoretical ChPT values of Refs. [16, 98], see columns six to eight.¹² The LPA-flow of Fig. 2(c) produces an isospin-zero scattering length, which is close to but slightly outside of the error band, and only the isospin-two scattering length matches the reference value.

In the third and fourth column of Table III, in contrast, the values of a_0^0 significantly differ, which we ascribe to the comparatively large mass M_σ in Figs. 2(e) to 2(h) (MF and one-loop). In general, a_0^0 strongly depends on the precise value of M_σ , as we infer from the curves in Fig. 3(a) becoming steep below $M_\sigma \sim 500$ MeV. Comparing all approximations, the value of a_0^0 is successively improved by the advancement of the truncation and the loop corrections. On the other hand, for $I = 2$ [cf. Fig. 3(b)], the curves overlap with the experimental band over a wide range of 500 MeV to the UV cutoff of 1.5 GeV. This renders the isospin-two scattering length a_0^2 almost insensitive to M_σ (for $M_\sigma \gtrsim 500$ MeV) and explains the good values found in all of the approximations (third line of Table III).

Note finally that the minor differences between the curves (i.e., the M_σ -dependence is basically robust) in Figs. 3(a) and 3(b) come from the slight variation of the ratio $M_\pi^2/(4\pi f_\pi)^2$ in the four cases,

$$\varpi := \left(\frac{M_\pi}{4\pi f_\pi} \right)^2 \sim \left(\frac{M_\pi}{\Lambda_\chi} \right)^2, \quad (63)$$

$$\varpi \stackrel{\text{LPA}'}{\simeq} 0.0145, \quad \varpi \stackrel{\text{LPA}}{\simeq} 0.0147, \quad \varpi \stackrel{\text{One-loop}}{\simeq} 0.0148, \quad \varpi \stackrel{\text{MF}}{\simeq} 0.0147. \quad (64)$$

The low-energy parameter ϖ is a measure for the pion mass M_π in units of the characteristic chiral-symmetry breaking scale $4\pi f_\pi \simeq \Lambda_\chi$ [81]; it is part of the typical low-energy expansion of the Gell-Mann-Oakes-Renner relation, putting the pion mass in direct connection to the light-flavor quark masses [81, 99]. For the physical values from the PDG [3], one has $\varpi_{\text{phys}} = 0.0142 \ll 1$.

In the limit $M_\sigma \rightarrow 0$, which is equivalent to $\epsilon \rightarrow \infty$ (for nonzero and finite M_π), the scattering lengths diverge,

$$\lim_{\epsilon \rightarrow \infty} a_0^0 \equiv \lim_{\epsilon \rightarrow \infty} a_0^2 = \infty. \quad (65)$$

This is easily verified, analytically and numerically, with the help of Eqs. (52) and (53) as well as Fig. 3. Furthermore, at the other extreme ($M_\sigma \rightarrow \infty$, $\epsilon \rightarrow 0$), the WLs of Eq. (60) are shown as horizontal dotted lines in Figs. 3(a) and 3(b); minor differences for large σ -masses between the WLs and the curves are inherited from the nonvanishing deviations in the pion mass M_π and the pion decay constant f_π w.r.t. PDG data (which is employed to calculate the numeric WLs)—or, in other words, $\varpi \neq \varpi_{\text{phys}}$. With regard to the scattering length a_0^0 in Fig. 3(a), we also run into a pole at $M_\sigma = 2M_\pi$ (vertical dotted line; corresponding to resonant σ -exchange), i.e.,

$$\begin{aligned} \lim_{\epsilon \rightarrow 1/4+0} a_0^0 &= -\infty, \\ \lim_{\epsilon \rightarrow 1/4-0} a_0^0 &= \infty, \end{aligned} \quad (66)$$

¹² The reference values in columns seven and eight are obtained by an interplay of experimental data and theoretical ChPT-input, leading to high-accuracy scattering lengths; for details see Refs. [16, 78–82, 98]. We quoted two different references for a thorough analysis.

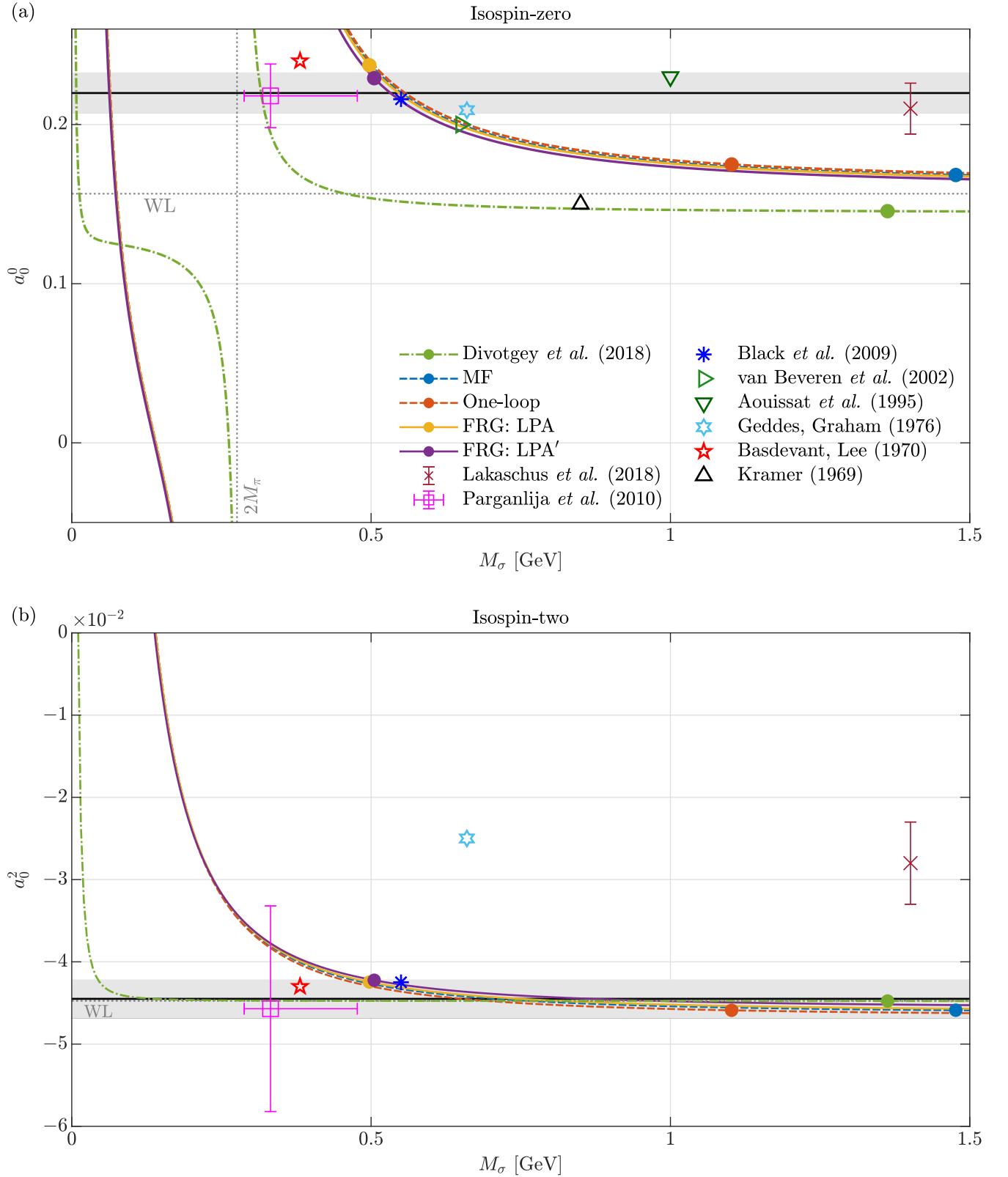


Figure 3. S -wave pion-pion scattering lengths as functions of the (renormalized) isoscalar mass M_σ . The legend in subfigure (a) applies to both panels; the markers on the solid, dashed, or dash-dotted lines, corresponding to the first five entries, indicate the computed or fitted pairs (M_σ, a_0^I) , $I \in \{0, 2\}$, of the present study and the closely related Ref. [28] (cf. also Table III). The horizontal black solid lines surrounded by the gray-shaded areas depict the respective experimental values and their uncertainty. See the main text for detailed explanations about the various (external) data points.

where the limit $\epsilon \rightarrow 1/4 \pm 0$ translates into the limit $M_\sigma \rightarrow 2M_\pi$ “from below” (+) and “from above” (-). Hence, one hits the pole when crossing the value of $\epsilon = 1/4$ during the integration process, accompanied by the onset of divergence in the geometric-series expansion (52) of the pionic effective action.

Aside from the calculated scattering lengths, Figs. 3(a) and 3(b) include external data from similar phenomenological models. The dash-dotted curve “Divotgey *et al.* (2018)” corresponds to the (extended) LSMs of Refs. [27, 28], where the (three-flavor) model parameters were fitted to mesonic masses, decay constants, and decay widths. As it involves the effect of vector and axial-vector mesons, the line in Fig. 3(a) runs fairly below our results in the domain of $M_\sigma > 2M_\pi$. It crosses the experimental band for values around $M_\sigma \sim 300$ MeV—a substantial shift to lower masses, as it was also detected in Ref. [92]. The isoscalar mass of the model, $M_\sigma = 1363$ MeV (cf. once again column two of Table II), hampers the simultaneous reproduction of the experimental scattering lengths; see the marker on the dash-dotted curve. For a_0^2 , the outcome matches the experimental band and the spin-one vector resonances remarkably augment its general agreement with the theoretical calculation at lower σ -masses, cf. Fig. 3(b). As repeatedly mentioned, the analysis of Ref. [28] (and its Fig. 1) (partly) stimulated our work—despite the fact that the nucleons and their chiral partners were actually neglected there.

The various other data points in Figs. 3(a) and 3(b) embed our results into a historical and broader research context, with the linear realization of chiral symmetry as the common footing. As stated in the Introduction, many approaches fail to simultaneously predict both a_0^0 and a_0^2 . The time-honored model calculations of Refs. [86, 87, 89] do not meet both experimental/ChPT values; using chiral (nucleon-)meson Lagrangians with a dynamic isoscalar σ -field, the data points “Basdevant, Lee (1970)” and “Geddes, Graham (1976)” match the isospin-two or isospin-zero scattering length, respectively, but they miss the other one. Together with the data point “Kramer (1969),” which is not accurate in either cases—in Fig. 3(b), it even lies outside of the plot range—, these publications document interest in the topic of pion-pion scattering in the framework of LSMs back in the 60’s and 70’s; they shed light on different chiral-symmetry breaking schemes and investigated many parameter settings in their chiral models. In more modern studies on LSMs, the scattering process remains a standard low-energy consistency check, as e.g. given by the data points “Aouissat *et al.* (1995),” “van Beveren *et al.* (2002),” and “Black *et al.* (2009)” [90, 93, 94]. While the former two determined the isospin-zero scattering length a_0^0 only (and the first of which solely agrees with the experimental uncertainty band by adding phenomenological form factors), the authors of the latter chose the mass M_σ “by hand” as 550 MeV (without any dedicated fitting procedure); with that choice, they were able to match both scattering lengths at the same time and underlined the crucial dependence of the result on the isoscalar σ -mass—again, this is contrary to the dynamic generation of model parameters of our approach.

As an example for addressing the inverse question, i.e., determining the σ -mass from pion-pion scattering data, the data point “Parganlija *et al.* (2010)” represents the outcome of the model fit of Ref. [26]. The point carries horizontal and vertical errorbars, where its actual value and the errorbars stand for the experimental input, the resulting mass M_σ , and the employed experimental uncertainty, respectively. The σ -mass has a rather broad range of $M_\sigma \sim 300$ MeV to 500 MeV, caused by the large vertical errorbars (among other numeric errors). The latest external data point, which is named “Lakaschus *et al.* (2018),” is an extension of Refs. [26–28] by light scalar tetraquark and glueball states. In combination with the heavy σ -resonance, however, the prediction of the scattering lengths (with vertical errorbars) is still not (simultaneously) compatible with the gray-shaded areas in Figs. 3(a) and 3(b).

Figure 4 demonstrates the (numeric) convergence of the expansion in Eqs. (42) to (51) within the LPA’, which we conceive as the most relevant approximation, as it incorporates the effective action Γ_k in its full-fledged ansatz (7). The curves for the scattering length a_0^0 in Fig. 4(a) overlap for $M_\sigma > 1$ GeV already for momentum orders of $m \geq 4$. They expose at the same time the necessity for higher orders ($m \gtrsim 8$) in the “sensitive” range around $M_\sigma \sim 500$ MeV. While the lowest order ($m = 0$) does not even match the WL (60) for a heavy σ -meson, the high-momentum orders ($m \geq 6$) converge fast to the exact value of Eq. (52) and the analytic and numeric errors of Eqs. (54) and (55) shrink [cf. Fig. 4(c)]. For a_0^2 the curves and the numeric values become identical as soon as $m \geq 4$ and the expansion errors completely vanish [cf. Figs. 4(b) and 4(d)], as stated in Sec. III. Like for a_0^0 , the first-order curve ($m = 0$) is incompatible with the WL (2). Its values are positive, thus lying outside of the actual axis borders of Fig. 4(b). The numeric evaluation of the low-energy expansion and the errors for the LPA’ are also given in Table IV. To restrain the errors to orders of 10^{-2} and 10^{-3} for the isospin-zero and isospin-two scattering lengths, respectively, one should consider the low-energy expansion up to $\mathcal{O}(p^4)$. This roughly yields equal uncertainties as for the experimental/ChPT values [16, 98] (for $I = 2$, the analytic and numeric errors are zero). At $\mathcal{O}(p^{12})$, the errors $\Delta_{\text{analytic/numeric}}^{0,12}$ are smaller than 10^{-4} , hence below the significant digits of the values in Table III. In leading order and next-to leading order of the low-energy expansion [$\mathcal{O}(p^0)$ and $\mathcal{O}(p^2)$], the results are unreliable, since the errors are of the same order as the S -wave scattering lengths themselves.¹³

¹³ These statements are concerned with truncation errors w.r.t. the generated higher-derivative pion self-interactions from the elimination of the isoscalar field; other error sources are still present.

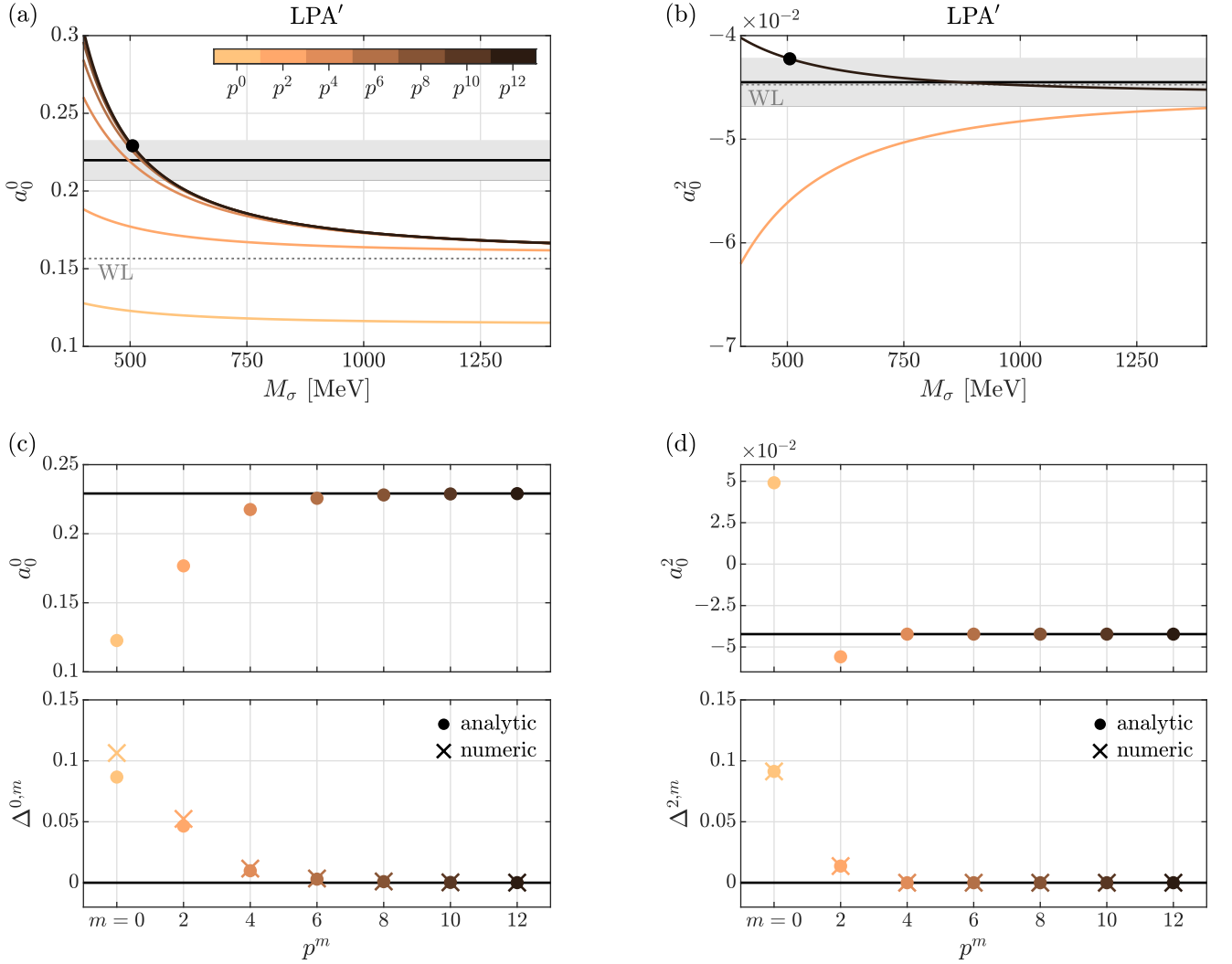


Figure 4. S -wave pion-pion scattering lengths within the LPA' and for different momentum orders in the low-energy expansion. The color bar in subfigure (a) indicates the approximation order w.r.t. the pion momentum p , in accordance with Eqs. (42) to (51). The black dots in subplots (a) and (b) as well as the black horizontal lines in panels (c) and (d) (upper plots) represent the exact values of Table III. (c) and (d) Convergence of the computed pairs (M_σ, a_0^I) , $I \in \{0, 2\}$, with successively advancing the p -order. The lower plots show the analytic and numeric errors $\Delta_{\text{analytic/numeric}}^{I,m}$, cf. Eqs. (54) through (56) and Table I. The analytic error is numerically evaluated for $\epsilon \simeq 0.0749$.

The integration of momentum modes gives direct access to the ϵ -parameter and to the ϖ -ratio over the entire energy-momentum range, $0 \text{ GeV} \leq k \leq 1.5 \text{ GeV}$. This is shown in Figs. 5(a) and 5(b); in those panels, the gray-shaded areas depict the regimes, where the low-energy parameters become large, i.e., $\epsilon \geq 1/4$ and $\varpi \geq 1$, and the low-energy ϵ -expansion (52) as well as analogous series in ϖ break down. This happens close to the crossover scale Λ_χ , where the bosons are (almost) degenerate in mass ($\epsilon \rightarrow 1$ for $k > \Lambda_\chi$) and the pion mass surpasses the characteristic scale of $4\pi f_\pi$ ($\varpi > 1$ for $k \gtrsim \Lambda_\chi$), cf. Eq. (63). In consequence, the scale evolution of the two parameters sets the “radius of convergence” of the low-energy expansion approximately to Λ_χ . Additionally, Fig. 5(a) and the inset in Fig. 5(b) confirm the (non-)monotonicity in the scaling of the σ -mass, as originally observed in Fig. 2. Most notably, this pushes the FRG curves “upwards” to the experimental band for a_0^0 and corrects them “downwards” for a_0^2 , see Fig. 5(c) and Fig. 5(d), respectively. The scale evolution is plotted for $0 \leq k < \Lambda_\chi$, the region beyond which the scattering lengths take on “unrealistically” large or small values [as also seen in the heat-kernel approach of Ref. [100] at finite temperature]. In the IR, the ϵ -parameters for the four different approximations are read off Fig. 5(a) as

$$\epsilon^{\text{LPA}'} \simeq 0.0749, \quad \epsilon^{\text{LPA}} \simeq 0.0792, \quad \epsilon^{\text{One-loop}} \simeq 0.0162, \quad \epsilon^{\text{MF}} \simeq 0.0090. \quad (67)$$

In all cases, they are smaller than ϵ_{phys} of Eq. (34), $\epsilon < \epsilon_{\text{phys}} \ll 1$, which justifies the expansion in powers of ϵ .

Table IV. Numeric evaluation of the errors $\Delta_{\text{analytic/numeric}}^{I,m}$ (upper part: analytic; lower part: numeric) for the LPA' ($\epsilon \simeq 0.0749$).

Isospin I	$\mathcal{O}(p^0)$	$\mathcal{O}(p^2)$	$\mathcal{O}(p^4)$	$\mathcal{O}(p^6)$	$\mathcal{O}(p^8)$	$\mathcal{O}(p^{10})$	$\mathcal{O}(p^{12})$
$I = 0$	0.0867	0.0465	9.8×10^{-3}	2.9×10^{-3}	8.8×10^{-3}	2.6×10^{-4}	7.9×10^{-5}
$I = 2$	0.0913	0.0137	zero	zero	zero	zero	zero
$I = 0$	0.1064	0.0524	0.0116	3.5×10^{-3}	1.1×10^{-3}	3.1×10^{-4}	9.3×10^{-5}
$I = 2$	0.0913	0.0137	zero	zero	zero	zero	zero

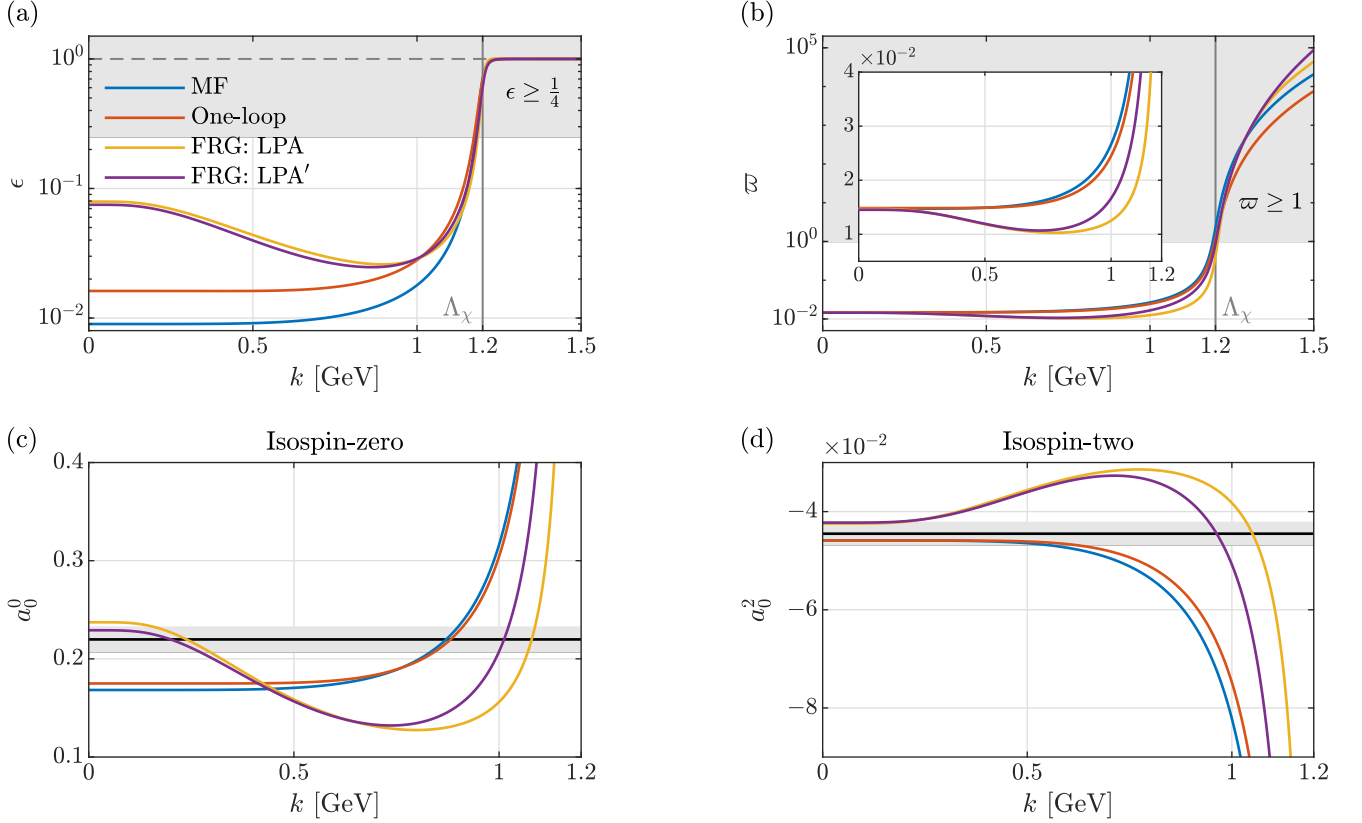


Figure 5. Flow of the low-energy parameters ϵ and ϖ and the S -wave scattering lengths as functions of the energy-momentum scale k . The legend in subfigure (a) is valid for all panels. (a) The parameter ϵ approaches the value of one, $\epsilon \rightarrow 1$ (horizontal dashed line), for large k . In the gray-shaded area at $\epsilon \geq 1/4$, the low-energy expansion (52) necessarily fails. (b) The parameter ϖ drastically grows in the vicinity of the chiral-symmetry breaking scale Λ_χ . It further signals for $\varpi \geq 1$ the breakdown of the low-energy description (purely) in terms of pion fields. (c) and (d) Isospin-zero and isospin-two scattering lengths a_0^0 and a_0^2 and their dependence on the energy-momentum scale $k < \Lambda_\chi = 1.2$ GeV. As before, the experimental/ChPT results are given as black horizontal lines on a gray background (errors).

V. SUMMARY AND CONCLUSION

We have investigated the dynamic generation of the S -wave pion-pion scattering lengths within a nucleon-meson model featuring parity doubling. To this end, the powerful framework of the FRG has been combined with a systematic expansion of the bosonic part of the quantum effective action in terms of stereographic coordinates and pion momenta, underlining similarities to the NLSM and the chiral expansion of ChPT. The FRG technique allowed us to produce fluctuation-enhanced results, which were compared to MF and one-loop calculations. In particular, this ansatz enabled us to

- bring together significant low-energy scales and parameters in the dynamic context of the renormalization-group idea; we deliberately chose as the initialization scale for the integration of momentum modes the characteristic scale of chiral symmetry breaking, $\Lambda_\chi \simeq 4\pi f_\pi$.

- get access to the effective action of the nucleon-meson model and compute the pion-pion scattering amplitude via tree diagrams consisting of dressed propagators and vertices.
- organize the pionic effective action in a power-counting scheme in terms of pion fields and pion momenta (similar to the NLSM and ChPT).
- discuss a “radius of convergence” for the low-energy expansion (w.r.t. the running energy-momentum scale of the FRG).
- learn about subtleties and intricacies coming with the low-energy expansion of the nonlinear pionic effective action and the truncation of its higher-derivative interactions.

As the major finding, we were able to simultaneously match (within errorbars) the experimental/ChPT values for the S -wave isospin-zero and isospin-two scattering lengths a_0^0 and a_0^2 . This was accomplished for the LPA'-truncation within the FRG (and not quite for the LPA) with the precondition of chiral symmetry breaking occurring at $\Lambda_\chi = 1.2 \text{ GeV} \simeq 4\pi f_\pi$,

$$\begin{aligned}
\text{LPA:} \quad a_0^0 &= 0.2373, & a_0^2 &= -0.0425; \\
\text{LPA':} \quad a_0^0 &= 0.2291, & a_0^2 &= -0.0422; \\
\text{experiment/ChPT:} \quad a_0^0 &= 0.2198 \pm 0.0126, & a_0^2 &= -0.0445 \pm 0.0023.
\end{aligned} \tag{68}$$

The integration of momentum modes was moreover constrained by the physical masses and the pion decay constant f_π in the IR limit, where solely the dynamically generated isoscalar mass M_σ was understood as a model prediction. The value of M_σ is crucial for a “successful” computation of the isospin-zero scattering length a_0^0 in the linear realization of chiral symmetry [28, 94]. In the LPA and LPA', we obtained M_σ of the order of 500 MeV. Contrary to the present work, similar phenomenological approaches oftentimes fail in simultaneously reproducing both scattering lengths or require for this purpose additional form factors and the value of M_σ , as well-chosen external input [26–29, 86–91, 94]. The FRG framework outperforms numerous other calculations in that sense and gave new insights into the energy-momentum dependence of the pion-pion scattering lengths. To generate the desired values for the scattering lengths, the chiral-invariant mass of the nucleon and its chiral partner roughly lay in the range of $450 \text{ MeV} \lesssim M_0 \lesssim 825 \text{ MeV}$ for the LPA' (824.5 MeV in the IR) and it was fixed to 824.5 MeV for the LPA. These masses are broadly consistent with the corresponding parameters in Refs. [56, 59, 68, 69]. The mass parameter m_0 and the influence of its variation on the FRG flows will be discussed in detail in a follow-up work.

In the simplest approximations (MF and one-loop), we did not reach agreement for a_0^0 , which is mainly due to the relatively large value of M_σ obtained in these calculations, $M_\sigma > 1 \text{ GeV}$. However, such a value turns out to be necessary to meet the above constraints for the chiral-symmetry breaking scale and the physical masses in the IR. Interestingly, large σ -masses of more than 1 GeV were also favored by the (extended) LSMs of Refs. [26, 27], which were fitted to experimental data like mesonic decay constants and decay widths. On these grounds, the computation of the pion-pion scattering lengths in Ref. [28] further motivated the current publication, since its findings were not compatible with the experimental values. Suitable to the discussion of the σ -mass, recent extensions of these models with tetraquarks and glueballs as additional “exotic” resonances in the light scalar sector below 1.3 GeV improve the scattering lengths, but still not to a satisfactory conclusion (regarding the experimental/ChPT values) [29].

In addition to the scattering lengths, we supplied a comprehensive investigation of the scale evolution of important low-energy parameters, which determines the “radius of convergence” of the expansion in small pion momenta (w.r.t. the energy-momentum scale). Close to $\Lambda_\chi \simeq 4\pi f_\pi$, those parameters become large and signal the breakdown of the corresponding geometric series. There, the predictability of the pion-pion scattering lengths within the presented formalism (with “stereographic pions”) and its convergence is lost. To compute the scattering lengths in the convergent regime up to a numerical error of less than 10^{-4} (as compared to the universal LSM formulas), we were urged to take pion self-interactions of $\mathcal{O}(p^{12})$ in the pion momentum p into account. In general, our choice of the low-energy parameter $\epsilon = M_\pi^2/M_\sigma^2$ for this expansion is not unique and might be replaced by other appropriate choices. The analysis of the low-energy parameters was finally accompanied by an explicit proof of coordinate independence of the (on-shell) four-point function. In summary, we have thereby drawn—with the FRG formalism applied to a nucleon-meson model and in an unprecedented manner—a direct connection between the scale of $4\pi f_\pi \simeq 1.2 \text{ GeV}$ and the S -wave pion-pion scattering lengths as low-energy observables of QCD.

Nonetheless, in the current approximation, it is not possible to yield analogous corrections beyond the leading-order NLSM in the nonlinear realization of chiral symmetry, which inevitably demands the elimination of the σ -mode (or the “radial excitation”) through the limit $M_\sigma \rightarrow \infty$ [10, 30, 32]. Going beyond the leading order requires the explicit treatment of higher-derivative interactions in the (parity-doublet) nucleon-meson model, as done in Refs. [37, 38, 42] for the quark-meson(-diquark) models. These terms generate low-energy couplings independent of the isoscalar mass

M_σ and will be addressed in upcoming publications. In addition, future efforts could focus on the scattering process at nonzero temperatures and densities (or external fields) [100, 101], also involving latest fluid-dynamical perspectives on the nonperturbative FRG flows [102]. It would be eventually interesting to analyze the (tree-level) effect of vector mesons on the pion-pion scattering lengths (in the light of resonance saturation) [28, 103].

Finally, based on the presented calculations of the S -wave pion-pion scattering lengths, we do not draw conclusions in favor of or against specific features of parity doubling in the investigated nucleon-meson model. We regard the present investigation as an interesting application of the parity-doublet model, in which we could combine pertinent observables, parameters, and scales of low-energy QCD. In general, our findings do not rule out other model settings, especially concerning the debate about the chiral-invariant nucleon mass in the chiral-restored phase.

ACKNOWLEDGMENTS

We are grateful to F. Divotgey for contributing to the early stages of this work. J.E. is indebted to J.M. Pawłowski, D.H. Rischke, B.J. Schaefer and L. von Smekal for their longstanding support. The authors further thank F. Giacosa and A. Koenigstein for valuable discussions. J.E. acknowledges funding by the German National Academy of Sciences Leopoldina (through the scholarship 2020-06). J.E. thanks the IPhT for its hospitality.

Appendix A: Model construction and physical basis

The parity-doublet nucleon-meson model (7) incorporates baryons in the “mirror assignment” of chiral symmetry. They “live” in the three-fold tensor product of the Dirac-fermion representation $(2, 1) \oplus (1, 2)$ (w.r.t. Lorentz symmetry),

$$[(2, 1) \oplus (1, 2)]^{\otimes 3} \cong 5 [(2, 1) \oplus (1, 2)] + 3 [(3, 2) \oplus (2, 3)] + (4, 1) \oplus (1, 4). \quad (\text{A1})$$

Each of the direct sums on the left-hand side of the above equation symbolizes a quark representation. To obtain this result, we made use of the decomposition

$$[(2, 1) \oplus (1, 2)]^{\otimes 2} \cong 2(1, 1) \oplus 2(2, 2) \oplus (3, 1) \oplus (1, 3). \quad (\text{A2})$$

More precisely, the baryons correspond to one of the Dirac representations on the right-hand side of Eq. (A1). In the mirror assignment of the two fermion fields ψ_1 and ψ_2 , however, the Weyl spinors are considered as twisted, i.e.,

$$\begin{aligned} \psi_1: (2, 1) \oplus (1, 2) &= \psi_{1,l} \oplus \psi_{1,r}, \\ \psi_2: (1, 2) \oplus (2, 1) &= \psi_{2,l} \oplus \psi_{2,r}. \end{aligned} \quad (\text{A3})$$

The transformation behavior of the “left” and “right” components thus reads

$$\begin{aligned} \psi_{1,l} &\longrightarrow u_l \psi_{1,l}, & \psi_{1,r} &\longrightarrow u_r \psi_{1,r}, \\ \psi_{2,l} &\longrightarrow u_r \psi_{2,l}, & \psi_{2,r} &\longrightarrow u_l \psi_{2,r}, \end{aligned} \quad (u_l, u_r) \in \text{SU}(2) \times \text{SU}(2). \quad (\text{A4})$$

Further details about the mirror assignment and a comparison to the “naive” assignment—where both fields behave equally under chiral transformations—can be found in Refs. [56–59].¹⁴ Equipped with this setting, it is then straightforward to construct invariant interaction terms with mesons [in the $(2, 2)$ -representation of the chiral group] in the “usual manner” [104] as well as a chiral-invariant mass term,

$$m_0 (\bar{\psi}_{1,l} \psi_{2,r} + \bar{\psi}_{2,l} \psi_{1,r}) \equiv m_0 (\bar{\psi}_1 \psi_2 + \bar{\psi}_2 \psi_1). \quad (\text{A5})$$

The last identity is inferred from the idempotence of chiral projection operators (not shown here). Eventually, these considerations result in the truncation (7), where the opposite minus sign in front of the term $y_2 \bar{\psi}_2 \sigma \psi_2$ is the consequence of chiral invariance in the mirror assignment.

The fermions ψ_1 and ψ_2 are initially defined with even parity, $P = 1$. For them to describe the nucleons and their chiral-partner fields, it is necessary to diagonalize the mass matrix (9) and switch the parity eigenvalue of one of the

¹⁴ Especially, a very thorough introduction is given in Ref. [59].

spinors. This is achieved by the orthogonal transformation given by

$$N = \begin{pmatrix} N_+ \\ N_- \end{pmatrix} = \begin{pmatrix} \mathbb{1} & 0 \\ 0 & \gamma_5 \end{pmatrix} \begin{pmatrix} \cos \omega & \sin \omega \\ -\sin \omega & \cos \omega \end{pmatrix} \begin{pmatrix} \psi_1 \\ \psi_2 \end{pmatrix} =: \mathcal{P}O\Psi = \mathcal{P}\Psi', \quad (\text{A6})$$

$$\bar{N} = (\bar{N}_+, \bar{N}_-) = \bar{\Psi}O^\top \mathcal{P} \begin{pmatrix} 1 & 0 \\ 0 & -1 \end{pmatrix}, \quad (\text{A7})$$

such that $N_+ = \psi'_1$ and $N_- = \gamma_5 \psi'_2$. The matrix \mathcal{P} obviously attaches an additional Dirac matrix γ_5 to the rotated fermion ψ'_2 , turning its parity to $\mathbf{P} = -1$ [59]. In Eq. (A7), we exploited the fact that $\mathcal{P}^2 = \mathbb{1}$. For the rotation angle ω , one finds

$$\omega = \frac{1}{2} \arctan \left[\frac{2m_0}{(y_1 + y_2)\sigma_0} \right] \equiv \frac{1}{2} \arctan \left[\frac{2M_0}{(\tilde{y}_1 + \tilde{y}_2)\tilde{\sigma}_0} \right]. \quad (\text{A8})$$

This expression is renormalization-group invariant, cf. the discussion around Eq. (15) in Sec. II. The angle ω finally converts the mass matrix (9) to the equivalent (10). Its scale evolution is shown in Fig. 9(a) in Appendix D. In particular, $\omega \rightarrow \pi/4$ in the UV when N_+ and N_- are degenerate in mass.

Appendix B: Geometry and algebra

A schematic picture of stereographic projections (from the south pole) is shown in Fig. 6. The north pole $\tilde{\varphi} = (0, 0, 0, \theta)$ is mapped onto the origin of \mathbb{R}^3 , $\mathfrak{D} = (0, 0, 0)$ (indicated as a red dot). A local dreibein on the sphere \mathbb{S}^3 is constructed from the Maurer-Cartan form $\alpha_\mu(\Pi)$,

$$\alpha_\mu(\Pi) = \Sigma^{-1}(\Pi) \partial_\mu \Sigma(\Pi), \quad (\text{B1})$$

where $\Sigma(\Pi)$ is a coset representative of the coset space $\text{SO}(4)/\text{SO}(3) \cong \mathbb{S}^3$. The component $\alpha_\mu(\Pi)$ takes on values in the (six-dimensional) Lie algebra $\mathfrak{so}(4)$, therefore decomposing as

$$\alpha_\mu(\Pi) = ie_\mu^a(\Pi)c_a + iw_\mu^i(\Pi)s_i, \quad a, i = 1, 2, 3. \quad (\text{B2})$$

The vectors c_a , $a = 1, 2, 3$, and s_i , $i = 1, 2, 3$, are the coset generators and those of the (residual) isospin subalgebra $\mathfrak{so}(3)$, respectively. The coefficients e_μ^a can be expanded in terms of the local coordinates $\Pi^{\bar{a}}$,¹⁵

$$e_\mu^a(\Pi) = e_a^a(\Pi) \partial_\mu \Pi^{\bar{a}} = \frac{4f_\pi}{4f_\pi^2 + \Pi^2} \delta_a^{\bar{a}} \partial_\mu \Pi^{\bar{a}}, \quad \bar{a} = 1, 2, 3. \quad (\text{B3})$$

The objects $e_a^{\bar{a}}$ form the requested local frame (dreibein) on \mathbb{S}^3 with the related metric tensor

$$g_{\bar{a}\bar{b}}(\Pi) = \delta_{ab} e_a^{\bar{a}}(\Pi) e_b^{\bar{b}}(\Pi) = \frac{16f_\pi^2}{(4f_\pi^2 + \Pi^2)^2} \delta_{\bar{a}\bar{b}}. \quad (\text{B4})$$

The generators s_i , $i = 1, 2, 3$, of the Lie algebra $\mathfrak{so}(3)$ and their algebraic complement c_a , $a = 1, 2, 3$, which together form those of the Lie algebra $\mathfrak{so}(4)$, are chosen as

$$\begin{aligned} s_1 &= \begin{pmatrix} 0 & 0 & 0 & 0 \\ 0 & 0 & -i & 0 \\ 0 & i & 0 & 0 \\ 0 & 0 & 0 & 0 \end{pmatrix}, & s_2 &= \begin{pmatrix} 0 & 0 & i & 0 \\ 0 & 0 & 0 & 0 \\ -i & 0 & 0 & 0 \\ 0 & 0 & 0 & 0 \end{pmatrix}, & s_3 &= \begin{pmatrix} 0 & -i & 0 & 0 \\ i & 0 & 0 & 0 \\ 0 & 0 & 0 & 0 \\ 0 & 0 & 0 & 0 \end{pmatrix}, \\ c_1 &= \begin{pmatrix} 0 & 0 & 0 & -i \\ 0 & 0 & 0 & 0 \\ 0 & 0 & 0 & 0 \\ i & 0 & 0 & 0 \end{pmatrix}, & c_2 &= \begin{pmatrix} 0 & 0 & 0 & 0 \\ 0 & 0 & 0 & -i \\ 0 & 0 & 0 & 0 \\ 0 & i & 0 & 0 \end{pmatrix}, & c_3 &= \begin{pmatrix} 0 & 0 & 0 & 0 \\ 0 & 0 & 0 & 0 \\ 0 & 0 & 0 & -i \\ 0 & 0 & i & 0 \end{pmatrix}. \end{aligned} \quad (\text{B5})$$

¹⁵ The coefficients w_μ^i parametrize isospin transformations; they are of no relevance for the purely pionic model of our work.

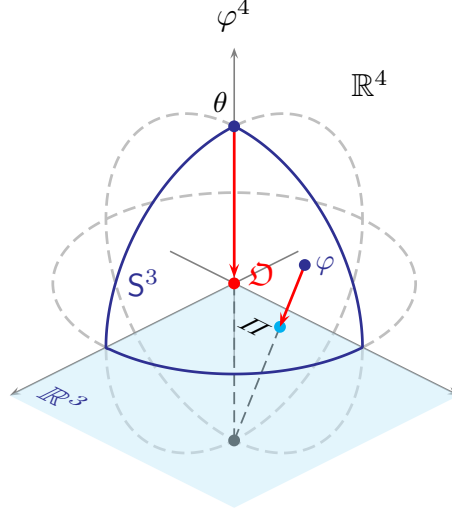


Figure 6. Vacuum manifold of the nucleon-meson model. Schematic three-dimensional sketch of stereographic projections from the south pole (red arrows) of the three-sphere S^3 onto \mathbb{R}^3 . The contours of the sphere S^3 are depicted by blue solid (“octant” directed at the viewer) and gray dashed lines.

They fulfill the commutator (Lie-bracket) and trace relations

$$\begin{aligned}
 [s_i, s_j] &= i\epsilon_{ij}{}^k s_k, & \text{tr}(s_i s_j) &= 2\delta_{ij}, \\
 [s_i, c_a] &= i\epsilon_{ia}{}^b c_b, & \text{tr}(s_i c_a) &= 0, \\
 [c_a, c_b] &= i\epsilon_{ab}{}^i s_i, & \text{tr}(c_a c_b) &= 2\delta_{ab},
 \end{aligned} \tag{B6}$$

with the Levi-Civita symbols $\epsilon_{ij}{}^k$ as the structure constants. An appropriate coset representative $\Sigma(\Pi)$, i.e., an $\text{SO}(4)$ -matrix parametrized through the stereographic pions Π , and the corresponding skew-symmetric Maurer-Cartan form $\alpha_\mu(\Pi)$ on the vacuum manifold S^3 are given by

$$\Sigma(\Pi) = \begin{pmatrix} \mathbb{1} - \frac{2\Pi\Pi^\top}{4f_\pi^2 + \Pi^2} & \frac{4f_\pi\Pi}{4f_\pi^2 + \Pi^2} \\ -\frac{4f_\pi\Pi^\top}{4f_\pi^2 + \Pi^2} & \frac{4f_\pi^2 - \Pi^2}{4f_\pi^2 + \Pi^2} \end{pmatrix} \in \text{SO}(4), \quad \Pi = (\Pi^1, \Pi^2, \Pi^3)^\top, \tag{B7}$$

$$\alpha_\mu(\Pi) = \Sigma^{-1}(\Pi)\partial_\mu\Sigma(\Pi) = \begin{pmatrix} \frac{2[\Pi\partial_\mu\Pi^\top - (\partial_\mu\Pi)\Pi^\top]}{4f_\pi^2 + \Pi^2} & \frac{4f_\pi\partial_\mu\Pi}{4f_\pi^2 + \Pi^2} \\ -\frac{4f_\pi\partial_\mu\Pi^\top}{4f_\pi^2 + \Pi^2} & 0 \end{pmatrix} \in \mathfrak{so}(4). \tag{B8}$$

The coefficients $e_\mu^\alpha(\Pi)$ are extracted from Eq. (B8) via

$$e_\mu^\alpha(\Pi) = -\frac{i}{2} \text{tr}[\alpha_\mu(\Pi)c_\alpha] = \frac{4f_\pi\partial_\mu\Pi^\alpha}{4f_\pi^2 + \Pi^2}, \tag{B9}$$

which was used in Eq. (B3). The transformation properties of these geometric objects are extensively examined in Refs. [38, 40, 41] (which also contain a lot more details about the geometric interpretation and the nonlinear transformation behavior of the “stereographic pions”).

Appendix C: Coordinate independence of the on-shell four-point function

Consider the change of variable $\varphi \rightarrow \varphi'$ in the effective-action functional $\Gamma[\varphi]$. We assume that the transformation function $\varphi = \varphi[\varphi']$ is smooth and invertible, i.e., it is differentiable and its inverse φ^{-1} exists. The transformed action functional is $\Gamma'[\varphi'] = \Gamma[\varphi[\varphi']]$. Specifically, we regard the Cartesian coordinates φ as (invertible) mappings of the

stereographic projections φ' [cf. Eq. (18)].¹⁶ Taking a solution φ_{sol} of the EOM,

$$\left. \frac{\delta \Gamma}{\delta \varphi^i} \right|_{\varphi_{\text{sol}}} = 0, \quad i = 1, \dots, 4, \quad (\text{C1})$$

the functional derivative of Γ' evaluated at $\varphi^{-1}[\varphi_{\text{sol}}]$ also vanishes by the chain rule,

$$\left. \frac{\delta \Gamma'[\varphi']}{\delta \varphi'^j(x)} \right|_{\varphi^{-1}[\varphi_{\text{sol}}]} = \int_z \left. \frac{\delta \Gamma[\varphi]}{\delta \varphi^i(z)} \right|_{\varphi_{\text{sol}}} \left. \frac{\delta \varphi^i(z)}{\delta \varphi'^j(x)} \right|_{\varphi^{-1}[\varphi_{\text{sol}}]} = 0, \quad j = 1, \dots, 4. \quad (\text{C2})$$

This equation shows that $\varphi^{-1}[\varphi_{\text{sol}}]$ is a solution to the EOM w.r.t. φ' . The map φ^{-1} is well-defined in our case, since we restrict the discussion to the vicinity of the origin \mathfrak{D} of \mathbb{R}^3 ; see once more Fig. 6. Consequently, we directly obtain the solution $\varphi'_{\text{sol}} = \varphi^{-1}[\varphi_{\text{sol}}]$ once φ_{sol} is known, and vice versa.

Solving the EOM w.r.t. the radial θ -field implicitly defines the function $\theta_{\text{sol}}[\Pi]$,

$$\left. \frac{\delta \Gamma'}{\delta \theta} \right|_{\theta_{\text{sol}}[\Pi]} = 0. \quad (\text{C3})$$

The second functional derivative of Eq. (C3),

$$\frac{\delta^2}{\delta \Pi^a(x_1) \delta \Pi^b(x_2)} \left(\left. \frac{\delta \Gamma'[\varphi']}{\delta \theta(x_3)} \right|_{\theta_{\text{sol}}} \right) = \Gamma'_{\Pi\Pi\theta}{}^{(3)ab}(x_1, x_2, x_3) + \int_z \Gamma'_{\theta\theta}{}^{(2)}(z, x_3) \frac{\delta^2 \theta_{\text{sol}}(z)}{\delta \Pi^a(x_1) \delta \Pi^b(x_2)} = 0, \quad (\text{C4})$$

yields the important relation

$$\frac{\delta^2 \theta_{\text{sol}}(x_1)}{\delta \Pi^a(x_2) \delta \Pi^b(x_3)} = - \int_z \frac{\delta^2 W'[J']}{\delta J'_\theta(x_1) \delta J'_\theta(z)} \Gamma'_{\Pi\Pi\theta}{}^{(3)ab}(x_2, x_3, z) \equiv - \int_z W'_{\theta\theta}{}^{(2)}(x_1, z) \Gamma'_{\Pi\Pi\theta}{}^{(3)ab}(x_2, x_3, z). \quad (\text{C5})$$

To derive the above Eq. (C5), we used the fact that the first derivative of $\theta_{\text{sol}}[\Pi]$ is zero (due to the necessary isospin symmetry of the solution) as well as the well-known identity

$$\int_z \frac{\delta^2 W'[J']}{\delta J'^i(x_1) \delta J'^k(z)} \frac{\delta^2 \Gamma'[\varphi']}{\delta \varphi'^k(z) \delta \varphi'^j(x_2)} = \delta^{ij} \delta(x_1 - x_2). \quad (\text{C6})$$

The functional $W'[J']$ (with the sources J') is the Schwinger functional, i.e., the Legendre transform of $\Gamma'[\varphi']$. Defining the generating functional Γ'_{sol} ,

$$\Gamma'_{\text{sol}}[\Pi] := \Gamma'[\varphi']|_{\theta = \theta_{\text{sol}}}, \quad (\text{C7})$$

one obtains the four-point function of Γ'_{sol} as

$$\begin{aligned} \Gamma'_{\text{sol}}{}^{(4)abcd}{}_{\Pi\Pi\Pi\Pi}(x_1, x_2, x_3, x_4) &= \Gamma'_{\Pi\Pi\Pi\Pi}{}^{(4)abcd}(x_1, x_2, x_3, x_4) - \int_{z_1} \int_{z_2} \Gamma'_{\Pi\Pi\theta}{}^{(3)ab}(x_1, x_2, z_1) W'_{\theta\theta}{}^{(2)}(z_1, z_2) \Gamma'_{\Pi\Pi\theta}{}^{(3)cd}(x_3, x_4, z_2) \\ &\quad - \int_{z_1} \int_{z_2} \Gamma'_{\Pi\Pi\theta}{}^{(3)ac}(x_1, x_3, z_1) W'_{\theta\theta}{}^{(2)}(z_1, z_2) \Gamma'_{\Pi\Pi\theta}{}^{(3)bd}(x_2, x_4, z_2) \\ &\quad - \int_{z_1} \int_{z_2} \Gamma'_{\Pi\Pi\theta}{}^{(3)ad}(x_1, x_4, z_1) W'_{\theta\theta}{}^{(2)}(z_1, z_2) \Gamma'_{\Pi\Pi\theta}{}^{(3)bc}(x_2, x_3, z_2), \end{aligned} \quad (\text{C8})$$

where we again utilized that odd derivatives of θ_{sol} vanish. In the language of Feynman diagrams, Eq. (C8) translates into the right-hand sides of Eqs. (31) and (32), with the θ -propagator

$$G'_{\theta\theta}(x_1, x_2) = i W'_{\theta\theta}{}^{(2)}(x_1, x_2) \equiv \frac{i \delta^2 W'[J']}{\delta J'_\theta(x_1) \delta J'_\theta(x_2)}. \quad (\text{C9})$$

¹⁶ We do not print the prime in the main part.

To demonstrate the coordinate independence of the on-shell four-point function, we now express Eq. (C8) in terms of the original vertex functions (derivatives of Γ): As prerequisites, we therefore explicitly calculate the derivatives of the coordinate function $\varphi[\varphi']$,

$$\frac{\delta\varphi^i(x_1)}{\delta\Pi^a(x_2)} = \frac{\theta}{f_\pi} \delta^{ia} \delta(x_1 - x_2), \quad (\text{C10})$$

$$\frac{\delta\varphi^i(x_1)}{\delta\theta(x_2)} = \delta^{i4} \delta(x_1 - x_2), \quad (\text{C11})$$

$$\frac{\delta^2\varphi^i(x_1)}{\delta\Pi^a(x_2)\delta\Pi^b(x_3)} = -\frac{\theta}{f_\pi^2} \delta^{i4} \delta^{ab} \delta(x_1 - x_2) \delta(x_1 - x_3), \quad (\text{C12})$$

$$\frac{\delta^2\varphi^i(x_1)}{\delta\Pi^a(x_2)\delta\theta(x_3)} = \frac{1}{f_\pi} \delta^{ia} \delta(x_1 - x_2) \delta(x_1 - x_3), \quad (\text{C13})$$

$$\frac{\delta^2\varphi^i(x_1)}{\delta\Pi^a(x_2)\delta\Pi^b(x_3)\delta\Pi^c(x_4)} = -\frac{\theta}{2f_\pi^2} (\delta^{ia} \delta^{bc} + \delta^{ib} \delta^{ac} + \delta^{ic} \delta^{ab}) \delta(x_1 - x_2) \delta(x_1 - x_3) \delta(x_1 - x_4), \quad (\text{C14})$$

and provide the chiral Ward identity between the two-point and the three-point functions based on the (renormalized) bosonic part of the Minkowskian analogue of Eq. (7),

$$\frac{\delta^2\Gamma[\varphi]}{\delta\varphi^i(x_1)\delta\varphi^j(x_2)} = - [(\square_{x_1} + 2V') \delta^{ij} + 4V'' \varphi^i(x_1)\varphi^j(x_1)] \delta(x_1 - x_2), \quad (\text{C15})$$

$$\begin{aligned} \frac{\delta^3\Gamma[\varphi]}{\delta\varphi^i(x_1)\delta\varphi^j(x_2)\delta\varphi^k(x_3)} = & -4 \left\{ V'' [\varphi^i(x_1)\delta^{jk} + \varphi^j(x_1)\delta^{ik} + \varphi^k(x_1)\delta^{ij}] \right. \\ & \left. + 2V^{(3)} \varphi^i(x_1)\varphi^j(x_1)\varphi^k(x_1) \right\} \delta(x_1 - x_2) \delta(x_1 - x_3), \end{aligned} \quad (\text{C16})$$

$$\Rightarrow \quad \Gamma_{\pi\pi\sigma}^{(3)ab}(x_1, x_2, x_3) = \frac{1}{\theta} [\Gamma_{\sigma\sigma}^{(2)}(x_1, x_3) \delta^{ab} - \Gamma_{\pi\pi}^{(2)ab}(x_1, x_3)] \delta(x_1 - x_2), \quad (\text{C17})$$

where $V' \equiv dV(\varphi^2)/d\varphi^2$, $V'' \equiv d^2V(\varphi^2)/(d\varphi^2)^2$, and so forth (to be distinguished from the above prime indicating the transformed effective action). By virtue of the chain rule and the EOM from the beginning of this Appendix, the three-point and four-point functions on the right of Eq. (C8) are rewritten as

$$\begin{aligned} \Gamma_{\Pi\Pi\theta}^{(3)ab}(x_1, x_2, x_3) = & \int_{z_1} \int_{z_2} \frac{\delta^2\Gamma[\varphi]}{\delta\varphi^i(z_1)\delta\varphi^j(z_2)} \left[\frac{\delta\varphi^i(z_1)}{\delta\Pi^a(x_1)} \frac{\delta^2\varphi^j(z_2)}{\delta\Pi^b(x_2)\delta\theta(x_3)} + \frac{\delta\varphi^i(z_1)}{\delta\Pi^b(x_2)} \frac{\delta^2\varphi^j(z_2)}{\delta\Pi^a(x_1)\delta\theta(x_3)} \right. \\ & \left. + \frac{\delta^2\varphi^i(z_1)}{\delta\Pi^a(x_1)\delta\Pi^b(x_2)} \frac{\delta\varphi^j(z_2)}{\delta\theta(x_3)} \right] \\ & + \int_{z_1} \int_{z_2} \int_{z_3} \frac{\delta^3\Gamma[\varphi]}{\delta\varphi^i(z_1)\delta\varphi^j(z_2)\delta\varphi^l(z_3)} \frac{\delta\varphi^i(z_1)}{\delta\Pi^a(x_1)} \frac{\delta\varphi^j(z_2)}{\delta\Pi^b(x_2)} \frac{\delta\varphi^l(z_3)}{\delta\theta(x_3)} \\ = & \frac{\theta}{f_\pi^2} \left\{ \theta \Gamma_{\pi\pi\sigma}^{(3)ab}(x_1, x_2, x_3) + \Gamma_{\pi\pi}^{(2)ab}(x_1, x_2) [\delta(x_1 - x_3) + \delta(x_2 - x_3)] \right. \\ & \left. - \Gamma_{\sigma\sigma}^{(2)}(x_1, x_3) \delta^{ab} \delta(x_1 - x_2) \right\}, \end{aligned} \quad (\text{C18})$$

$$\begin{aligned} \Gamma_{\Pi\Pi\Pi\Pi}^{(4)abcd}(x_1, x_2, x_3, x_4) = & \frac{\theta^2}{f_\pi^4} \left\{ \theta^2 \Gamma_{\pi\pi\pi\pi}^{(4)abcd}(x_1, x_2, x_3, x_4) - \delta^{ab} \delta^{cd} \left[\Gamma_{\sigma\sigma}^{(2)}(x_1, x_2) \delta(x_2 - x_3) \delta(x_3 - x_4) \right. \right. \\ & \left. \left. + \Gamma_{\sigma\sigma}^{(2)}(x_3, x_4) \delta(x_1 - x_2) \delta(x_1 - x_4) - \Gamma_{\sigma\sigma}^{(2)}(x_1, x_3) \delta(x_1 - x_2) \delta(x_3 - x_4) \right] \right. \\ & \left. + \frac{1}{2} \Gamma_{\pi\pi}^{(2)ab}(x_1, x_2) \delta^{cd} [\delta(x_2 - x_3) \delta(x_2 - x_4) - \delta(x_1 - x_3) \delta(x_1 - x_4)] \right. \\ & \left. + \frac{1}{2} \Gamma_{\pi\pi}^{(2)cd}(x_3, x_4) \delta^{ab} [\delta(x_1 - x_4) \delta(x_2 - x_4) - \delta(x_1 - x_3) \delta(x_2 - x_3)] \right. \\ & \left. + \text{crossings to the previous three terms} \right\}. \end{aligned} \quad (\text{C19})$$

Plugging in these relations in Eq. (C8), taking advantage of the Ward identity (C17), and transferring everything into momentum space along the conventions visible in Fig. 1,

$$\begin{aligned} \Rightarrow \int_{x_1} \int_{x_2} \int_{x_3} \int_{x_4} \exp\left(i \sum_{n=1}^4 x_n \cdot p_n\right) i\Gamma_{\text{sol}}^{\prime(4)abcd}(x_1, x_2, x_3, x_4) \\ \equiv (2\pi)^4 \delta\left(\sum_{n=1}^4 x_n \cdot p_n\right) i\Gamma_{\text{sol}}^{\prime(4)abcd}(p_1, p_2, p_3, p_4), \end{aligned} \quad (\text{C20})$$

$$\delta(x_1 - x_2) = \int \frac{d^4q}{(2\pi)^4} e^{-iq \cdot (x_1 - x_2)} \equiv \int_q e^{-iq \cdot (x_1 - x_2)}, \quad (\text{C21})$$

$$\Gamma_{\pi\pi}^{(2)ab}(x_1, x_2) = \int_q (q^2 - M_\pi^2) \delta^{ab} e^{-iq \cdot (x_1 - x_2)}, \quad W_{\sigma\sigma}^{(2)}(x_1, x_2) = \int_q \frac{1}{q^2 - M_\sigma^2} e^{-iq \cdot (x_1 - x_2)}, \quad (\text{C22})$$

we find for the amplitude $\mathfrak{A}(s, t, u)$ in Eq. (27) the expression

$$\mathfrak{A}(s, t, u) = \frac{1}{f_\pi^2} \left\{ (M_\pi^2 - M_\sigma^2) \frac{s - M_\pi^2}{s - M_\sigma^2} - \left[\left(\frac{1}{2} - \frac{s - M_\pi^2}{s - M_\sigma^2} \right) \sum_{i=1}^4 \mathbb{P}_i + \frac{\mathbb{P}_1\mathbb{P}_3 + \mathbb{P}_1\mathbb{P}_4 + \mathbb{P}_2\mathbb{P}_3 + \mathbb{P}_2\mathbb{P}_4}{s - M_\sigma^2} \right] \right\}, \quad (\text{C23})$$

with $\mathbb{P}_n := p_n^2 - M_\pi^2$, $n = 1, \dots, 4$. The momentum-space Feynman rules, needed for the last step, read for the relevant s -channel contributions:

$$\Rightarrow -4iV'' \delta^{ab} \delta^{cd} \equiv i \frac{M_\pi^2 - M_\sigma^2}{f_\pi^2} \delta^{ab} \delta^{cd}, \quad (\text{C24})$$

$$\Rightarrow (-4iV'')^2 f_\pi^2 \frac{i}{s - M_\sigma^2} \delta^{ab} \delta^{cd} \equiv -\frac{(M_\pi^2 - M_\sigma^2)^2}{f_\pi^2} \frac{i}{s - M_\sigma^2} \delta^{ab} \delta^{cd}, \quad (\text{C25})$$

where we used the chiral Ward identity (C17). On the mass shell, $\mathbb{P}_n = 0 \forall n$, the result simplifies to

$$\mathfrak{A}(s, t, u) = \frac{M_\pi^2 - M_\sigma^2}{f_\pi^2} \frac{s - M_\pi^2}{s - M_\sigma^2}, \quad (\text{C26})$$

which is the amplitude in the (original) coordinates $\varphi = (\vec{\pi}, \sigma)$ [30, 32]. For $s = M_\pi^2$, the amplitude $\mathfrak{A}(s, t, u)$ vanishes, since the four-pion vertex and the s -channel σ -exchange diagram cancel each other. This cancellation phenomenon is known as the ‘‘Adler zero’’ [77, 85, 105]. Equation (C26) is the universal tree-level amplitude of the SO(4)-symmetric LSM (with pions and the σ -meson).

Appendix D: FRG flow of scale-dependent quantities

The flow equations for the scale-dependent couplings in Eq. (7) and the corresponding vertex functions are obtained by calculating the functional derivatives of Eq. (5). The Taylor coefficients of the effective potential are determined by Eq. (8). All differential equations are evaluated at the k -independent expansion point $\varphi_0^2 = \text{const.}$ of the potential, which is chosen to be slightly larger than the IR minimum ($\varphi_0^2 \gtrsim f_\pi^2$). The latter is the physical vacuum configuration of the model, where the masses and other observables are defined. The integration of momentum modes is initialized at $\Lambda_\chi = 1.2 \text{ GeV} \simeq 4\pi f_\pi$. At this scale, the potential $V(\varphi^2)$ is assumed to be of the form given in Eq. (8), with $\alpha_1, \alpha_2 > 0$ and $\alpha_n = 0$, $n > 2$. The other scale-dependent quantities are initialized as listed in Table V. The fixing of the chiral-invariant mass m_0 to a common value among all approximations determines the Yukawa couplings y_1 and y_2 in the MF and one-loop approximations and the LPA, cf. Fig. 12(a) in Appendix E. It leaves only two adjustable

model parameters (for the MF, one-loop, and LPA cases), namely, the Taylor coefficients α_1 and α_2 , to account for the breaking scale Λ_χ and the IR observables (including the pion-pion scattering lengths). The expansion point of the effective potential and the h -parameter are indirectly fixed by the pion decay constant f_π and the pion mass M_π , respectively. The integration is then carried out down to $k = 0$, and additionally up to $k = 1.5$ GeV in order to verify chiral symmetry restoration above Λ_χ . This upper limit of the considered k -range is set to the largest mass scale of the model, $M_{N(1535)} \simeq 1.5$ GeV.

Employing the language of Feynman diagrams, the flow equations for the effective potential V , the chiral-invariant mass m_0 , the Yukawa couplings y_1 and y_2 , as well as the wave-function renormalizations Z and Z^ψ read

$$\partial_k V_k = \mathcal{V}^{-1} \partial_k \Gamma_k = \mathcal{V}^{-1} \left(\frac{1}{2} \text{diagram}_\sigma + \frac{1}{2} \text{diagram}_\pi - \text{diagram}_\Psi \right), \quad (\text{D1})$$

$$\begin{aligned} \partial_k m_{0,k} &= -\frac{1}{4} \mathcal{V}^{-1} \text{tr}_\gamma \left[\frac{\delta^2 \partial_k \Gamma_k}{\delta \bar{\Psi}_{f_1, p_1}(0) \delta \Psi_{f_2, p_2}(0)} \Big|_{f_1=f_2=1, p_1=1, p_2=2} \right] \\ &= -\frac{1}{4} \mathcal{V}^{-1} \text{tr}_\gamma \left(\frac{1}{2} \text{diagram}_\sigma + \frac{1}{2} \text{diagram}_\pi \right. \\ &\quad \left. - \text{diagram}_\sigma - \text{diagram}_\pi \right), \quad (\text{D2}) \end{aligned}$$

$$\begin{aligned} \partial_k y_{1,k} &= \frac{i}{24} \mathcal{V}^{-1} \text{tr}_{\gamma, \text{flavor}} \left[\frac{\delta^3 \partial_k \Gamma_k}{\delta \pi^a(0) \delta \bar{\Psi}_{p_1}(0) \delta \Psi_{p_2}(0)} \Big|_{p_1=p_2=1} \gamma_5 \tau^a \right] \\ &= \frac{i}{24} \mathcal{V}^{-1} \text{tr}_{\gamma, \text{flavor}} \left(\begin{aligned} & -\frac{1}{2} \text{diagram}_\sigma - \frac{1}{2} \text{diagram}_\pi - \frac{1}{2} \text{diagram}_\sigma \\ & -\frac{1}{2} \text{diagram}_\pi - \frac{1}{2} \text{diagram}_\sigma - \frac{1}{2} \text{diagram}_\pi \\ & + \text{diagram}_\sigma + \text{diagram}_\pi + \text{diagram}_\sigma \end{aligned} \right) \end{aligned}$$

$$\left. \begin{array}{c} + \left(\text{Diagram 1} + \text{Diagram 2} + \text{Diagram 3} \right) \gamma_5 \tau^a, \end{array} \right. \quad (\text{D3})$$

$$\partial_k y_{2,k} = \frac{i}{24} \mathcal{V}^{-1} \text{tr}_{\gamma, \text{flavor}} \left[\frac{\delta^3 \partial_k \Gamma_k}{\delta \pi^a(0) \delta \bar{\Psi}_{\mathbf{p}_1}(0) \delta \Psi_{\mathbf{p}_2}(0)} \Big|_{\mathbf{p}_1 = \mathbf{p}_2 = 2} \gamma_5 \tau^a \right], \quad (\text{D4})$$

$$\begin{aligned} \partial_k Z_k &= \mathcal{V}^{-1} \frac{d}{dq^2} \Big|_{q^2=0} \frac{\delta^2 \partial_k \Gamma_k}{\delta \pi^1(-q) \delta \pi^1(q)} \\ &= \mathcal{V}^{-1} \frac{d}{dq^2} \Big|_{q^2=0} \left(\frac{1}{2} \left(\text{Diagram 4} + \text{Diagram 5} \right) - \text{Diagram 6} \right. \\ &\quad \left. - \frac{1}{2} \left(\text{Diagram 7} + \text{Diagram 8} \right) \right), \end{aligned} \quad (\text{D5})$$

$$\partial_k Z_k^\psi = -\frac{i}{4} \mathcal{V}^{-1} \frac{d}{dq^2} \Big|_{q^2=0} \text{tr}_\gamma \left[\frac{\delta^2 \partial_k \Gamma_k}{\delta \bar{\Psi}_{f_1, \mathbf{p}_1}(q) \delta \Psi_{f_2, \mathbf{p}_2}(q)} \Big|_{f_1 = f_2 = 1, \mathbf{p}_1 = \mathbf{p}_2 = 1} \gamma_\mu q_\mu \right]. \quad (\text{D6})$$

In the graphical translation, we left out particular leg specifications and intrinsic multiplicity/symmetry or sign factors. For the flow equations (D4) and (D6), we have the same Feynman diagrams as in Eqs. (D3) and (D2), respectively. The object Ψ represents the vector $(\psi_1, \psi_2)^\top$ in Eq. (A7) of Appendix A; it carries the SU(2) flavor indices f_1, f_2 and the SO(2) parity (or rotation) indices $\mathbf{p}_1, \mathbf{p}_2$ (in addition to its spin indices, which are not shown). The different fields of the nucleon-meson model are “highlighted” in red (pions), blue (σ -field), and black/gray (fermions). Finally, the spacetime volume is written as \mathcal{V} . The regulator insertions, which are colored equally as the propagator lines, are proportional to the wave-function renormalizations,

$$R_k^\pi(q^2) \equiv R_k^\sigma(q^2) = Z_k q^2 r_k(q^2), \quad (\text{D7})$$

$$R_k^\psi(q^2) = i Z_k^\psi \gamma_\mu q_\mu r_k^\psi(q^2), \quad R_{k, f_1 f_2, \mathbf{p}_1 \mathbf{p}_2}^\Psi(q^2) = R_k^\psi(q^2) \delta_{f_1 f_2} \delta_{\mathbf{p}_1 \mathbf{p}_2}, \quad (\text{D8})$$

where we take the optimized Litim regulators as the shape functions [106],

$$r_k(q^2) \equiv r\left(\frac{q^2}{k^2}\right) = \left(\frac{k^2}{q^2} - 1\right) \Theta(k^2 - q^2), \quad (\text{D9})$$

$$r_k^\psi(q^2) \equiv r^\psi\left(\frac{q^2}{k^2}\right) = \left(\sqrt{\frac{k^2}{q^2}} - 1\right) \Theta(k^2 - q^2). \quad (\text{D10})$$

The symbol $\Theta(\cdot)$ denotes the Heaviside step function. The regulators obey the limits

$$\lim_{k \rightarrow 0} R_k = 0, \quad \lim_{k \rightarrow \Lambda \rightarrow \infty} R_k = \infty, \quad \lim_{q \rightarrow 0} R_k > 0, \quad \lim_{q \rightarrow \infty} R_k = 0. \quad (\text{D11})$$

In the first limit, one recovers the (quantum) effective action Γ . The second leads to $\Gamma_k \rightarrow S$ (for $k \rightarrow \Lambda \rightarrow \infty$). The last two limits imply the massive suppression of soft modes only during the integration process. To calculate the diagrams, we used the dedicated algebra tools DoFun [107], FormTracer [108], and FeynCalc [109].

Table V. Initialization parameters for the integration of momentum modes.

Approximation	φ_0 [MeV]	α_1 [MeV ²]	α_2	m_0 [MeV]	y_1	y_2	Z	Z^ψ	h [MeV ³]
FRG (LPA')	60.74	510 ²	58.2	770	12.0	19.4	1.6	1.4	2.62×10^6
FRG (LPA)	91.92	330 ²	10.5	824.45	6.765	13.06	1.0	1.0	1.80×10^6
One-loop	91.57	460 ²	21.3	824.45	6.765	13.06	1.0	1.0	1.80×10^6
MF	91.80	598 ²	37.5	824.45	6.765	13.06	1.0	1.0	1.80×10^6

The fermion propagator has off-diagonal elements in the basis of Ψ . The two-point function (plus regulator) on the right-hand side of Eq. (5) has in momentum space the structure

$$\mathcal{V}^{-1} \Gamma_k^{(2) \bar{\Psi} \Psi} + R_k^\Psi \sim \begin{pmatrix} iZ^\psi \gamma_\mu q_\mu \left[1 + r_k^\psi(q^2) \right] - y_1 \sigma & -m_0 \\ -m_0 & iZ^\psi \gamma_\mu q_\mu \left[1 + r_k^\psi(q^2) \right] + y_2 \sigma \end{pmatrix}. \quad (\text{D12})$$

Its inverse, i.e., the fermionic propagator tensor $G_k^{\Psi \bar{\Psi}}$, is given by

$$G_{k,d_1 d_2, f_1 f_2, p_1 p_2}^{\Psi \bar{\Psi}}(q, q') = - \left\{ \begin{aligned} & \left[f_k^{++}(q^2) \delta_{d_1 d_2} + i g_{k,\mu}^{++}(q) (\gamma_\mu)_{d_1 d_2} \right] \delta_{p_1 1} \delta_{p_2 1} \\ & \left[f_k^{+-}(q^2) \delta_{d_1 d_2} + i g_{k,\mu}^{+-}(q) (\gamma_\mu)_{d_1 d_2} \right] \delta_{p_1 1} \delta_{p_2 2} \\ & \left[f_k^{-+}(q^2) \delta_{d_1 d_2} + i g_{k,\mu}^{-+}(q) (\gamma_\mu)_{d_1 d_2} \right] \delta_{p_1 2} \delta_{p_2 1} \\ & \left[f_k^{--}(q^2) \delta_{d_1 d_2} + i g_{k,\mu}^{--}(q) (\gamma_\mu)_{d_1 d_2} \right] \delta_{p_1 2} \delta_{p_2 2} \end{aligned} \right\} \delta_{f_1 f_2} \delta(q - q'). \quad (\text{D13})$$

The indices d_1, d_2 are those of the Dirac (spin) space. The functions f_k (even in the momentum q) and $g_{k,\mu}$ (odd in the momentum) are deduced as

$$f_k^{\pm\pm}(q^2) = \pm \mathcal{N}_k(q^2) \left[(Z^\psi)^2 q^2 (1 + r_k^\psi)^2 y_{1/2} \sigma + m^+ m^- y_{2/1} \sigma \right], \quad (\text{D14})$$

$$f_k^{\pm\mp}(q^2) = \mathcal{N}_k(q^2) \left[(Z^\psi)^2 q^2 (1 + r_k^\psi)^2 + m^+ m^- \right] m_0, \quad (\text{D15})$$

$$g_{k,\mu}^{\pm\pm}(q) = \mathcal{N}_k(q^2) Z^\psi q_\mu (1 + r_k^\psi) \left[(Z^\psi)^2 q^2 (1 + r_k^\psi)^2 + (m^+)^2 + (m^-)^2 - m_0^2 - (y_{1/2} \sigma)^2 \right], \quad (\text{D16})$$

$$g_{k,\mu}^{\pm\mp}(q) = - \mathcal{N}_k(q^2) Z^\psi q_\mu (1 + r_k^\psi) (m^+ - m^-) m_0, \quad (\text{D17})$$

with the normalization factor

$$\mathcal{N}_k(q^2) = \left\{ \left[(Z^\psi)^2 q^2 (1 + r_k^\psi)^2 + (m^+)^2 \right] \left[(Z^\psi)^2 q^2 (1 + r_k^\psi)^2 + (m^-)^2 \right] \right\}^{-1}. \quad (\text{D18})$$

For $m_0 = 0$, the off-diagonal elements vanish, $f_k^{\pm\mp} = g_{k,\mu}^{\pm\mp} = 0$, and the diagonal elements become

$$f_k^{\pm\pm}(q^2) = \pm \frac{y_{1/2} \sigma}{(Z^\psi)^2 q^2 (1 + r_k^\psi)^2 + (y_{1/2} \sigma)^2}, \quad g_{k,\mu}^{\pm\pm}(q) = \frac{Z^\psi q_\mu (1 + r_k^\psi)}{(Z^\psi)^2 q^2 (1 + r_k^\psi)^2 + (y_{1/2} \sigma)^2}, \quad (\text{D19})$$

which are the well-known propagator functions of quark-meson-type models with the fermion masses $y_{1/2} \sigma$ [37, 38]. As an example, the fermionic loop in the flow equation (D1) of the effective potential is calculated as

$$- \text{loop} = -8\mathcal{V} \int_q \left[g_{k,\mu}^{++}(q) h_{k,\mu}(q) + g_{k,\mu}^{--}(q) h_{k,\mu}(q) \right], \quad (\text{D20})$$

$$h_{k,\mu}(q) = Z^\psi q_\mu \left[\partial_k r_k^\psi(q^2) - \frac{\eta^\psi}{k} r_k^\psi(q^2) \right], \quad (\text{D21})$$

$$\Rightarrow \quad \partial_k V_k|_{\text{fermions}} = - (5 - \eta^\psi) \frac{k^5}{20\pi^2} \left[\frac{1}{k^2 + (M^+)^2} + \frac{1}{k^2 + (M^-)^2} \right]. \quad (\text{D22})$$

As expected, the trace operation of the loop extracts the diagonal propagator parts, i.e., the physical eigenvalues of the fermions with the (squared) particle energies $k^2 + (M^\pm)^2$ and the physical masses M^\pm . In Eq. (D21), we introduced the anomalous dimension η^ψ . The bosonic and fermionic anomalous dimensions η and η^ψ parametrize the scaling of the wave-function renormalization factors,

$$\eta_k = -k \partial_k \ln Z_k, \quad \eta_k^\psi = -k \partial_k \ln Z_k^\psi. \quad (\text{D23})$$

The flow equations in terms of renormalized fields and couplings solely depend on the anomalous dimensions, see e.g. Eq. (D22), such that the absolute values of the factors Z and Z^ψ actually do not explicitly enter the physical solution of the equations.

The numeric solution of the differential equations for the Taylor coefficients α_n , $n = 1, \dots, N_\alpha$, is already (indirectly) plotted in Fig. 2 of Sec. IV, since the masses (16) can be expressed through the coefficients as follows:

$$M_\pi^2 = 2\tilde{V}'(f_\pi^2) \equiv 2 \sum_{n=1}^{N_\alpha} \frac{\tilde{\alpha}_n}{(n-1)!} (f_\pi^2 - \tilde{\varphi}_0^2)^{n-1}, \quad (\text{D24})$$

$$M_\sigma^2 = 2\tilde{V}'(f_\pi^2) + 4f_\pi^2 \tilde{V}''(f_\pi^2) \equiv 2 \left[\sum_{n=1}^{N_\alpha-1} \frac{\tilde{\alpha}_n + 2f_\pi^2 \tilde{\alpha}_{n+1}}{(n-1)!} (f_\pi^2 - \tilde{\varphi}_0^2)^{n-1} + \frac{\tilde{\alpha}_{N_\alpha}}{(N_\alpha-1)!} (f_\pi^2 - \tilde{\varphi}_0^2)^{N_\alpha-1} \right], \quad (\text{D25})$$

where we utilized the renormalized coefficients $\tilde{\alpha}_n = \alpha_n/Z^n$ and the renormalized expansion point $\tilde{\varphi}_0^2 = Z\varphi_0^2$. Instead of deriving the masses from the scale-dependent minimum $\tilde{\sigma}_0$ of the effective potential, we alternatively compute their flow equations,

$$\partial_k \tilde{\sigma}_0 = -\tilde{\sigma}_0 \left[\frac{1}{2} \frac{\eta}{k} + \frac{2}{M_\sigma^2} \frac{\partial}{\partial \tilde{\varphi}^2} \Big|_{\tilde{\sigma}_0^2} \partial_k \tilde{V}_k(\tilde{\varphi}^2) \right], \quad (\text{D26})$$

$$\partial_k M_\pi = M_\pi \left[\frac{1}{2} \frac{\eta}{k} + \frac{1}{M_\sigma^2} \frac{\partial}{\partial \tilde{\varphi}^2} \Big|_{\tilde{\sigma}_0^2} \partial_k \tilde{V}_k(\tilde{\varphi}^2) \right], \quad (\text{D27})$$

$$\partial_k M_\sigma = M_\sigma \left\{ \frac{1}{2} \frac{\eta}{k} + \frac{1}{M_\sigma^2} \left[\frac{M_\pi^2 - 8\tilde{\sigma}_0^2 \tilde{V}''(\tilde{\sigma}_0^2) - 8\tilde{\sigma}_0^4 \tilde{V}^{(3)}(\tilde{\sigma}_0^2)}{M_\sigma^2} \frac{\partial}{\partial \tilde{\varphi}^2} \Big|_{\tilde{\sigma}_0^2} + 2\tilde{\sigma}_0^2 \frac{\partial^2}{(\partial \tilde{\varphi}^2)^2} \Big|_{\tilde{\sigma}_0^2} \right] \partial_k \tilde{V}_k(\tilde{\varphi}^2) \right\}, \quad (\text{D28})$$

and evaluate them on the solution for the Taylor coefficients. In the UV, i.e., $\tilde{\sigma}_0 \rightarrow 0$ and $M_\sigma \rightarrow M_\pi$, the flow equation for M_σ reduces to

$$\partial_k M_\sigma = M_\pi \left[\frac{1}{2} \frac{\eta}{k} + \frac{1}{M_\pi^2} \frac{\partial}{\partial \tilde{\varphi}^2} \Big|_{\tilde{\sigma}_0^2} \partial_k \tilde{V}_k(\tilde{\varphi}^2) \right] \equiv \partial_k M_\pi. \quad (\text{D29})$$

Since the above equations are in their renormalization-group-invariant form, meaning that they neither explicitly depend on Z nor Z^ψ [as discussed below Eq. (D23)], one may rescale the values of the wave-function renormalizations in the definition of the bare boson and fermion masses,

$$m_{\pi/\sigma}^{\text{bare}} := \sqrt{\frac{Z_k}{Z_{k_{\text{IR}}}}} M_{\pi/\sigma} \equiv \frac{m_{\pi/\sigma}}{Z_0^{1/2}}, \quad m^{\pm, \text{bare}} := \frac{Z_k^\psi}{Z_{k_{\text{IR}}}^\psi} M^\pm \equiv \frac{m^\pm}{Z_0^\psi}. \quad (\text{D30})$$

This leads (in the LPA') to the coincidence of bare and renormalized masses at $k = 0$, cf. Fig. 7(a), which combines the curves from Fig. 2(a) (solid lines) with the bare ones (dashed lines in the respective colors). It reveals that the bare fermion masses are notably smaller over the almost entire k -range, while the bosonic masses mainly differ for scales above Λ_χ . For the sake of completeness, Fig. 7(b) shows the (normalized) flows of the wave-function renormalization factors Z and Z^ψ . Interestingly, the flow of the fermionic wave-function renormalization Z^ψ flattens out in the UV, which is not observed for its bosonic counterpart Z ; the scaling behavior of the renormalized and bare fermion masses is nearly “parallel” above the chiral-symmetry breaking scale, see once more Fig. 7(a).

In Fig. 7(c), we analyzed the characteristic “down-bending” of the σ -mass in the FRG truncations (LPA and LPA') and isolated its triggers. The dash-dotted line, which we named “bare,” is the scale evolution of the σ -mass for taking the bare two-point function $S^{(2)}$ as input for the flow equations—as it is done in the MF and one-loop approximations. The absence of interactions beyond quartic order in $S^{(2)}$ leads to the rather monotonous behavior below the scale Λ_χ ,

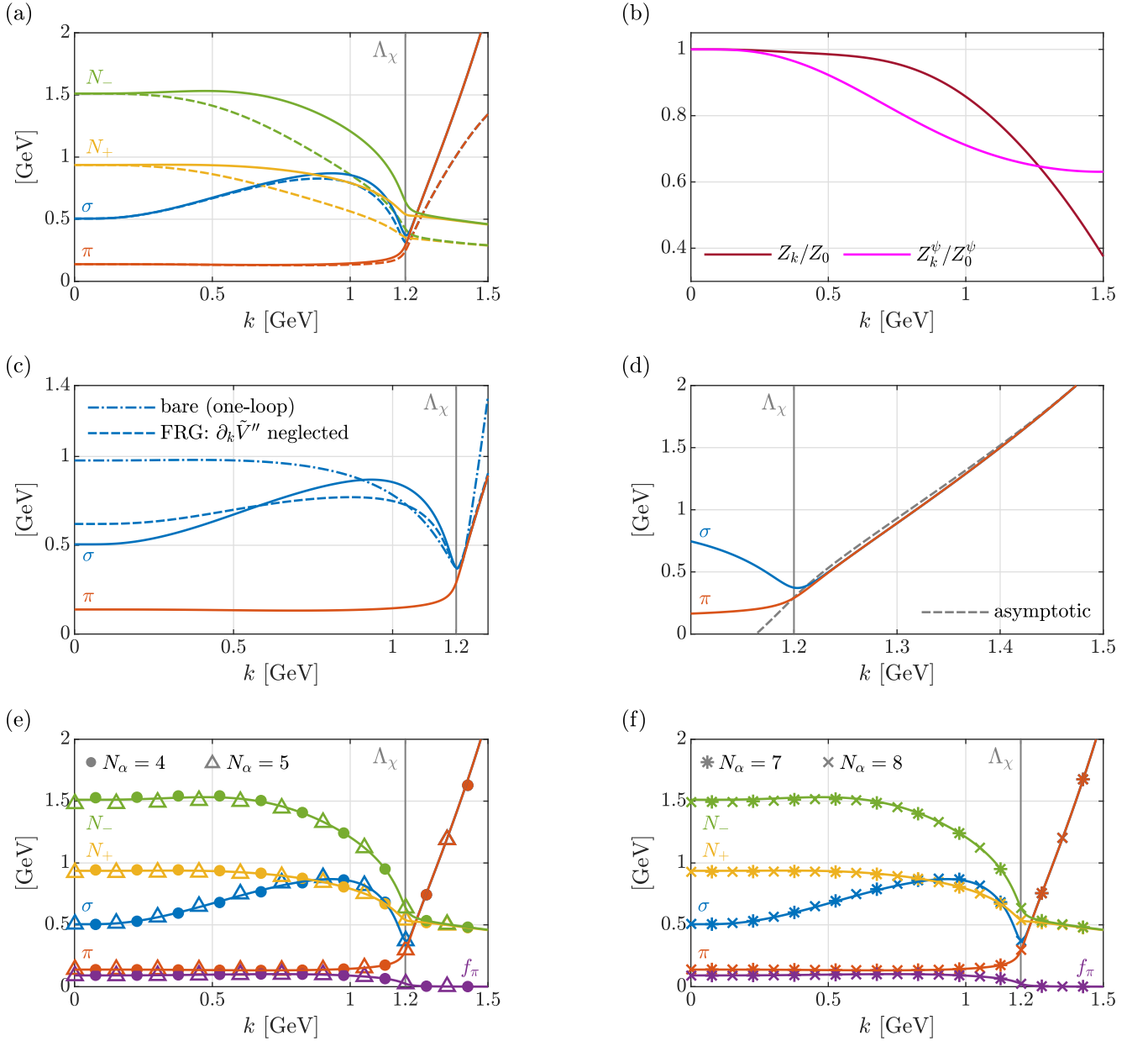


Figure 7. Scale-dependent (renormalized and bare) masses, scale evolution of the wave-function renormalization, and numeric analysis of the LPA' flow. (a) Boson and fermion masses [solid lines; identical to Fig. 2(a)] in comparison to the bare quantities (dashed lines). (b) Scale evolution of the factors Z and Z^ψ (normalized to one in the IR). (c) Numeric analysis of the flow of the σ -mass (detailed explanations are given in the main text). (d) Asymptotic behavior of the boson masses for large k -scales. (e) and (f) Variations of the N_α -parameter of the effective potential (8) and the effect on the numeric results (solid lines: $N_\alpha = 6$).

where all lines are fixed. Secondly, the dashed line stands for the FRG flow of M_σ , which obeys Eq. (D28), but where we omitted the last contribution proportional to $\partial_k \tilde{V}''$. The resulting curve is “damped” as compared to the total flow (solid line) and the IR mass shrinks to smaller values. The appearing non-monotonicity then gets amplified by the inclusion of the flow of \tilde{V}'' , which reinforces the influence of the higher Taylor coefficients. The IR mass M_σ , in summary, decreases by a factor of almost 2. The asymptotic scale evolution of the bosonic masses in the UV, following Eq. (D29), is verified in Fig. 7(d).

Against variations of the N_α -parameter of the effective potential (8), the numeric masses and the pion decay constant are relatively robust in the LPA', i.e., the flows and the physical IR values are not substantially affected; see Figs. 7(e) and 7(f) for changes of N_α to smaller ($N_\alpha = 4, 5$) and larger integers ($N_\alpha = 7, 8$), respectively. The solid lines in both subfigures indicate the flows of Figs. 2(a) and 2(b) ($N_\alpha = 6$). Clearly, the effect of increasing N_α , which amounts to

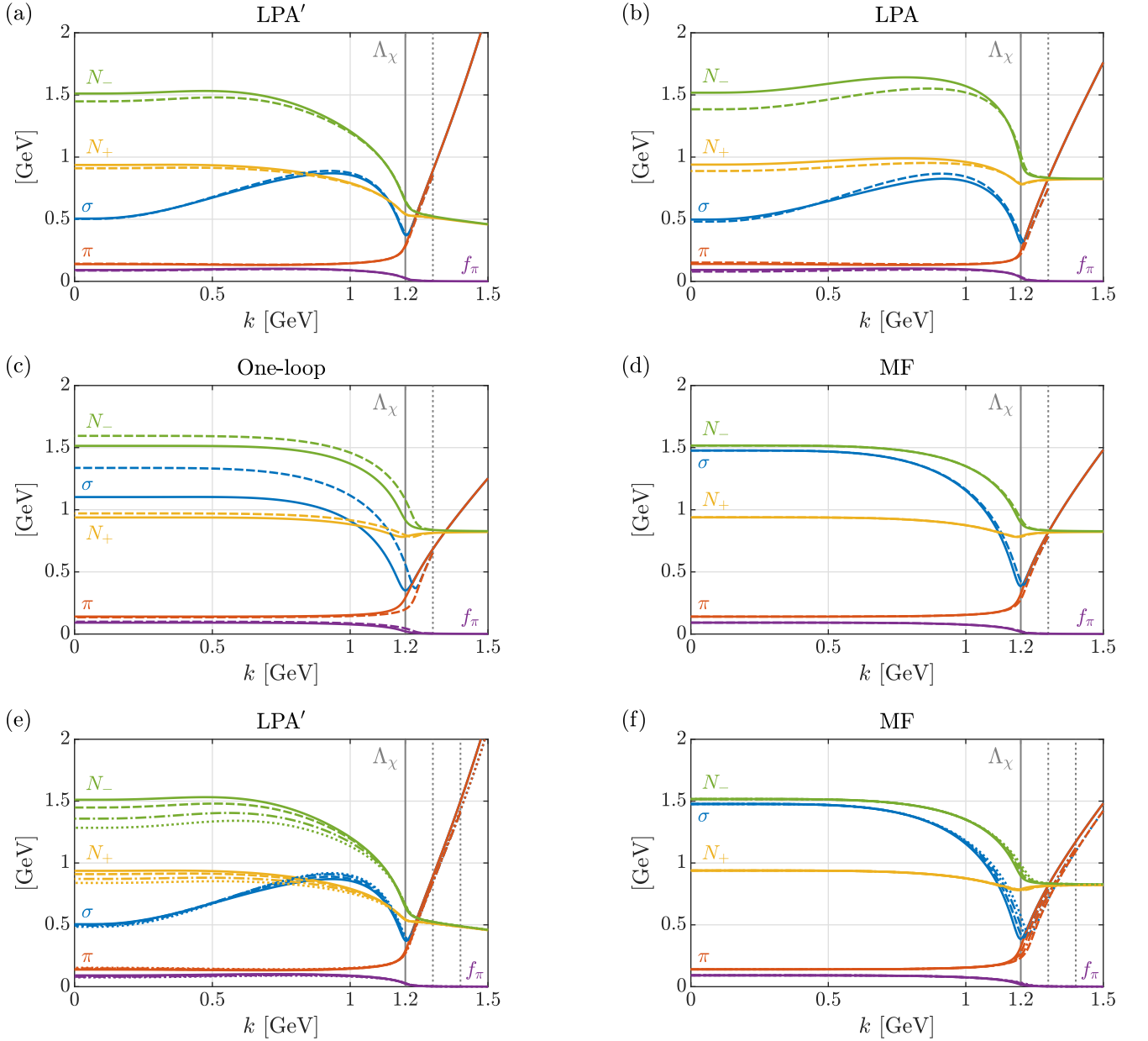


Figure 8. Influence of higher Taylor coefficients (α_n , $n > 2$). (a) to (d) Shift of the initialization scale $\Lambda_\chi = 1.2$ GeV to 1.3 GeV (vertical gray-dotted line) in all approximations (LPA', LPA, one-loop, and MF). The integration towards the IR starting from the cutoff 1.3 GeV (dashed lines) is initialized as a cubic polynomial in φ^2 , cf. Eq. (8). This is compared to the corresponding original flows (solid lines; quadratic polynomials tuned at $\Lambda_\chi = 1.2$ GeV). The respective initial values of the coefficients and couplings at 1.3 GeV are obtained by integrating the original flow “upwards” from Λ_χ to 1.3 GeV and then dropping the Taylor coefficients $\alpha_{n > 3}$. (e) Initialization of the LPA'-flow at 1.3 GeV, 1.4 GeV, and 1.5 GeV (dashed, dash-dotted, and dotted lines, respectively). The initial values of the Taylor coefficients and couplings are determined as in panel (a). (f) Analogous figure to panel (e) for the MF approximation, demonstrating the cutoff independence of the IR observables.

less than 2% in the (most relevant) quantities f_π , M_π , and M_σ , can be smoothed out by slightly readjusting the UV parameters. Thus choosing $N_\alpha = 6$ [as also argued by Refs. [38, 42, 55]] does not a priori distort the main conclusion of our work. In particular, the crucial value of M_σ changes by less than 0.5% for smaller or larger values of N_α .

To numerically support the ansatz for the effective potential as a quadratic polynomial (in φ^2) at $\Lambda_\chi = 1.2$ GeV, we estimate the influence of the higher Taylor coefficients (α_n , $n > 2$) that could be present at Λ_χ by increasing the initialization scale to 1.3 GeV. This is illustrated in Figs. 8(a) to 8(d) (see the vertical gray-dotted line as compared to the gray line Λ_χ); the dashed curves represent the integration of the flow equations starting with a cubic potential

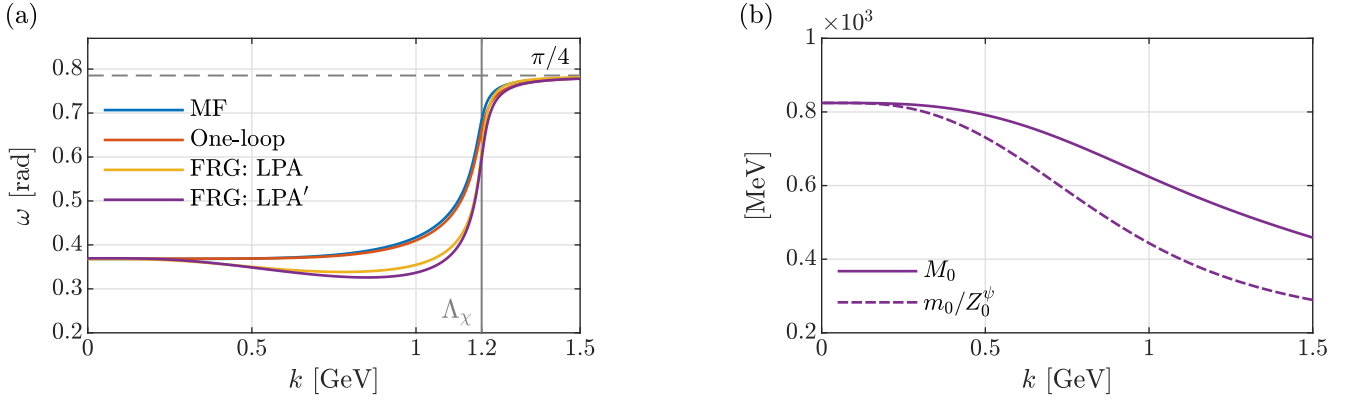


Figure 9. Scale evolution of the rotation angle ω and the (renormalized and bare) chiral-invariant mass. (a) The rotation angle of Eq. (A8) is plotted against the k -scale for all four approximations, which are considered in the main part of this publication. The angle ω approaches the limit of $\pi/4$ rad (horizontal dashed line) in the UV. (b) Renormalized and bare chiral-invariant masses M_0 and m_0/Z_0^ψ , respectively, as functions of the scale k (in the LPA'); the bare mass is normalized according to Eq. (D30).

($\alpha_n > 0$, $n \leq 3$, and $\alpha_n = 0$, $n > 3$) initialized at 1.3 GeV in the chiral-restored phase, such that all higher coefficients already acquire nonzero values at Λ_χ . The respective initial values of the coefficients and couplings are obtained by integrating the original quadratic potential “upwards” from Λ_χ to 1.3 GeV and then dropping the coefficients $\alpha_{n > 3}$. Let us remark that it was necessary to involve (at least) the first three Taylor coefficients in this upwards-integrating procedure in order to find stable solutions for the subsequent “downwards” integration starting from 1.3 GeV (which was e.g. not possible for a similar procedure solely involving the first two coefficients). Hence, the dashed curves can be interpreted as alternative UV tuning of the flows in the chiral-restored phase above Λ_χ . It obviously turns out that the overall picture does not change drastically, especially, the boson masses and the pion decay constant appear to be only mildly affected in the LPA', LPA, and the MF approximation (which is the most important criterion regarding the computation of the pion-pion scattering lengths and the σ -mass prediction). In the MF case, the IR values of the observables are actually not affected at all. Only the one-loop integration in Fig. 8(c) exhibits a substantial difference in the chiral breaking scale and the IR value of the isoscalar mass (but it still produces a σ -mass larger than 1 GeV).

Figure 8(e) shows the LPA'-flows initialized at UV scales even larger than 1.3 GeV (1.4 GeV and 1.5 GeV), compare the additionally added gray-dotted lines. Again, the respective starting values were computed by upwards integration with a cubic potential as described in the context of Fig. 8(a). Once more, the bosonic observables are rather robust and to some extent almost independent of the initialization scale as well as the presence of the higher Taylor coefficients already at Λ_χ . The largest effects are found in the IR fermion masses M^\pm . Finally, Fig. 8(e) demonstrates the cutoff independence of the IR results in the MF approximation also for the initialization scales of 1.4 GeV and 1.5 GeV. The reason for this cutoff independence lies in the fact that the integration of each of the Taylor coefficients itself is independent of the others and exclusively depends on the fermionic loop contribution, see also Appendix E.

The angle ω of Eq. (A8) quantifies the rotation from the unphysical parity-even basis towards the physical parity-odd case; it is presented in Fig. 9(a) and basically comprises the scale dependence of the chiral-invariant mass M_0 and the Yukawa couplings \tilde{y}_1 and \tilde{y}_2 (besides the condensate $\tilde{\sigma}_0$). The numeric angle ω roughly varies between 0.3 rad and 0.8 rad, where it approaches the limit

$$\lim_{\tilde{\sigma}_0 \rightarrow 0} \omega = \frac{\pi}{4} \text{ rad} \quad (\text{D31})$$

in the chiral-restored phase ($k > \Lambda_\chi$). The latter is dominated by the asymptotic behavior of $\tilde{\sigma}_0 \rightarrow 0$. In the broken phase ($k < \Lambda_\chi$), the curves for the different approximations split and eventually merge in the IR limit, $k \rightarrow 0$; they exhibit again the same (non-)monotonicity as observed in Figs. 2 and 5 of Sec. IV, ending up around $\omega = 0.37$ rad. The merging of the lines for $k \rightarrow 0$ is caused by the common IR values of the chiral-invariant mass and the Yukawa couplings among all approximations, cf. the discussion below.

Figure 9(b) lets us furthermore comment on the value of the renormalized and bare chiral-invariant mass parameters M_0 and $m_0^{\text{bare}} := m_0/Z_0^\psi$ (in the LPA'). The (renormalized) physical mass matches the range of $M_0 \simeq 450$ MeV to $M_0 \simeq 825$ MeV along its evolution (w.r.t. the energy-momentum scale k). It therefore principally conforms with the values cited in the Introduction. The bare mass m_0^{bare} turns out to be smaller, but it is still situated in the somewhat wider range of $200 \text{ MeV} \leq m_0^{\text{bare}} \leq 900 \text{ MeV}$, as also mentioned at the very beginning of this work. In the IR, we find

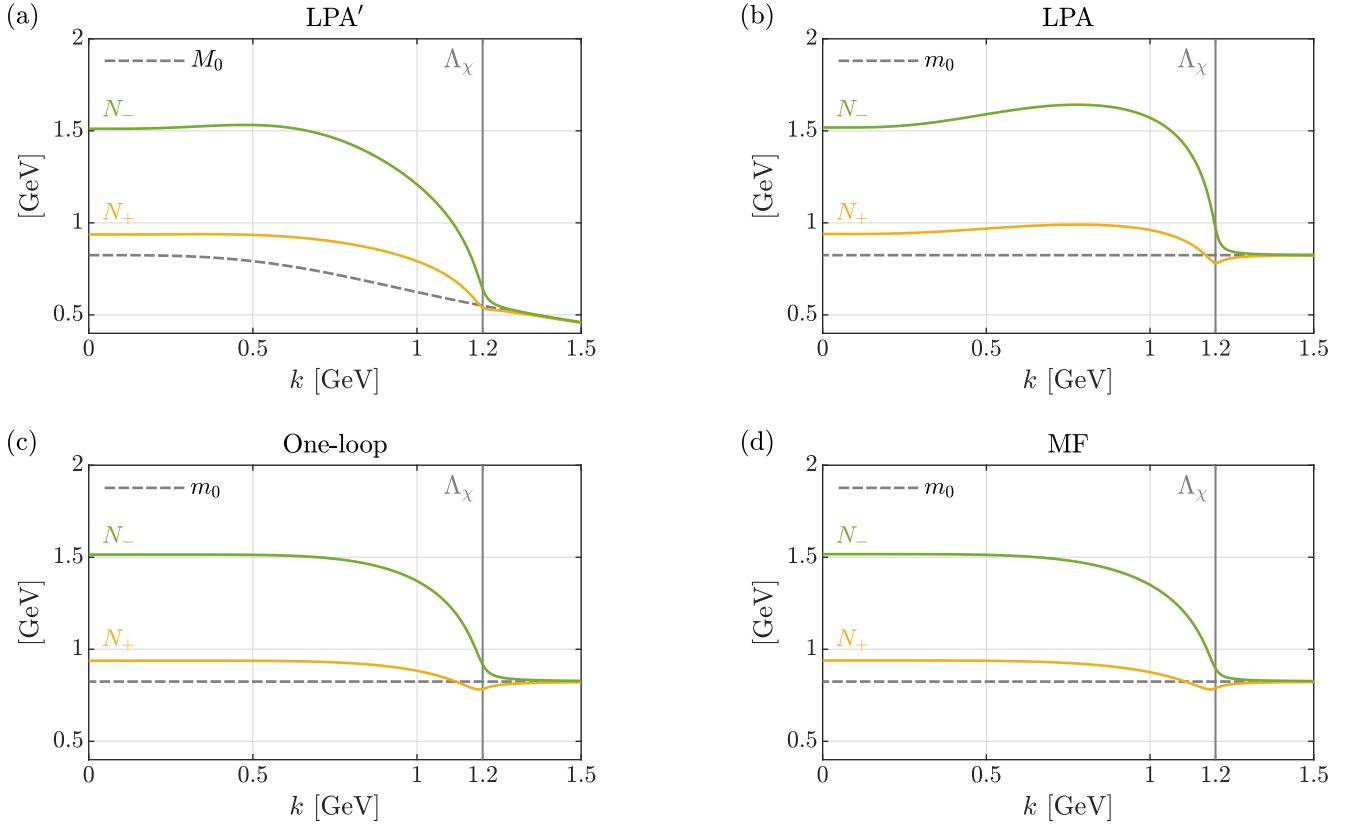


Figure 10. Scale evolution of the fermion masses M^\pm in comparison to the chiral-invariant mass. (a) The mass parameters M_0 and $m_0 = Z^\psi M_0$ are both considered as scale dependent in the LPA'. (b), (c), and (d) The mass parameters are taken as scale independent in the LPA, one-loop, and MF approximations, respectively.

a chiral-invariant mass of $M_0 \simeq 824.5$ MeV and the degeneracy of the (physical) fermion masses M^\pm with M_0 in the chiral-restored phase is demonstrated in Fig. 10(a).

Concerning the simpler approximations (LPA, one-loop, and MF), the (scale-independent) mass parameter m_0 is consequently set to the LPA'-value of 824.5 MeV. In all three truncations, the fermion masses m^\pm consistently fall into line with m_0 around the scale of Λ_χ (and beyond), cf. Figs. 10(b) to 10(d). Note that these results were generated under the constraints of chiral symmetry breaking occurring at Λ_χ and the “successful” reproduction of the pion-pion scattering lengths as IR observables within the nucleon-meson model.

Similarly to the fermion masses, the Yukawa couplings of Eqs. (12) to (14) (in the physical basis) become degenerate in the symmetric phase, $\tilde{\sigma}_0 \rightarrow 0$, as it was outlined below Eq. (14) in Sec. II. In the LPA', the expressions $(\tilde{y}_1 \pm \tilde{y}_2)/2$ are scale dependent themselves [cf. Figs. 11(a) and 11(b)], whereas the respective terms are assumed to be constant in the other approximations [cf. Figs. 11(c) to 11(h)]. The scale dependence of the Yukawa couplings appears to be rather mild, except for scales close to the crossover transition. The fixing of the chiral-invariant mass parameter to the LPA'-value guarantees that the Yukawa couplings attain the same IR values in all approximations.

Appendix E: Analytic one-loop integration and isoscalar-mass prediction

1. Analytic integration and renormalized effective potential

The flow equation for the effective potential V is given by

$$\partial_k V_k = \frac{k^5}{32\pi^2} \left\{ \frac{3}{k^2 + m_\pi^2} + \frac{1}{k^2 + m_\sigma^2} - 8 \left[\frac{1}{k^2 + (m^+)^2} + \frac{1}{k^2 + (m^-)^2} \right] \right\}, \quad (\text{E1})$$

where we have replaced $\Gamma_k^{(2)}$ by $\Gamma^{(2)}|_\Lambda \equiv S^{(2)}$ with the UV cutoff Λ on the right of the flow equation, cf. once again Eq. (62) in Sec. IV. This means that the squared masses m_π^2 , m_σ^2 , and $(m^\pm)^2$ are independent of the integration variable

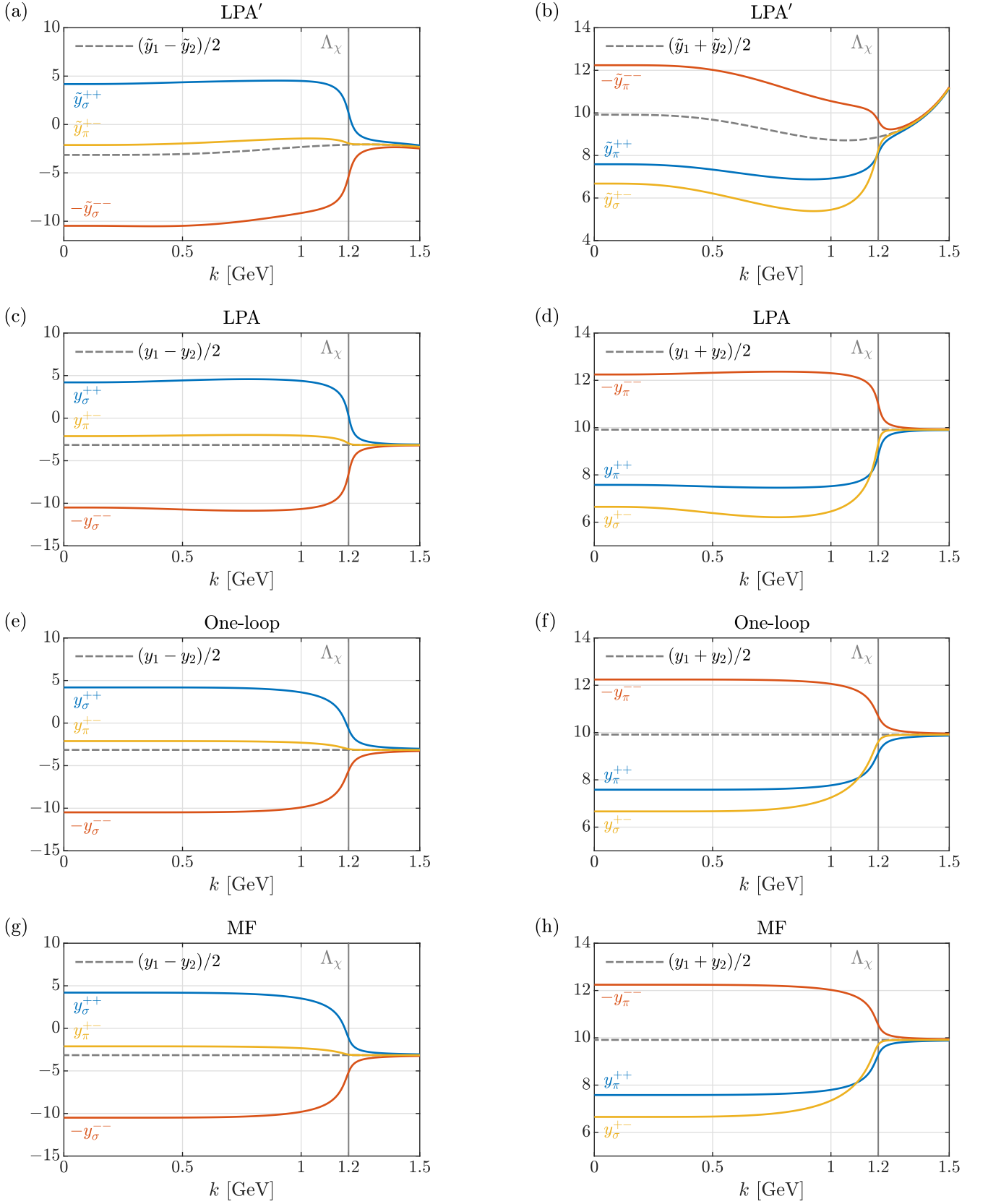


Figure 11. Scale evolution of the Yukawa couplings (in the physical basis) and for the four different approximations/truncations. In the left column, we collected the couplings that tend to the expression $(\tilde{y}_1 - \tilde{y}_2)/2$ [or $(y_1 - y_2)/2$] for large scales in the UV. In the right column, the corresponding couplings converge to the numeric value of $(\tilde{y}_1 + \tilde{y}_2)/2$ [or $(y_1 + y_2)/2$].

k. These are given by

$$m_\pi^2(\sigma^2) = 2V'_\Lambda(\sigma^2) \equiv 2 [\alpha_{1,\Lambda} + \alpha_{2,\Lambda} (\sigma^2 - \varphi_0^2)], \quad (\text{E2})$$

$$m_\sigma^2(\sigma^2) = 2V'_\Lambda(\sigma^2) + 4\sigma^2 V''_\Lambda(\sigma^2) \equiv 2 [\alpha_{1,\Lambda} + \alpha_{2,\Lambda} (3\sigma^2 - \varphi_0^2)], \quad (\text{E3})$$

$$m^\pm(\sigma) = \frac{1}{2} \left[\pm\sigma(y_1 - y_2) + \sqrt{\sigma^2(y_1 + y_2)^2 + 4m_0^2} \right], \quad (\text{E4})$$

where we used

$$V_\Lambda(\sigma^2) = \alpha_{1,\Lambda} (\sigma^2 - \varphi_0^2) + \frac{\alpha_{2,\Lambda}}{2} (\sigma^2 - \varphi_0^2)^2. \quad (\text{E5})$$

The integration of the flow equation for the effective potential can be carried out analytically. This yields the cutoff-regularized IR potential

$$V_0^{\text{one-loop}} = V_0^{\text{MF}} + \frac{1}{64\pi^2} \left\{ 3m_\pi^4 \left[\frac{1}{l^\pi} + \ln l^\pi - \ln(1 + l^\pi) \right] + m_\sigma^4 \left[\frac{1}{l^\sigma} + \ln l^\sigma - \ln(1 + l^\sigma) \right] \right\}, \quad (\text{E6})$$

$$V_0^{\text{MF}} = V_\Lambda - \frac{1}{8\pi^2} \left\{ (m^+)^4 \left[\frac{1}{l^+} + \ln l^+ - \ln(1 + l^+) \right] + (m^-)^4 \left[\frac{1}{l^-} + \ln l^- - \ln(1 + l^-) \right] \right\}, \quad (\text{E7})$$

with $l^{\pi/\sigma} = (m_{\pi/\sigma}/\Lambda)^2$ and $l^\pm = (m^\pm/\Lambda)^2$. We have dropped irrelevant terms proportional to Λ^4 . The first two terms in each of the square brackets are divergent for $l^{\pi/\sigma} \rightarrow 0$ and $l^\pm \rightarrow 0$, which corresponds to sending the cutoff to infinity, i.e., $\Lambda \rightarrow \infty$, keeping the masses constant. The MF approximation of the effective potential is obtained by neglecting the bosonic loop contributions in Eq. (E6), keeping only the one fermion loop.

Using the minimum condition of the IR potential $V_0^{\text{one-loop}}$, we compute the squared pion mass from the relation

$$\begin{aligned} h &= M_\pi^2 f_\pi = 2f_\pi \left. V_0^{\text{one-loop}'} \right|_{\sigma^2 = f_\pi^2} \\ &= 2f_\pi [\alpha_{1,\Lambda} + \alpha_{2,\Lambda} (f_\pi^2 - \varphi_0^2)] + \frac{1}{64\pi^2} \left(3 \frac{dm_\pi^4}{d\sigma} \left[\frac{1}{l^\pi} \frac{1}{2} \frac{1 + 2l^\pi}{1 + l^\pi} + \ln l^\pi - \ln(1 + l^\pi) \right] \right) \Big|_{f_\pi} \\ &\quad + \frac{dm_\sigma^4}{d\sigma} \left[\frac{1}{l^\sigma} \frac{1}{2} \frac{1 + 2l^\sigma}{1 + l^\sigma} + \ln l^\sigma - \ln(1 + l^\sigma) \right] \Big|_{f_\pi} - 8 \left\{ \frac{d(m^+)^4}{d\sigma} \left[\frac{1}{l^+} \frac{1}{2} \frac{1 + 2l^+}{1 + l^+} + \ln l^+ - \ln(1 + l^+) \right] \right\} \Big|_{f_\pi} \\ &\quad + \frac{d(m^-)^4}{d\sigma} \left[\frac{1}{l^-} \frac{1}{2} \frac{1 + 2l^-}{1 + l^-} + \ln l^- - \ln(1 + l^-) \right] \Big|_{f_\pi} \Bigg). \end{aligned} \quad (\text{E8})$$

The squared σ -mass is analogously computed as

$$\begin{aligned} M_\sigma^2 &= 2V_0^{\text{one-loop}''} + 4f_\pi^2 \left. V_0^{\text{one-loop}''} \right|_{f_\pi^2} \\ &= 2 [\alpha_{1,\Lambda} + \alpha_{2,\Lambda} (3f_\pi^2 - \varphi_0^2)] \\ &\quad + \frac{1}{64\pi^2} \left(3 \left\{ \frac{d^2 m_\pi^4}{d\sigma^2} \left[\frac{1}{l^\pi} \frac{1}{2} \frac{1 + 2l^\pi}{1 + l^\pi} + \ln l^\pi - \ln(1 + l^\pi) \right] \right\} \Big|_{f_\pi} - \left(\frac{dm_\pi^2}{d\sigma} \right)^2 \frac{1}{l^\pi} \frac{1}{(1 + l^\pi)^2} \Big|_{f_\pi} \right) \\ &\quad + \frac{d^2 m_\sigma^4}{d\sigma^2} \left[\frac{1}{l^\sigma} \frac{1}{2} \frac{1 + 2l^\sigma}{1 + l^\sigma} + \ln l^\sigma - \ln(1 + l^\sigma) \right] \Big|_{f_\pi} - \left(\frac{dm_\sigma^2}{d\sigma} \right)^2 \frac{1}{l^\sigma} \frac{1}{(1 + l^\sigma)^2} \Big|_{f_\pi} \\ &\quad - 8 \left\{ \frac{d^2 (m^+)^4}{d\sigma^2} \left[\frac{1}{l^+} \frac{1}{2} \frac{1 + 2l^+}{1 + l^+} + \ln l^+ - \ln(1 + l^+) \right] \right\} \Big|_{f_\pi} - \left[\frac{d(m^+)^2}{d\sigma} \right]^2 \frac{1}{l^+} \frac{1}{(1 + l^+)^2} \Big|_{f_\pi} \\ &\quad + \frac{d^2 (m^-)^4}{d\sigma^2} \left[\frac{1}{l^-} \frac{1}{2} \frac{1 + 2l^-}{1 + l^-} + \ln l^- - \ln(1 + l^-) \right] \Big|_{f_\pi} - \left[\frac{d(m^-)^2}{d\sigma} \right]^2 \frac{1}{l^-} \frac{1}{(1 + l^-)^2} \Big|_{f_\pi} \Bigg). \end{aligned} \quad (\text{E9})$$

If we now plug in the numeric values of Table V, we find that $M_\pi = 140.2$ MeV and $M_\sigma = 1102$ MeV for the one-loop approximation as well as $M_\pi = 140.0$ MeV and $M_\sigma = 1477$ MeV for the MF approximation, as quoted in Table II. In addition, Eq. (E8) can be used to numerically determine the pion decay constant f_π .

Writing the loop contributions in Eqs. (E6) and (E7) in terms of the ‘‘loop function’’ $F_\Lambda(\sigma^2)$,

$$V_0^{\text{one-loop}}(\sigma^2) \equiv V_\Lambda(\sigma^2) + F_\Lambda(\sigma^2), \quad (\text{E10})$$

with

$$F_\Lambda(\sigma^2) = F_\Lambda^{\text{MF}}(\sigma^2) + \frac{1}{64\pi^2} \left\{ 3m_\pi^4 \left[\frac{1}{l^\pi} + \ln l^\pi - \ln(1+l^\pi) \right] + m_\sigma^4 \left[\frac{1}{l^\sigma} + \ln l^\sigma - \ln(1+l^\sigma) \right] \right\}, \quad (\text{E11})$$

$$F_\Lambda^{\text{MF}}(\sigma^2) = -\frac{1}{8\pi^2} \left\{ (m^+)^4 \left[\frac{1}{l^+} + \ln l^+ - \ln(1+l^+) \right] + (m^-)^4 \left[\frac{1}{l^-} + \ln l^- - \ln(1+l^-) \right] \right\}, \quad (\text{E12})$$

we reorganize Eqs. (E8) and (E9) (with the identification $\varphi_0^2 = f_\pi^2$) as

$$\alpha_{1,\Lambda} = \frac{h}{2f_\pi} - F'_\Lambda(f_\pi^2) \equiv \frac{M_\pi^2}{2} - F'_\Lambda(f_\pi^2), \quad (\text{E13})$$

$$\alpha_{2,\Lambda} = \frac{M_\sigma^2 - M_\pi^2}{4f_\pi^2} - F''_\Lambda(f_\pi^2). \quad (\text{E14})$$

The loop function F_Λ depends on the Taylor coefficients $\alpha_{1,\Lambda}$ and $\alpha_{2,\Lambda}$ in the one-loop case, whereas it is independent of these two parameters in the MF approximation (the MF loop function F_Λ^{MF} does not involve the bosonic masses). Expanding the function F_Λ around the vacuum state,

$$F_\Lambda(\sigma^2) = F_\Lambda(f_\pi^2) + F'_\Lambda(f_\pi^2) (\sigma^2 - f_\pi^2) + \frac{1}{2} F''_\Lambda(f_\pi^2) (\sigma^2 - f_\pi^2)^2 + \dots, \quad (\text{E15})$$

one rewrites the renormalized IR potential (E10) as

$$\begin{aligned} V_0^{\text{one-loop}}(\sigma^2) &= \left[\frac{M_\pi^2}{2} - F'_\Lambda(f_\pi^2) \right] (\sigma^2 - f_\pi^2) + \frac{1}{2} \left[\frac{M_\sigma^2 - M_\pi^2}{4f_\pi^2} - F''_\Lambda(f_\pi^2) \right] (\sigma^2 - f_\pi^2)^2 \\ &+ F_\Lambda(f_\pi^2) + F'_\Lambda(f_\pi^2) (\sigma^2 - f_\pi^2) + \frac{1}{2} F''_\Lambda(f_\pi^2) (\sigma^2 - f_\pi^2)^2 + \mathcal{O}[(\sigma^2 - f_\pi^2)^3]. \end{aligned} \quad (\text{E16})$$

Thus the divergent contributions to the potential cancel out to order $(\sigma^2 - f_\pi^2)^2$. The infinite constant $F_\Lambda(f_\pi^2)$ does not affect derivatives of $V_0^{\text{one-loop}}$. Terms higher than $(\sigma^2 - f_\pi^2)^2$ likewise do not contribute to the first and second derivatives evaluated at the vacuum state, $\sigma^2 = f_\pi^2$. This means that we find from Eq. (E16) finite observables M_σ and M_π even if we would take the infinite-cutoff limit, $\Lambda \rightarrow \infty$ ($l^{\pi/\sigma} \rightarrow 0$ and $l^\pm \rightarrow 0$).

The renormalized IR potential can therefore be defined as

$$V_{\text{ren.}}^{\text{one-loop}}(\sigma^2) = \frac{M_\pi^2}{2} (\sigma^2 - f_\pi^2) + \frac{M_\sigma^2 - M_\pi^2}{8f_\pi^2} (\sigma^2 - f_\pi^2)^2. \quad (\text{E17})$$

Once we fix the physical IR values of f_π , M_π , and M_σ , we can determine at any cutoff scale the parameters α_1 and α_2 of the UV potential such that the one-loop integration generates exactly those observables in the IR. The coefficient α_1 renormalizes the ‘‘mass term’’ of the effective potential and the coefficient α_2 renormalizes the quartic interaction. We thus expect unequal sensitivity of these couplings on Λ , with α_1 being more sensitive than α_2 due to their respective mass dimensions.

We adapt the above ‘‘standard’’ renormalization formalism in the next Section in order to determine initial values of the Taylor coefficients α_1 and α_2 at the chiral-symmetry breaking scale $\Lambda_\chi \simeq 4\pi f_\pi$. We emphasize that, in general, the breaking scale Λ_χ and the actual UV cutoff Λ (as discussed above) as well as the initialization scale of the integration of momentum modes do not coincide, especially in their precise physical meaning. It is hence important to notice that the discussion below is part of the approximations of our work and the findings might contain corresponding artifacts. Being aware of this issue, we have already done numeric tests concerning the presence of higher Taylor coefficients at Λ_χ , cf. again Fig. 8. In order to justify our approximations, further quantification of numeric errors induced by using Λ_χ in place of Λ in the above formalism (as well as using Λ_χ as the initialization scale) is given below.

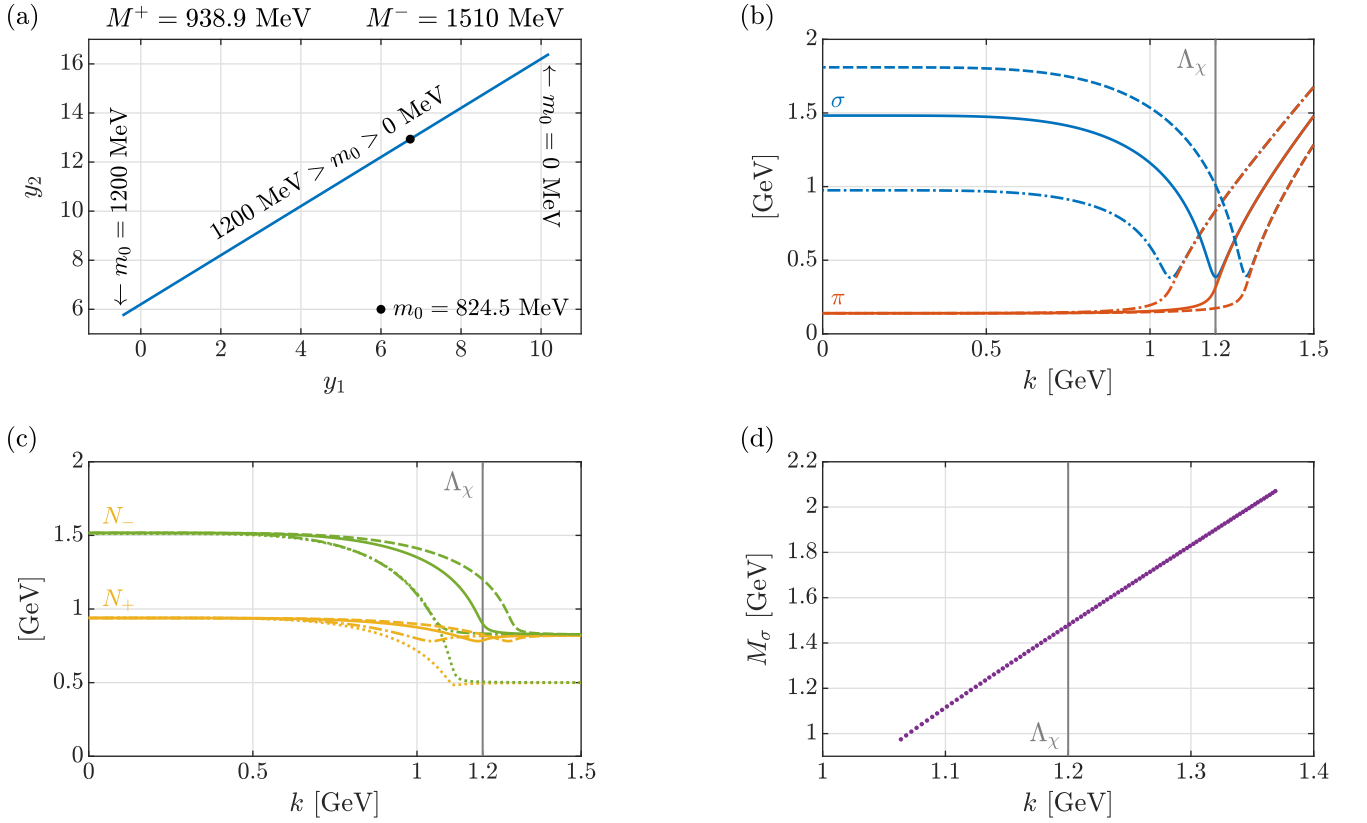


Figure 12. Prediction of the isoscalar σ -mass in the MF approximation. (a) Physical IR fermion masses are produced for various choices of the chiral-invariant mass m_0 (parametric plot of the corresponding Yukawa couplings in the range of $0 \text{ MeV} \leq m_0 \leq 1200 \text{ MeV}$); the black dot indicates the IR (renormalized) M_0 -value of the LPA'-truncation. (b) Determination of the σ -mass by adjusting the Taylor coefficient α_2 such that chiral symmetry breaking occurs at the scale Λ_χ (solid: $\alpha_2 = 38$; dashed: $\alpha_2 = 70$; dash-dotted: $\alpha_2 = 1$). (c) Scale evolution of the fermion masses corresponding to the parameter scenarios of panel (b); the IR fermion masses are fixed and the dotted lines show a scenario with varying m_0 (dotted: $m_0 = 500 \text{ MeV}$; else: $m_0 = 824.5 \text{ MeV}$). (d) Scale (k -value; x-axis) of chiral symmetry breaking as a function of the IR σ -mass (M_σ ; y-axis).

2. Isoscalar-mass prediction

In the MF approximation, Eqs. (E13) and (E14) unambiguously determine the Taylor coefficients $\alpha_{1,\Lambda}$ and $\alpha_{2,\Lambda}$ at $\Lambda = \Lambda_\chi$ as functions of the bosonic masses and the fermionic loop function (E12). While the first coefficient α_1 is set by the IR pion mass M_π , the second coefficient α_2 controls the mass splitting between the bosons. Conversely, the IR isoscalar σ -mass can be predicted after fixing all other parameters in Eq. (E14) by adjusting the coefficient α_2 in such a way that chiral symmetry breaking occurs at $\Lambda_\chi = 1.2 \text{ GeV} \simeq 4\pi f_\pi$.

In general, requiring that the isoscalar mass M_σ be larger than the pion mass M_π at the chiral breaking scale Λ_χ (and below), which is the natural ordering of the bosonic masses, implies a positive Taylor coefficient α_2 ,

$$M_\sigma^2 - M_\pi^2|_{\Lambda_\chi} = 4\sigma_0^2 \alpha_2|_{\Lambda_\chi} > 0 \quad \Leftrightarrow \quad \alpha_{2,\Lambda_\chi} > 0, \quad (\text{E18})$$

with the (scale-dependent) minimum σ_0 of the effective potential. Moreover, the coefficient α_1 must also be positive in order to fulfill the minimum condition at Λ_χ ,

$$2\sigma_0 V'_{\Lambda_\chi}(\sigma_0^2) - h = 0 \quad \Leftrightarrow \quad \alpha_{1,\Lambda_\chi} + \alpha_{2,\Lambda_\chi} (\sigma_0^2 - \varphi_0^2) - \frac{h}{2\sigma_0} = 0 \quad \Rightarrow \quad \alpha_{1,\Lambda_\chi} > 0, \quad (\text{E19})$$

where we used that the value of σ_0 increases as the scale k decreases, so that $\sigma_0^2 = f_\pi^2 \lesssim \varphi_0^2$ in the IR (cf. again Fig. 2).

The prediction of the isoscalar mass is only possible if one fixes the chiral-invariant mass parameter m_0 to a common value in all investigated approximations. This is due to the fact that the three parameters y_1 , y_2 , and m_0 are not uniquely determined by the two fermion masses (E4). The Yukawa couplings y_1 and y_2 are correlated. Figure 12(a)

demonstrates this correlation in terms of a parametric plot of the Yukawa couplings depending on the chosen value of m_0 for given physical fermion masses $m^\pm \equiv M^\pm$. As discussed in the main part of this publication, we decided to take the IR (renormalized) M_0 -value of the LPA'-truncation for this purpose ($M_0 = m_0/Z^\psi$ in the LPA', whereas $M_0 \equiv m_0$ for the other approximations), which yields approximately the same chiral-invariant mass and Yukawa couplings in the IR (along with roughly the same IR fermion masses, see Table II).

In Fig. 12(b), it is shown how we predict the isoscalar mass M_σ in the MF approximation by utilizing Eqs. (E13) and (E14). The first Taylor coefficient α_{1,Λ_χ} of the potential (E5) is obtained by fixing the pion mass in the IR to the physical value of $M_\pi \simeq 138$ MeV; this coefficient is independent of the σ -mass. The second Taylor coefficient α_{2,Λ_χ} , which regulates the isoscalar mass in the IR, is then adjusted in order to break chiral symmetry at Λ_χ (see the solid line). Figure 12(c) exhibits the scale evolution of the fermion masses corresponding to the three parameter scenarios of Fig. 12(b). The IR masses are not affected by the different choices for M_σ ; they are determined by the parameter $m_0 = 824.5$ MeV, the Yukawa couplings according to Fig. 12(a), and the physical value of the pion decay constant f_π . The additional dotted curves exemplify a change of the chiral-invariant mass (to $m_0 = 500$ MeV). In this setting, the Yukawa couplings (as functions of the parameter m_0) compensate for the change in the mass m_0 in the sense that the physical fermion masses are still attained in the IR.

The k -dependence of the isoscalar mass M_σ in Fig. 12(b) features a minimum at $k > 1$ GeV in all three cases, when chiral symmetry breaking occurs (in fact, we adjusted the parameter α_2 such that this minimum lies at $\Lambda_\chi = 1.2$ GeV, cf. once more the solid line). Figure 12(d) presents a scatter plot of the location of this minimum on the k -scale (x -axis) as a function of the IR value of M_σ (y -axis). Manifestly, the location crosses the scale Λ_χ for an IR isoscalar mass of the order of 1.5 GeV, giving the σ -mass prediction in the MF approximation ($M_\sigma = 1477$ MeV).

A more detailed analysis of the initial Taylor coefficients α_{1,Λ_χ} and α_{2,Λ_χ} of the potential (E5) is given in Fig. 13. As stated above, it is mandatory to have positive values for the two coefficients, which leads to restrictions regarding the choice of initial parameters. In Figs. 13(a) and 13(b), we illustrate the variation of α_1 with the parameters m_0 and Λ_χ , respectively. This coefficient is positive for $m_0 < 1.2$ GeV. Its value generally shrinks with increasing m_0 and decreasing Λ_χ . Concerning the coefficient α_2 , Figs. 13(c) and 13(d) reveal that, for fixed $m_0 = 824.5$ MeV, the IR σ -mass has to be larger than 1 GeV in order to find positive values. Varying the m_0 -parameter, large values of the σ -mass above 1 GeV are obviously favored as they generate more ‘‘overlap’’ with the range of $200 \text{ MeV} \lesssim m_0 \lesssim 900 \text{ MeV}$ suggested by other phenomenological studies [cf. Fig. 13(c)]. Furthermore, light isoscalar masses ($M_\sigma \sim 500$ MeV) are only reachable for $m_0 > 1.1$ GeV [cf. Fig. 13(d)]. The dependence of α_2 on Λ_χ again rules out IR isoscalar masses below 1 GeV, see Fig. 13(e). A variation of Λ_χ itself is also restricted by the condition $\alpha_2 > 0$ to a rough maximum of 1.5 GeV, given a σ -mass of the same order (and even to smaller values for decreasing M_σ). The overall sensitivity of the coefficients α_1 and α_2 on Λ_χ is estimated by the difference quotients

$$\left| \frac{\Delta\alpha_1/f_\pi^2}{\Delta\Lambda_\chi} \right| = \frac{\alpha_1(1.5 \text{ GeV}) - \alpha_1(1 \text{ GeV})}{f_\pi^2(1.5 \text{ GeV} - 1 \text{ GeV})} \simeq 0.178 \text{ MeV}^{-1}, \quad (\text{E20})$$

$$\left| \frac{\Delta\alpha_2}{\Delta\Lambda_\chi} \right| = \frac{\alpha_2(1 \text{ GeV}) - \alpha_2(1.5 \text{ GeV})}{1.5 \text{ GeV} - 1 \text{ GeV}} \simeq 0.097 \text{ MeV}^{-1}, \quad (\text{E21})$$

reflecting a larger sensitivity of the dimensionless coefficient α_1/f_π^2 w.r.t. changes in Λ_χ , as expected.

Figure 13(f) displays the effect of changing the initialization scale Λ_χ and the reference scale for the bosonic masses in the MF integration. This means that we now allow for higher cutoff scales than $\Lambda_\chi = 1.2$ GeV as the starting point for the integration of momentum modes in the UV. Moreover, we also change the IR cutoff scale k of the integration to values larger than zero ($k > 0$; this is called the ‘‘reference scale’’), at which we preset the bosonic and fermionic masses as the outcome of the MF integration (in contrast to the physical scale of $k = 0$). While the results presented in Sec. IV are produced by taking the IR limit $k = 0$ as the reference scale, i.e., with the IR bosonic masses M_π and M_σ determining the Taylor coefficients α_{1,Λ_χ} and α_{2,Λ_χ} (cf. the line named ‘‘original’’), we also investigate alternative choices for Λ_χ and the IR reference scale $k > 0$. Despite the cutoff independence of the renormalized effective potential (E17), we expect certain inaccuracies in the Taylor coefficients themselves for the reason that the current squared minimum σ_0^2 of the ‘‘flowing’’ potential $V(\sigma^2)$ deviates more and more from the squared expansion point $\varphi_0^2 \gtrsim f_\pi^2$ as the scale increases, $\sigma_0^2 \ll \varphi_0^2$. We therefore compare the ‘‘original’’ integration to cases where we determine α_1 and α_2 at scales larger than $\Lambda_\chi = 1.2$ GeV, namely, at $\Lambda_\chi = 1.25$ GeV and $\Lambda_\chi = 1.3$ GeV, using also reference scales away from zero. Being more precise, the four respective curves in Fig. 13(f) depict the MF integration for taking the scales $k = 1.2$ GeV (lines without further specification) and $k = 1$ GeV [lines with the specification ‘‘(φ'_0)’’] as the reference scale for determining the Taylor coefficients (at $\Lambda_\chi = 1.25$ GeV and $\Lambda_\chi = 1.3$ GeV), where we additionally shift the expansion point in the latter cases, $\varphi_0 \rightarrow \varphi'_0 = \sigma_0|_{k=1 \text{ GeV}}$. One observes that, for the reference scale lying at $k = 1.2$ GeV, the IR σ -mass at $k = 0$ substantially differs by about 250 MeV (cf. solid and dotted lines). This effect is again weakened by taking the reference scale of $k = 1$ GeV instead (and shifting the expansion point accordingly). Eventually, the importance of higher Taylor coefficients can be assessed by the deviations stemming from the different

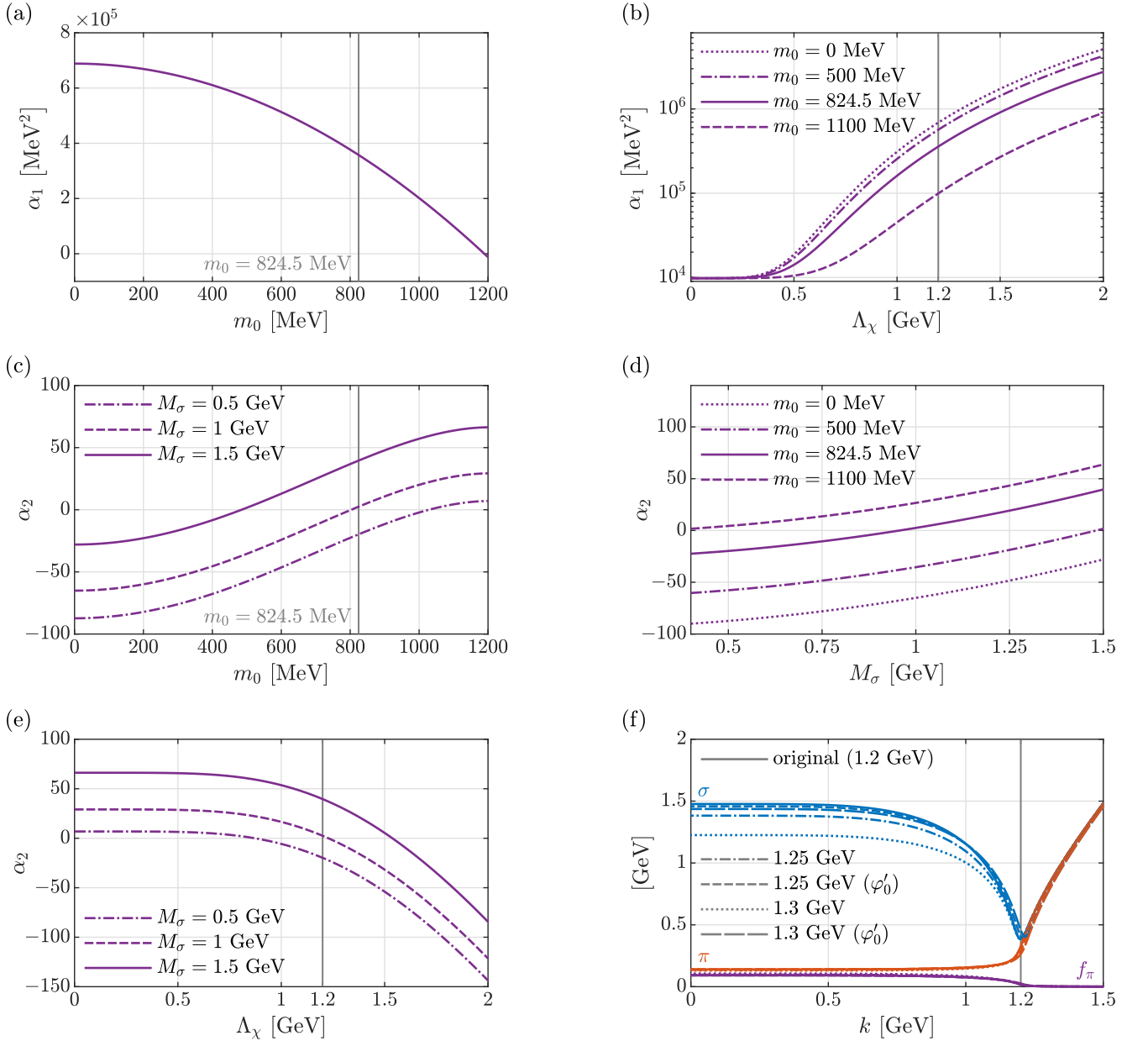


Figure 13. Analysis of the initial Taylor coefficients in the MF approximation. (a) and (b) Taylor coefficient α_1 as a function of the chiral-invariant mass m_0 and the scale Λ_χ , respectively. (c) to (e) Taylor coefficient α_2 as a function of the chiral-invariant mass m_0 , the IR isoscalar mass M_σ , as well as the scale Λ_χ , respectively. These findings rule out light IR σ -masses below 1 GeV. (f) Effect of changes in the initialization scale Λ_χ and the IR reference scale for the bosonic masses (as well as the pion decay constant) at $k = 0$ as the reference scale [described by Eqs. (E13) and (E14)]; the other curves are obtained by increasing Λ_χ to 1.25 GeV or 1.3 GeV. For each of these two scales the respective line without any further specification stands for the case of taking the bosonic masses at $k = 1.2$ GeV as the reference scale (instead of the physical IR masses at $k = 0$), whereas the lines with the specification “ (φ'_0) ” represent those with the reference scale lying at $k = 1$ GeV and an additionally shifted expansion point $\varphi_0 \rightarrow \varphi'_0$. The curves for the determination scales of 1.25 GeV or 1.3 GeV are computed using the equivalents of Eqs. (E13) and (E14) for nonzero k [for even larger determination scales of e.g. 1.4 GeV or 1.5 GeV, we already find negative values for the second coefficient α_2 , similar to panel (e)]. The results in subfigure (f) give an intuition about the accuracy of the employed Taylor approximation and the importance of higher Taylor coefficients.

Table VI. Implementation of numeric root finding in the one-loop approximation. We employ the dimensionless rescaled variables κ_1 and κ_2 (as defined in the first column). The variables κ_1 and κ_2 are sampled in equal spaces of their fourth and square root, respectively (with $\kappa_{1,\min} = \varepsilon$ and $\kappa_{1,\max} = 1$; $\kappa_{2,\min} = \varepsilon$ and $\kappa_{2,\max} = 1$; $\varepsilon = 10^{-6}$). The equations are numerically solved for isoscalar masses in the interval of $400 \text{ MeV} \leq M_\sigma \leq 1500 \text{ MeV}$ (in steps of 1 MeV; cf. Fig. 14).

Variables	Equations	Sampling intervals	Number of sampling points (equally spaced)
$\kappa_1 = \alpha_1/\Lambda_\chi^2$	Eq. (E13): $\kappa_1 - (M_\pi^2/2 - F'_{\Lambda_\chi})/\Lambda_\chi^2 = 0$	$\kappa_1^{1/4} \in [\varepsilon^{1/4}, 1]$	$N_{\kappa_1} = 100$
$\kappa_2 = \alpha_2 f_\pi^2/\Lambda_\chi^2$	Eq. (E14): $\kappa_2 - [(M_\sigma^2 - M_\pi^2)/4 - F''_{\Lambda_\chi} f_\pi^2]/\Lambda_\chi^2 = 0$	$\kappa_2^{1/2} \in [\varepsilon^{1/2}, 1]$	$N_{\kappa_2} = 100$

initialization scales of 1.25 GeV and 1.3 GeV, compare the corresponding curves (even larger initialization scales of e.g. 1.4 GeV or 1.5 GeV are not considered as the coefficient α_2 becomes negative there, signaling inaccuracies in the employed approach). In total, we understand these observed differences in the IR σ -mass mainly as consequences of neglecting the higher Taylor coefficients at the initialization scale $\Lambda_\chi = 1.2 \text{ GeV}$. Nevertheless, the MF integration apparently generates a large isoscalar mass in the IR ($M_\sigma > 1 \text{ GeV}$) and this particular feature is independent of the choice of the initialization and reference scales as studied in Fig. 13(f).

In the one-loop approximation, the Taylor coefficients α_{1,Λ_χ} and α_{2,Λ_χ} enter the right sides of Eqs. (E13) and (E14) through the loop function F_{Λ_χ} , which includes the bosonic loop contribution [the boson masses in Eqs. (E2) and (E3) depend on α_1 and α_2], i.e.,

$$\begin{aligned}
F_{\Lambda_\chi}(\sigma^2) \equiv F_{\Lambda_\chi}^{\text{MF}}(\sigma^2) + \frac{1}{16\pi^2} \left\{ 3 [\alpha_{1,\Lambda_\chi} + \alpha_{2,\Lambda_\chi} (\sigma^2 - \varphi_0^2)]^2 \left[\frac{\Lambda_\chi^2}{2 [\alpha_{1,\Lambda_\chi} + \alpha_{2,\Lambda_\chi} (\sigma^2 - \varphi_0^2)]} \right. \right. \\
+ \ln \left. \frac{2 [\alpha_{1,\Lambda_\chi} + \alpha_{2,\Lambda_\chi} (\sigma^2 - \varphi_0^2)]}{\Lambda_\chi^2 + 2 [\alpha_{1,\Lambda_\chi} + \alpha_{2,\Lambda_\chi} (\sigma^2 - \varphi_0^2)]} \right] \\
+ [\alpha_{1,\Lambda_\chi} + \alpha_{2,\Lambda_\chi} (3\sigma^2 - \varphi_0^2)]^2 \left[\frac{\Lambda_\chi^2}{2 [\alpha_{1,\Lambda_\chi} + \alpha_{2,\Lambda_\chi} (3\sigma^2 - \varphi_0^2)]} \right. \\
+ \ln \left. \frac{2 [\alpha_{1,\Lambda_\chi} + \alpha_{2,\Lambda_\chi} (3\sigma^2 - \varphi_0^2)]}{\Lambda_\chi^2 + 2 [\alpha_{1,\Lambda_\chi} + \alpha_{2,\Lambda_\chi} (3\sigma^2 - \varphi_0^2)]} \right] \left. \right\}. \quad (\text{E22})
\end{aligned}$$

In contrast, the fermion masses (E4) and the corresponding loop function in the MF approximation are independent of α_1 and α_2 . With the bosonic loop function in Eq. (E22) containing the Taylor coefficients, it is more complicated to solve Eqs. (E13) and (E14) for α_1 and α_2 . We hence formulate these equations as a root-finding problem and numerically search for solutions. The technical details of this implementation are listed in Table VI. Figure 14(a) collects the numeric roots as a function of M_σ . For a small value of $M_\sigma \sim 500 \text{ MeV}$, the roots are located in the top-left corner and tend towards a larger α_1 for growing M_σ (roughly up to $M_\sigma \sim 950 \text{ MeV}$), whereas the value of the coefficient α_2 does not change drastically. Starting from $M_\sigma \sim 950 \text{ MeV}$, we find two solutions to the system of equations, both of which are physically equivalent. This means that the two parameter sets consisting of α_1 and α_2 give the same physical outcome in the IR; they only disagree in the higher Taylor coefficients (α_n , $n > 2$), which do not affect the first and second derivatives of the effective potential at $\varphi_0^2 \simeq f_\pi^2$. Going to even higher isoscalar masses, the two distinct solutions approach each other from the top-left and the bottom-right. Above values of $M_\sigma \sim 1110 \text{ MeV}$, we no longer find numeric solutions.

Transferring these findings to the determination of the isoscalar mass M_σ by adjusting the chiral-symmetry breaking scale, we see in Fig. 14(b) that the local minimum in the M_σ -evolution (for $k > 1 \text{ GeV}$) coincides with the scale Λ_χ at $M_\sigma \simeq 1.1 \text{ GeV}$ [indicated as black dots in Fig. 14(a)]. The second solutions above $M_\sigma \simeq 950 \text{ MeV}$ add the data points in the top-left corner, exhibiting a breaking scale below Λ_χ . Contrarily, for light isoscalar masses ($M_\sigma \sim 500 \text{ MeV}$), the breaking scale is moved to larger k -values, ending up at $k \simeq 1370 \text{ MeV}$ for $M_\sigma \simeq 400 \text{ MeV}$. Figures 14(c) and 14(d) represent the case with two equivalent solutions ($M_\sigma \sim 1.1 \text{ GeV}$) and the one with a single solution ($M_\sigma \simeq 500 \text{ MeV}$), respectively. Similar to the FRG flows in Fig. 2, the M_σ -evolution in Fig. 14(d) shows a “down-bending,” but the actual chiral breaking scale does not match the requested value of Λ_χ . In summary, the large σ -masses in the MF and one-loop approximations result from insisting on chiral symmetry breaking occurring at $\Lambda_\chi = 1.2 \text{ GeV} \simeq 4\pi f_\pi$ and vice versa.

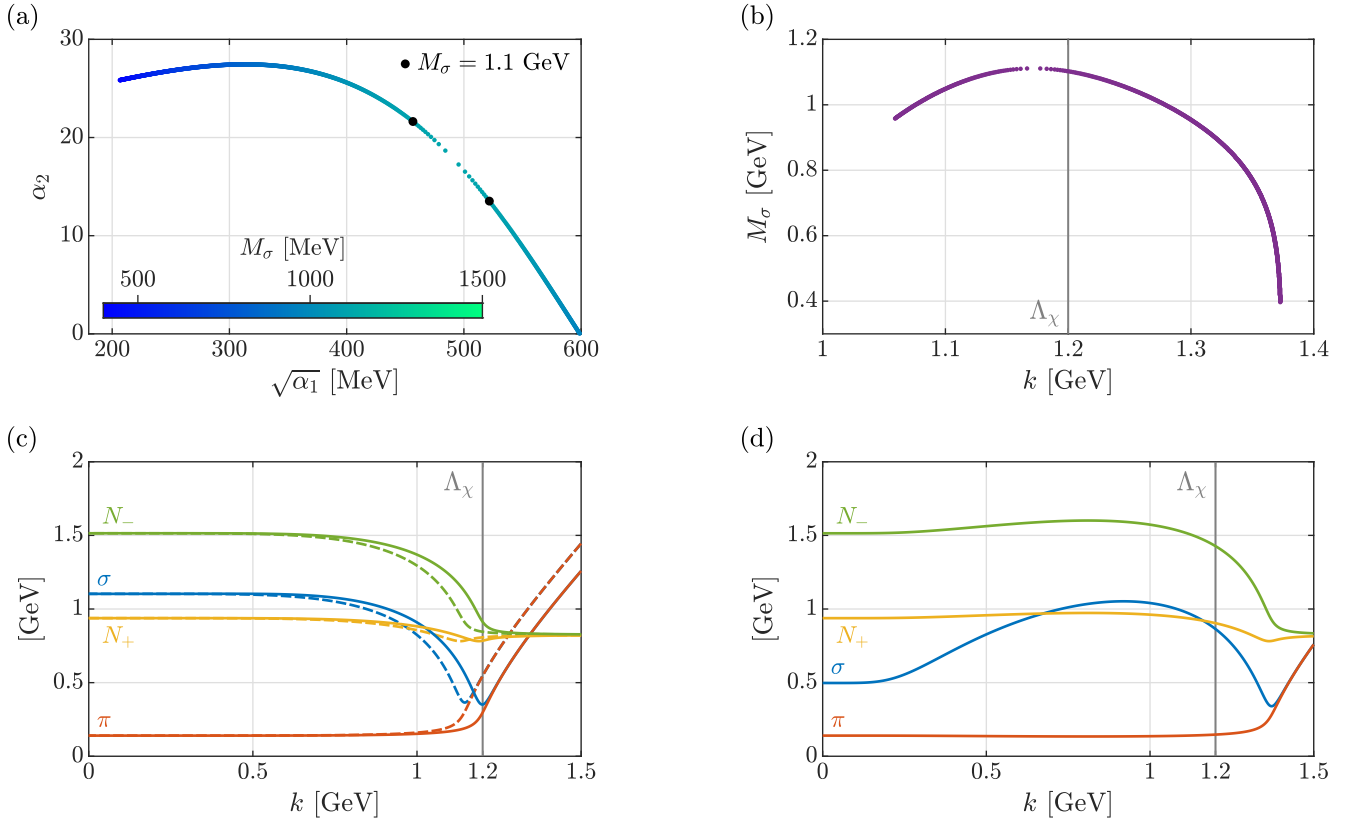


Figure 14. One-loop integration and determination of the initial Taylor coefficients. (a) Numeric roots of Eqs. (E13) and (E14) as functions of the IR isoscalar mass M_σ within the one-loop approximation (rescaled to $\sqrt{\alpha_1}$ and α_2); the color code covers the range of $400 \text{ MeV} \leq M_\sigma \leq 1500 \text{ MeV}$ and the black dots indicate the two solutions found for $M_\sigma = 1.1 \text{ GeV}$. (b) Numeric determination of the isoscalar mass M_σ as a function of the k -value of the chiral-symmetry breaking scale. (c) and (d) Cases of two/one solution(s) to Eqs. (E13) and (E14) for a given value of the σ -mass [(c) $M_\sigma = 1103 \text{ MeV}$; (d) $M_\sigma = 498 \text{ MeV}$].

Appendix F: Higher-derivative pion self-interactions

The elimination of the θ -field by the EOM (32) generates various higher-derivative pion self-interactions. Additionally to Eq. (57), one finds 13 (possible) structures at $\mathcal{O}(p^4)$,

$$\begin{aligned}
\mathcal{O}(p^4): \quad & \Pi^2 \Pi \cdot \square^2 \Pi, \quad \Pi^2 (\partial_\mu \Pi) \cdot \partial^\mu \square \Pi, \quad \Pi^2 (\square \Pi)^2, \quad \Pi^2 (\partial_\mu \partial_\nu \Pi)^2, \quad \Pi \cdot (\partial_\mu \Pi) \Pi \cdot \partial^\mu \square \Pi, \\
& \Pi \cdot (\partial_\mu \Pi) (\partial^\mu \Pi) \cdot \square \Pi, \quad \Pi \cdot (\partial_\mu \Pi) (\partial_\nu \Pi) \cdot \partial_\mu \partial_\nu \Pi, \quad (\Pi \cdot \square \Pi)^2, \quad \Pi \cdot (\square \Pi) (\partial_\mu \Pi)^2, \\
& (\Pi \cdot \partial_\mu \partial_\nu \Pi)^2, \quad \Pi \cdot (\partial_\mu \partial_\nu \Pi) (\partial_\mu \Pi) \cdot (\partial_\nu \Pi), \quad [(\partial_\mu \Pi) \cdot \partial^\mu \Pi]^2, \quad [(\partial_\mu \Pi) \cdot \partial_\nu \Pi]^2, \quad (F1)
\end{aligned}$$

as well as 54, 221, and 883 possibilities at $\mathcal{O}(p^6)$, $\mathcal{O}(p^8)$, and $\mathcal{O}(p^{10})$, respectively [due to the large numbers, we do not list the structures of $\mathcal{O}(p^6)$ and higher]. As already advertised in Sec. III, we obtain 3335 possibilities at $\mathcal{O}(p^{12})$, where we finally stopped the expansion in the pion momentum p . In order to keep track of the large amount of terms, we employed again the powerful algebra tool `FeynCalc` [109].

The pion self-interactions of the effective action Γ_{sol} , listed in Eqs. (57) and (F1), are parametrized by the (nonzero) low-energy couplings

$$\mathcal{O}(p^0): \quad \mathfrak{c}_1 = \frac{M_\pi^2(\epsilon + 1)}{8f_\pi^2}, \quad (F2)$$

$$\mathcal{O}(p^2): \quad \mathfrak{c}_2 = -\frac{2\epsilon + 1}{4f_\pi^2}, \quad \mathfrak{c}_3 = \frac{\epsilon^2}{2f_\pi^2}, \quad (F3)$$

$$\mathcal{O}(p^4): \quad \mathfrak{c}_5 \equiv \mathfrak{c}_6 \equiv \mathfrak{c}_9 = -\frac{\epsilon^3}{f_\pi^2 M_\pi^2}, \quad \mathfrak{c}_7 = -\frac{2\epsilon^2(\epsilon + 1)}{f_\pi^2 M_\pi^2}, \quad \mathfrak{c}_8 = -\frac{\epsilon^3}{2f_\pi^2 M_\pi^2}, \quad \mathfrak{c}_{12} = \frac{\epsilon(1 - \epsilon^2)}{2f_\pi^2 M_\pi^2}, \quad (F4)$$

⋮

where the indices of the couplings refer to the respective sortings of the structures in Eqs. (57) and (F1). Hence, only a specific coordinate-dependent subset of all possibilities is generated.¹⁷ Again, we do not give the numerous couplings of $\mathcal{O}(p^6)$ and higher—the overall strategy remains the same for all p -orders. The corresponding contributions to the scattering lengths read

$$\begin{aligned}
\mathcal{O}(p^0): \quad \Delta_0 a_0^0 &= \frac{5}{4\pi} \mathfrak{C}_1, & \Delta_0 a_0^2 &= \frac{1}{2\pi} \mathfrak{C}_1, \\
\mathcal{O}(p^2): \quad \Delta_2 a_0^0 &= -\frac{M_\pi^2}{4\pi} (\mathfrak{C}_2 - 3\mathfrak{C}_3), & \Delta_2 a_0^2 &= \frac{M_\pi^2}{2\pi} \mathfrak{C}_2, \\
\mathcal{O}(p^4): \quad \Delta_4 a_0^0 &= \frac{M_\pi^4}{4\pi} [5(\mathfrak{C}_8 + \mathfrak{C}_{12}) + \mathfrak{C}_9 - 3(\mathfrak{C}_5 + \mathfrak{C}_6 + \mathfrak{C}_7)], & \Delta_4 a_0^2 &= \frac{M_\pi^4}{2\pi} (\mathfrak{C}_8 - \mathfrak{C}_9 + \mathfrak{C}_{12}),
\end{aligned} \tag{F5}$$

such that

$$a_0^0 = \sum_{i \text{ even}} \Delta_i a_0^0 = \frac{M_\pi^2}{32\pi f_\pi^2} (7 + 29\epsilon + 60\epsilon^2 + 48\epsilon^3) + \dots, \tag{F6}$$

$$a_0^2 = \sum_{i \text{ even}} \Delta_i a_0^2 = -\frac{M_\pi^2}{16\pi f_\pi^2} (1 - \epsilon). \tag{F7}$$

These are the $\mathcal{O}(\epsilon)$ -accurate scattering lengths, cf. Eqs. (46) and (47). In the limit $M_\sigma \rightarrow \infty$ ($\epsilon \rightarrow 0$ for nonzero and finite M_π), we have

$$\mathcal{O}(p^0): \quad \lim_{\epsilon \rightarrow 0} \mathfrak{C}_1 = \frac{M_\pi^2}{8f_\pi^2} \equiv \frac{\tilde{h}}{8f_\pi^3}, \quad \mathcal{O}(p^2): \quad \lim_{\epsilon \rightarrow 0} \mathfrak{C}_2 = -\frac{1}{4f_\pi^2}, \tag{F8}$$

which are the unique low-energy couplings of the NLSM (with explicit chiral symmetry breaking) up to $\mathcal{O}(\Pi^4, \partial^2)$ in stereographic pions, see once more Eqs. (22) to (24).

-
- [1] W. Heisenberg, *Z. Phys.* **77**, 1 (1932).
 - [2] E. Wigner, *Phys. Rev.* **51**, 106 (1937).
 - [3] P. A. Zyla *et al.* (Particle Data Group), *PTEP* **2020**, 083C01 (2020).
 - [4] J. S. Schwinger, *Annals Phys.* **2**, 407 (1957).
 - [5] M. Gell-Mann and M. Levy, *Nuovo Cim.* **16**, 705 (1960).
 - [6] S. Weinberg, *Phys. Rev. Lett.* **18**, 188 (1967).
 - [7] F. Gursey, *Nuovo Cim.* **16**, 230 (1960).
 - [8] J. S. Schwinger, *Phys. Lett. B* **24**, 473 (1967).
 - [9] S. Weinberg, *Phys. Rev.* **166**, 1568 (1968).
 - [10] J. Zinn-Justin, *Int. Ser. Monogr. Phys.* **92**, 1 (1996).
 - [11] J. Gasser and H. Leutwyler, *Annals Phys.* **158**, 142 (1984).
 - [12] J. Gasser and H. Leutwyler, *Nucl. Phys. B* **250**, 465 (1985).
 - [13] H. Leutwyler, *Annals Phys.* **235**, 165 (1994), arXiv:hep-ph/9311274.
 - [14] S. Scherer, *Adv. Nucl. Phys.* **27**, 277 (2003), arXiv:hep-ph/0210398.
 - [15] J. Bijnens, *Prog. Part. Nucl. Phys.* **58**, 521 (2007), arXiv:hep-ph/0604043.
 - [16] H. Leutwyler, *Scholarpedia* **7**, (10):8708 (2012).
 - [17] S. R. Coleman, J. Wess, and B. Zumino, *Phys. Rev.* **177**, 2239 (1969).
 - [18] C. G. Callan, Jr., S. R. Coleman, J. Wess, and B. Zumino, *Phys. Rev.* **177**, 2247 (1969).
 - [19] K. Meetz, *J. Math. Phys.* **10**, 589 (1969).
 - [20] C. J. Isham, *Nuovo Cim. A* **59**, 356 (1969).
 - [21] M. Peczkis, *Rept. Math. Phys.* **11**, 211 (1977).
 - [22] C. Wetterich, *Phys. Lett. B* **301**, 90 (1993), arXiv:1710.05815 [hep-th].

¹⁷ The generated subset of term structures can considerably be reduced by means of partial-integration identities [38, 40], which however is irrelevant for the analytic and numeric results for the scattering lengths.

- [23] U. Ellwanger, *Z. Phys. C* **62**, 503 (1994), arXiv:hep-ph/9308260.
- [24] T. R. Morris, *Int. J. Mod. Phys. A* **9**, 2411 (1994), arXiv:hep-ph/9308265.
- [25] J. M. Pawłowski, *Annals Phys.* **322**, 2831 (2007), arXiv:hep-th/0512261.
- [26] D. Parganlija, F. Giacosa, and D. H. Rischke, *Phys. Rev. D* **82**, 054024 (2010), arXiv:1003.4934 [hep-ph].
- [27] D. Parganlija, P. Kovacs, G. Wolf, F. Giacosa, and D. H. Rischke, *Phys. Rev. D* **87**, 014011 (2013), arXiv:1208.0585 [hep-ph].
- [28] F. Divotgey, P. Kovacs, F. Giacosa, and D. H. Rischke, *Eur. Phys. J. A* **54**, 5 (2018), arXiv:1605.05154 [hep-ph].
- [29] P. Lakaschus, J. L. P. Mauldin, F. Giacosa, and D. H. Rischke, *Phys. Rev. C* **99**, 045203 (2019), arXiv:1807.03735 [hep-ph].
- [30] D. Bessis and J. Zinn-Justin, *Phys. Rev. D* **5**, 1313 (1972).
- [31] K. S. Jhung and R. S. Willey, *Phys. Rev. D* **9**, 3132 (1974).
- [32] T. Appelquist and C. W. Bernard, *Phys. Rev. D* **23**, 425 (1981).
- [33] W. Bentz, C. Matulla, and H. Baier, *Phys. Rev. C* **56**, 2280 (1997).
- [34] E. Brezin and J. Zinn-Justin, *Phys. Rev. Lett.* **36**, 691 (1976).
- [35] E. Brezin, J. Zinn-Justin, and J. C. Le Guillou, *Phys. Rev. D* **14**, 2615 (1976).
- [36] E. Brezin and J. Zinn-Justin, *Phys. Rev. B* **14**, 3110 (1976).
- [37] J. Eser, F. Divotgey, M. Mitter, and D. H. Rischke, *Phys. Rev. D* **98**, 014024 (2018), arXiv:1804.01787 [hep-ph].
- [38] F. Divotgey, J. Eser, and M. Mitter, *Phys. Rev. D* **99**, 054023 (2019), arXiv:1901.02472 [hep-ph].
- [39] J. Eser, F. Divotgey, and M. Mitter, *PoS CD2018*, 060 (2019), arXiv:1902.04804 [hep-ph].
- [40] J. Eser, *Momentum-dependent pion self-interactions from quantum fluctuations*, Dissertation, Johann Wolfgang Goethe-Universität Frankfurt am Main (2020).
- [41] F. Divotgey, *Niederenergiestudien effektiver Modelle stark wechselwirkender Systeme*, Dissertation, Johann Wolfgang Goethe-Universität Frankfurt am Main (2020).
- [42] N. Cichutek, F. Divotgey, and J. Eser, *Phys. Rev. D* **102**, 034030 (2020), arXiv:2006.12473 [hep-ph].
- [43] K. G. Wilson, *Phys. Rev. B* **4**, 3174 (1971); *Phys. Rev. B* **4**, 3184 (1971).
- [44] N. Dupuis, L. Canet, A. Eichhorn, W. Metzner, J. M. Pawłowski, M. Tissier, and N. Wschebor, *Phys. Rept.* **910**, 1 (2021), arXiv:2006.04853 [cond-mat.stat-mech].
- [45] U. Ellwanger and C. Wetterich, *Nucl. Phys. B* **423**, 137 (1994), arXiv:hep-ph/9402221; H. Gies and C. Wetterich, *Phys. Rev. D* **65**, 065001 (2002), arXiv:hep-th/0107221; *Phys. Rev. D* **69**, 025001 (2004), arXiv:hep-th/0209183; S. Floerchinger and C. Wetterich, *Phys. Lett. B* **680**, 371 (2009), arXiv:0905.0915 [hep-th]; M. Mitter, J. M. Pawłowski, and N. Strodthoff, *Phys. Rev. D* **91**, 054035 (2015), arXiv:1411.7978 [hep-ph]; J. Braun, L. Fister, J. M. Pawłowski, and F. Rennecke, *Phys. Rev. D* **94**, 034016 (2016), arXiv:1412.1045 [hep-ph]; A. K. Cyrol, M. Mitter, J. M. Pawłowski, and N. Strodthoff, *Phys. Rev. D* **97**, 054006 (2018), arXiv:1706.06326 [hep-ph]; R. Alkofer, A. Maas, W. A. Mian, M. Mitter, J. París-López, J. M. Pawłowski, and N. Wink, *Phys. Rev. D* **99**, 054029 (2019), arXiv:1810.07955 [hep-ph]; W.-j. Fu, J. M. Pawłowski, and F. Rennecke, *Phys. Rev. D* **101**, 054032 (2020), arXiv:1909.02991 [hep-ph].
- [46] D. U. Jungnickel and C. Wetterich, *Eur. Phys. J. C* **2**, 557 (1998), arXiv:hep-ph/9704345.
- [47] L. Jendges, B. Klein, H.-J. Pirner, and K. Schwenzer, (2006), arXiv:hep-ph/0608056.
- [48] A. Codello, R. Percacci, L. Rachwał, and A. Tonerò, *Eur. Phys. J. C* **76**, 226 (2016), arXiv:1505.03119 [hep-th].
- [49] A. Codello and R. Percacci, *Phys. Lett. B* **672**, 280 (2009), arXiv:0810.0715 [hep-th].
- [50] M. Fabbrichesi, R. Percacci, A. Tonerò, and O. Zanusso, *Phys. Rev. D* **83**, 025016 (2011), arXiv:1010.0912 [hep-ph].
- [51] F. Bazzocchi, M. Fabbrichesi, R. Percacci, A. Tonerò, and L. Vecchi, *Phys. Lett. B* **705**, 388 (2011), arXiv:1105.1968 [hep-ph].
- [52] R. Flore, A. Wipf, and O. Zanusso, *Phys. Rev. D* **87**, 065019 (2013), arXiv:1207.4499 [hep-th].
- [53] R. Percacci and M. Safari, *Phys. Rev. D* **88**, 085007 (2013), arXiv:1306.3918 [hep-th].
- [54] J. Braun, *Phys. Rev. D* **81**, 016008 (2010), arXiv:0908.1543 [hep-ph]; *J. Phys. G* **39**, 033001 (2012), arXiv:1108.4449 [hep-ph]; F. Rennecke, *Phys. Rev. D* **92**, 076012 (2015), arXiv:1504.03585 [hep-ph]; J. Braun, M. Leonhardt, and M. Pospiech, *Phys. Rev. D* **96**, 076003 (2017), arXiv:1705.00074 [hep-ph]; *Phys. Rev. D* **97**, 076010 (2018), arXiv:1801.08338 [hep-ph]; *Phys. Rev. D* **101**, 036004 (2020), arXiv:1909.06298 [hep-ph]; J. Braun, M. Leonhardt, and J. M. Pawłowski, *SciPost Phys.* **6**, 056 (2019), arXiv:1806.04432 [hep-ph]; C. Jung and L. von Smekal, *Phys. Rev. D* **100**, 116009 (2019), arXiv:1909.13712 [hep-ph].
- [55] D. U. Jungnickel and C. Wetterich, *Phys. Rev. D* **53**, 5142 (1996), arXiv:hep-ph/9505267; J. Berges, D. U. Jungnickel, and C. Wetterich, *Phys. Rev. D* **59**, 034010 (1999), arXiv:hep-ph/9705474; J. Berges, D.-U. Jungnickel, and C. Wetterich, *Eur. Phys. J. C* **13**, 323 (2000), arXiv:hep-ph/9811347; B.-J. Schaefer and J. Wambach, *Nucl. Phys. A* **757**, 479 (2005), arXiv:nucl-th/0403039; *Phys. Part. Nucl.* **39**, 1025 (2008), arXiv:hep-ph/0611191; T. K. Herbst, J. M. Pawłowski, and B.-J. Schaefer, *Phys. Lett. B* **696**, 58 (2011), arXiv:1008.0081 [hep-ph]; T. K. Herbst, M. Mitter, J. M. Pawłowski, B.-J. Schaefer, and R. Stiele, *Phys. Lett. B* **731**, 248 (2014), arXiv:1308.3621 [hep-ph]; M. Mitter and B.-J. Schaefer, *Phys. Rev. D* **89**, 054027 (2014), arXiv:1308.3176 [hep-ph]; J. M. Pawłowski and F. Rennecke, *Phys. Rev. D* **90**, 076002 (2014), arXiv:1403.1179 [hep-ph]; J. Eser, M. Grahl, and D. H. Rischke, *Phys. Rev. D* **92**, 096008 (2015), arXiv:1508.06928 [hep-ph]; C. Jung, F. Rennecke, R.-A. Tripolt, L. von Smekal, and J. Wambach, *Phys. Rev. D* **95**, 036020 (2017), arXiv:1610.08754 [hep-ph]; F. Rennecke and B.-J. Schaefer, *Phys. Rev. D* **96**, 016009 (2017), arXiv:1610.08748 [hep-ph]; W.-j. Fu, J. M. Pawłowski, F. Rennecke, and B.-J. Schaefer, *Phys. Rev. D* **94**, 116020 (2016), arXiv:1608.04302 [hep-ph]; R.-A. Tripolt, B.-J. Schaefer, L. von Smekal, and J. Wambach, *Phys. Rev. D* **97**, 034022 (2018), arXiv:1709.05991 [hep-ph]; S. Resch, F. Rennecke, and B.-J. Schaefer, *Phys. Rev. D* **99**, 076005 (2019), arXiv:1712.07961 [hep-ph]; K. Otto, M. Oertel, and B.-J. Schaefer, *Phys. Rev. D* **101**, 103021 (2020), arXiv:1910.11929 [hep-ph]; *Eur. Phys. J. ST* **229**, 3629 (2020),

- arXiv:2007.07394 [hep-ph]; C. Jung, J.-H. Otto, R.-A. Tripolt, and L. von Smekal, (2021), arXiv:2107.10748 [hep-ph].
- [56] C. E. Detar and T. Kunihiro, *Phys. Rev. D* **39**, 2805 (1989).
- [57] T. Hatsuda and M. Prakash, *Phys. Lett. B* **224**, 11 (1989).
- [58] D. Jido, Y. Nemoto, M. Oka, and A. Hosaka, *Nucl. Phys. A* **671**, 471 (2000), arXiv:hep-ph/9805306.
- [59] D. Jido, M. Oka, and A. Hosaka, *Prog. Theor. Phys.* **106**, 873 (2001), arXiv:hep-ph/0110005.
- [60] M. A. Shifman, A. I. Vainshtein, and V. I. Zakharov, *Phys. Lett. B* **78**, 443 (1978).
- [61] X.-D. Ji, *Phys. Rev. Lett.* **74**, 1071 (1995), arXiv:hep-ph/9410274.
- [62] Y.-B. Yang, A. Alexandru, T. Draper, J. Liang, and K.-F. Liu (xQCD), *Phys. Rev. D* **94**, 054503 (2016), arXiv:1511.09089 [hep-lat].
- [63] Y.-B. Yang, J. Liang, Y.-J. Bi, Y. Chen, T. Draper, K.-F. Liu, and Z. Liu, *Phys. Rev. Lett.* **121**, 212001 (2018), arXiv:1808.08677 [hep-lat].
- [64] J. D. Walecka, *Annals Phys.* **83**, 491 (1974).
- [65] T. D. Lee and G. C. Wick, *Phys. Rev. D* **9**, 2291 (1974).
- [66] J. Weyrich, N. Strodthoff, and L. von Smekal, *Phys. Rev. C* **92**, 015214 (2015), arXiv:1504.02697 [nucl-th].
- [67] R.-A. Tripolt, C. Jung, L. von Smekal, and J. Wambach, (2021), arXiv:2105.00861 [hep-ph].
- [68] S. Gallas, F. Giacosa, and D. H. Rischke, *Phys. Rev. D* **82**, 014004 (2010), arXiv:0907.5084 [hep-ph].
- [69] Y. Nemoto, D. Jido, M. Oka, and A. Hosaka, *Phys. Rev. D* **57**, 4124 (1998), arXiv:hep-ph/9710445; A. Bramon, R. Escribano, and J. L. Lucio Martinez, *Phys. Rev. D* **69**, 074008 (2004), arXiv:hep-ph/0312338; D. Zschesche, L. Tolos, J. Schaffner-Bielich, and R. D. Pisarski, *Phys. Rev. C* **75**, 055202 (2007), arXiv:nucl-th/0608044; S. Wilms, F. Giacosa, and D. H. Rischke, *Int. J. Mod. Phys. E* **16**, 2388 (2007), arXiv:nucl-th/0702076; V. Dexheimer, S. Schramm, and D. Zschesche, *Phys. Rev. C* **77**, 025803 (2008), arXiv:0710.4192 [nucl-th]; V. Dexheimer, G. Pagliara, L. Tolos, J. Schaffner-Bielich, and S. Schramm, *Eur. Phys. J. A* **38**, 105 (2008), arXiv:0805.3301 [nucl-th]; R. S. Hayano and T. Hatsuda, *Rev. Mod. Phys.* **82**, 2949 (2010), arXiv:0812.1702 [nucl-ex]; C. Sasaki and I. Mishustin, *Phys. Rev. C* **82**, 035204 (2010), arXiv:1005.4811 [hep-ph]; C. Sasaki, H. K. Lee, W.-G. Paeng, and M. Rho, *Phys. Rev. D* **84**, 034011 (2011), arXiv:1103.0184 [hep-ph]; F. Giacosa, *Prog. Part. Nucl. Phys.* **67**, 332 (2012), arXiv:1111.4944 [hep-ph]; S. Gallas, F. Giacosa, and G. Pagliara, *Nucl. Phys. A* **872**, 13 (2011), arXiv:1105.5003 [hep-ph]; J. Steinheimer, S. Schramm, and H. Stoecker, *Phys. Rev. C* **84**, 045208 (2011), arXiv:1108.2596 [hep-ph]; W.-G. Paeng, H. K. Lee, M. Rho, and C. Sasaki, *Phys. Rev. D* **85**, 054022 (2012), arXiv:1109.5431 [hep-ph]; V. Dexheimer, J. Steinheimer, R. Negreiros, and S. Schramm, *Phys. Rev. C* **87**, 015804 (2013), arXiv:1206.3086 [astro-ph.HE]; S. Gallas and F. Giacosa, *Int. J. Mod. Phys. A* **29**, 1450098 (2014), arXiv:1308.4817 [hep-ph]; A. Heinz, F. Giacosa, and D. H. Rischke, *Nucl. Phys. A* **933**, 34 (2015), arXiv:1312.3244 [nucl-th]; W.-G. Paeng, H. K. Lee, M. Rho, and C. Sasaki, *Phys. Rev. D* **88**, 105019 (2013), arXiv:1303.2898 [nucl-th]; S. Benic, I. Mishustin, and C. Sasaki, *Phys. Rev. D* **91**, 125034 (2015), arXiv:1502.05969 [hep-ph]; Y. Motohiro, Y. Kim, and M. Harada, *Phys. Rev. C* **92**, 025201 (2015), [Erratum: *Phys.Rev.C* 95, 059903 (2017)], arXiv:1505.00988 [nucl-th]; L. Olbrich, M. Zétényi, F. Giacosa, and D. H. Rischke, *Phys. Rev. D* **93**, 034021 (2016), arXiv:1511.05035 [hep-ph]; A. Mukherjee, J. Steinheimer, and S. Schramm, *Phys. Rev. C* **96**, 025205 (2017), arXiv:1611.10144 [nucl-th]; A. Mukherjee, S. Schramm, J. Steinheimer, and V. Dexheimer, *Astron. Astrophys.* **608**, A110 (2017), arXiv:1706.09191 [nucl-th]; D. Suenaga, *Phys. Rev. C* **97**, 045203 (2018), arXiv:1704.03630 [nucl-th]; Y. Takeda, Y. Kim, and M. Harada, *Phys. Rev. C* **97**, 065202 (2018), arXiv:1704.04357 [nucl-th]; W.-G. Paeng, T. T. S. Kuo, H. K. Lee, Y.-L. Ma, and M. Rho, *Phys. Rev. D* **96**, 014031 (2017), arXiv:1704.02775 [nucl-th]; M. Marczenko and C. Sasaki, *Phys. Rev. D* **97**, 036011 (2018), arXiv:1711.05521 [hep-ph]; C. Sasaki, *Nucl. Phys. A* **970**, 388 (2018), arXiv:1707.05081 [hep-ph]; M. Marczenko, D. Blaschke, K. Redlich, and C. Sasaki, *Phys. Rev. D* **98**, 103021 (2018), arXiv:1805.06886 [nucl-th]; Y. Takeda, H. Abuki, and M. Harada, *Phys. Rev. D* **97**, 094032 (2018), arXiv:1803.06779 [hep-ph]; T. Yamazaki and M. Harada, *Phys. Rev. D* **99**, 034012 (2019), arXiv:1809.02359 [hep-ph]; *Phys. Rev. C* **100**, 025205 (2019), arXiv:1901.02167 [nucl-th]; M. Marczenko, D. Blaschke, K. Redlich, and C. Sasaki, *Universe* **5**, 180 (2019), arXiv:1905.04974 [nucl-th]; D. Suenaga and P. Lakaschus, *Phys. Rev. C* **101**, 035209 (2020), arXiv:1908.10509 [nucl-th]; M. Marczenko, D. Blaschke, K. Redlich, and C. Sasaki, *Astron. Astrophys.* **643**, A82 (2020), arXiv:2004.09566 [astro-ph.HE]; T. Minamikawa, T. Kojo, and M. Harada, *Phys. Rev. C* **103**, 045205 (2021), arXiv:2011.13684 [nucl-th]; M. Marczenko, K. Redlich, and C. Sasaki, *Phys. Rev. D* **103**, 054035 (2021), arXiv:2012.15535 [hep-ph]; T. Minamikawa, T. Kojo, and M. Harada, (2021), arXiv:2107.14545 [nucl-th].
- [70] L. Y. Glozman, C. B. Lang, and M. Schrock, *Phys. Rev. D* **86**, 014507 (2012), arXiv:1205.4887 [hep-lat]; G. Aarts, C. Allton, S. Hands, B. Jäger, C. Praki, and J.-I. Skullerud, *Phys. Rev. D* **92**, 014503 (2015), arXiv:1502.03603 [hep-lat]; G. Aarts, C. Allton, D. De Boni, S. Hands, B. Jäger, C. Praki, and J.-I. Skullerud, *JHEP* **06**, 034 (2017), arXiv:1703.09246 [hep-lat].
- [71] J. Berges, D. U. Jungnickel, and C. Wetterich, *Int. J. Mod. Phys. A* **18**, 3189 (2003), arXiv:hep-ph/9811387; S. Floerchinger and C. Wetterich, *Nucl. Phys. A* **890-891**, 11 (2012), arXiv:1202.1671 [nucl-th]; M. Drews, T. Hell, B. Klein, and W. Weise, *Phys. Rev. D* **88**, 096011 (2013), arXiv:1308.5596 [hep-ph]; M. Drews and W. Weise, *Phys. Lett. B* **738**, 187 (2014), arXiv:1404.0882 [nucl-th]; *Phys. Rev. C* **91**, 035802 (2015), arXiv:1412.7655 [nucl-th]; *Prog. Part. Nucl. Phys.* **93**, 69 (2017), arXiv:1610.07568 [nucl-th]; G. Fejős and A. Hosaka, *Phys. Rev. D* **95**, 116011 (2017), arXiv:1701.03717 [hep-ph]; G. Fejos and A. Hosaka, *Phys. Rev. D* **98**, 036009 (2018), arXiv:1805.08713 [nucl-th]; W. Weise, *Int. J. Mod. Phys. E* **27**, 1840004 (2018), arXiv:1811.09682 [nucl-th]; M. Leonhardt, M. Pospiech, B. Schallmo, J. Braun, C. Drischler, K. Hebeler, and A. Schwenk, *Phys. Rev. Lett.* **125**, 142502 (2020), arXiv:1907.05814 [nucl-th]; B. Friman and W. Weise, *Phys. Rev. C* **100**, 065807 (2019), arXiv:1908.09722 [nucl-th]; L. Brandes, N. Kaiser, and W. Weise, *Eur. Phys. J. A* **57**, 243 (2021), arXiv:2103.06096 [nucl-th].
- [72] Y. Nambu, *Phys. Rev. Lett.* **4**, 380 (1960).

- [73] J. Goldstone, *Nuovo Cim.* **19**, 154 (1961).
- [74] J. Goldstone, A. Salam, and S. Weinberg, *Phys. Rev.* **127**, 965 (1962).
- [75] J. Bijnens and G. Ecker, *Ann. Rev. Nucl. Part. Sci.* **64**, 149 (2014), arXiv:1405.6488 [hep-ph].
- [76] A. Manohar and H. Georgi, *Nucl. Phys. B* **234**, 189 (1984).
- [77] S. Weinberg, *Phys. Rev. Lett.* **17**, 616 (1966).
- [78] J. Bijnens, G. Colangelo, G. Ecker, J. Gasser, and M. E. Sainio, *Phys. Lett. B* **374**, 210 (1996), arXiv:hep-ph/9511397.
- [79] J. Bijnens, G. Colangelo, G. Ecker, J. Gasser, and M. E. Sainio, *Nucl. Phys. B* **508**, 263 (1997), [Erratum: *Nucl.Phys.B* **517**, 639–639 (1998)], arXiv:hep-ph/9707291.
- [80] B. Ananthanarayan, G. Colangelo, J. Gasser, and H. Leutwyler, *Phys. Rept.* **353**, 207 (2001), arXiv:hep-ph/0005297.
- [81] G. Colangelo, J. Gasser, and H. Leutwyler, *Phys. Lett. B* **488**, 261 (2000), arXiv:hep-ph/0007112.
- [82] G. Colangelo, J. Gasser, and H. Leutwyler, *Nucl. Phys. B* **603**, 125 (2001), arXiv:hep-ph/0103088.
- [83] W. Greiner and B. Muller, *Theoretical physics. Vol. 2: Quantum mechanics. Symmetries* (1989).
- [84] V. Koch, *Int. J. Mod. Phys. E* **6**, 203 (1997), arXiv:nucl-th/9706075.
- [85] F. Sannino and J. Schechter, *Phys. Rev. D* **52**, 96 (1995), arXiv:hep-ph/9501417; M. Harada, F. Sannino, and J. Schechter, *Phys. Rev. D* **54**, 1991 (1996), arXiv:hep-ph/9511335; M. D. Scadron, *Mod. Phys. Lett. A* **14**, 1349 (1999), arXiv:hep-ph/9910243; J. L. Lucio, M. Napsuciale, and M. Ruiz-Altaba, (1999), arXiv:hep-ph/9903420; D. Black, A. H. Fariborz, S. Moussa, S. Nasri, and J. Schechter, *Phys. Rev. D* **64**, 014031 (2001), arXiv:hep-ph/0012278; M. D. Scadron, F. Kleefeld, and G. Rupp, (2006), arXiv:hep-ph/0601196; A. H. Fariborz, R. Jora, and J. Schechter, *Phys. Rev. D* **76**, 114001 (2007), arXiv:0708.3402 [hep-ph].
- [86] G. Kramer, *Phys. Rev.* **177**, 2515 (1969).
- [87] J. I. Basdevant and B. W. Lee, *Phys. Rev. D* **2**, 1680 (1970).
- [88] H. B. Geddes and R. H. Graham, *Phys. Rev. D* **12**, 855 (1975).
- [89] H. B. Geddes and R. H. Graham, *Phys. Rev. D* **13**, 56 (1976).
- [90] Z. Aouissat, R. Rapp, G. Chanfray, P. Schuck, and J. Wambach, *Nucl. Phys. A* **581**, 471 (1995), arXiv:nucl-th/9406010.
- [91] J. Soto, P. Talavera, and J. Tarrus, *Nucl. Phys. B* **866**, 270 (2013), arXiv:1110.6156 [hep-ph].
- [92] A. H. Fariborz, N. W. Park, J. Schechter, and M. Naeem Shahid, *Phys. Rev. D* **80**, 113001 (2009), arXiv:0907.0482 [hep-ph].
- [93] E. van Beveren, F. Kleefeld, G. Rupp, and M. D. Scadron, *Mod. Phys. Lett. A* **17**, 1673 (2002), arXiv:hep-ph/0204139.
- [94] D. Black, A. H. Fariborz, R. Jora, N. W. Park, J. Schechter, and M. Naeem Shahid, *Mod. Phys. Lett. A* **24**, 2285 (2009), arXiv:0904.2161 [hep-ph].
- [95] S. Weinberg, *The quantum theory of fields. Vol. 2: Modern applications* (Cambridge University Press, 2013).
- [96] D. F. Litim and J. M. Pawłowski, *Phys. Rev. D* **65**, 081701 (2002), arXiv:hep-th/0111191; *Phys. Rev. D* **66**, 025030 (2002), arXiv:hep-th/0202188.
- [97] N. Strodthoff, B.-J. Schaefer, and L. von Smekal, *Phys. Rev. D* **85**, 074007 (2012), arXiv:1112.5401 [hep-ph]; J. Stoll, N. Zorbach, A. Koenigstein, M. J. Steil, and S. Rechenberger, (2021), arXiv:2108.10616 [hep-ph].
- [98] J. Gasser, *PoS EFT09*, 029 (2009).
- [99] M. Gell-Mann, R. J. Oakes, and B. Renner, *Phys. Rev.* **175**, 2195 (1968).
- [100] B.-J. Schaefer and H.-J. Pirner, *Nucl. Phys. A* **627**, 481 (1997), arXiv:hep-ph/9706258.
- [101] M. Loewe and C. V. Martinez, *Phys. Rev. D* **77**, 105006 (2008), [Erratum: *Phys.Rev.D* **78**, 069902 (2008)], arXiv:0801.2176 [hep-ph]; M. Loewe, L. Monje, and R. Zamora, *Phys. Rev. D* **97**, 056023 (2018), arXiv:1712.10047 [hep-ph]; M. Loewe, L. Monje, E. Muñoz, A. Raya, and R. Zamora, *Phys. Rev. D* **99**, 056002 (2019), arXiv:1901.03256 [hep-ph]; M. Loewe, E. Muñoz, and R. Zamora, *Phys. Rev. D* **100**, 116006 (2019), arXiv:1905.03783 [hep-ph].
- [102] E. Grossi and N. Wink, (2019), arXiv:1903.09503 [hep-th]; E. Grossi, F. J. Ihssen, J. M. Pawłowski, and N. Wink, *Phys. Rev. D* **104**, 016028 (2021), arXiv:2102.01602 [hep-ph]; A. Koenigstein, M. J. Steil, N. Wink, E. Grossi, J. Braun, M. Buballa, and D. H. Rischke, (2021), arXiv:2108.02504 [cond-mat.stat-mech]; A. Koenigstein, M. J. Steil, N. Wink, E. Grossi, and J. Braun, (2021), arXiv:2108.10085 [cond-mat.stat-mech]; M. J. Steil and A. Koenigstein, (2021), arXiv:2108.04037 [cond-mat.stat-mech].
- [103] G. Ecker, J. Gasser, A. Pich, and E. de Rafael, *Nucl. Phys. B* **321**, 311 (1989).
- [104] F. Giacosa, A. Koenigstein, and R. D. Pisarski, *Phys. Rev. D* **97**, 091901 (2018), arXiv:1709.07454 [hep-ph].
- [105] S. L. Adler, *Phys. Rev.* **137**, B1022 (1965); *Phys. Rev.* **139**, B1638 (1965).
- [106] D. F. Litim, *Phys. Rev. D* **64**, 105007 (2001), arXiv:hep-th/0103195.
- [107] M. Q. Huber and J. Braun, *Comput. Phys. Commun.* **183**, 1290 (2012), arXiv:1102.5307 [hep-th]; M. Q. Huber, A. K. Cyrol, and J. M. Pawłowski, *Comput. Phys. Commun.* **248**, 107058 (2020), arXiv:1908.02760 [hep-ph].
- [108] A. K. Cyrol, M. Mitter, and N. Strodthoff, *Comput. Phys. Commun.* **219**, 346 (2017), arXiv:1610.09331 [hep-ph].
- [109] R. Mertig, M. Bohm, and A. Denner, *Comput. Phys. Commun.* **64**, 345 (1991); V. Shtabovenko, R. Mertig, and F. Orellana, *Comput. Phys. Commun.* **207**, 432 (2016), arXiv:1601.01167 [hep-ph]; *Comput. Phys. Commun.* **256**, 107478 (2020), arXiv:2001.04407 [hep-ph].